UCLA
UCLA Electronic Theses and Dissertations

Title

Modeling the Formation of the First Stars and Their Effects on the Cosmological 21-cm Background

Permalink

Author

Mebane, Richard

Publication Date

2020

Peer reviewed|Thesis/dissertation

UNIVERSITY OF CALIFORNIA

Los Angeles

**Modeling the Formation of the First Stars
and Their Effects on the Cosmological 21-cm Background**

A dissertation submitted in partial satisfaction

of the requirements for the degree

Doctor of Philosophy in Astronomy and Astrophysics

by

Richard Harris Mebane

2020

ABSTRACT OF THE DISSERTATION

Modeling the Formation of the First Stars
and Their Effects on the Cosmological 21-cm Background

by

Richard Harris Mebane

Doctor of Philosophy in Astronomy and Astrophysics

University of California, Los Angeles, 2020

Professor Steven R. Furlanetto, Chair

The first generations of stars in the Universe have never been observed, though they played an important role in the early evolution of galaxies. These stars likely began forming in isolation from pristine gas in small dark matter minihalos, and they set the stage for more traditional star formation in galaxies. Though they will be difficult to observe directly, we may detect their presence in the cosmological 21-cm background. For my thesis, I developed a semi-analytic model studying the formation and evolution of Population III star forming halos. I investigated the effects that this mode of star formation has on the 21-cm background by modeling both the average signal and its spatial fluctuations. Finally, I investigated the effects of warm dark matter on early Universe star formation. In general, I found that Pop III stars can have a large effect on the 21-cm background, and studying this signal will teach us much about structure formation and star formation in the early Universe.

The dissertation of Richard Harris Mebane is approved.

Alice E. Shapley

Smadar Naoz

Matthew A. Malkan

Steven R. Furlanetto, Committee Chair

University of California, Los Angeles

2020

LIST OF TABLES

2012–2014   **Undergraduate Researcher**, Department of Physics, Carnegie Mellon University, Pittsburgh, PA

2014   **B.S., Physics**, Carnegie Mellon University, Pittsburgh, PA

2014–2017   **Teaching Assistant**, Department of Physics and Astronomy, UCLA, Los Angeles, CA. Astronomy 4 – Black Holes and Cosmic Catastrophes (Fall 2014), Astronomy 3 - Nature of the Universe (Winter and Fall 2015), Astronomy 274 - Extragalactic Astrophysics I (Grader, Winter 2017)

2015–present   **Graduate Student Researcher**, Department of Physics and Astronomy, UCLA, Los Angeles, CA

2016   **M.S., Astronomy**, UCLA, Los Angeles, CA

PUBLICATIONS

A Minimalist Feedback-Regulated Model for Galaxy Formation During the Epoch of Reionization

Furlanetto, S.R., Mirocha, J., Mebane, R.H., Sun, G., 2017, MNRAS, 472, 2, p.1576-1592

Unique Signatures of Population III Stars in the Global 21-cm Signal

Mirocha, J., Mebane, R.H., Furlanetto, S.R., Singal, K., Trinh, D., 2018, MNRAS, 478, 4, p.5591-5606

The Persistence of Population III Star Formation

Mebane, R.H., Mirocha, J., Furlanetto, S.R., 2018, MNRAS, 479, 4, p.4544-4559

The Effects of Population III Radiation Backgrounds on the Cosmological 21-cm Signal

Mebane, R.H., Mirocha, J., Furlanetto, S.R., 2020, MNRAS, 493, 1, p.1217-1226

CHAPTER 1

Introduction

The formation and evolution of galaxies likely began in the first 100 million years after the Big Bang, and the earliest progenitors of these galaxies were no more than a small cluster of gas and stars in overdense regions of dark matter called halos. These early star forming halos were many orders of magnitude less massive than the galaxies we observe today, though they would grow substantially throughout cosmic time through accretion of new material and mergers with other halos. As the first stars formed and lived out their lives, they would disrupt the structure of the gas in these halos as well as chemically enrich them, setting the stage for the overall evolution of star formation throughout the Universe.

The first stars which formed in the Universe were likely very different than those we observe today. These stars, called Population III stars, formed out of pristine, metal-free gas in small dark matter minihalos. These stars were short lived and formed in small numbers, but they were of vital importance to the evolution of star formation in the Universe. Throughout their lifetime, these Pop III stars fused hydrogen into more complex elements, or metals, which were necessary for the transition to more traditional star formation. Understanding the process through which this first generation of stars formed is an important step in understanding the cosmic dawn of the Universe.

Pop III star formation occured through a different channel than star formation today. Traditionally, stars form when a molecular cloud collapses and fragments due to metal-line cooling, where metal ions become collisionally excited and radiate energy away from the

cloud. Before the first stars formed, however, clouds were cooled with molecular hydrogen. Because H_2 cooling is less efficient than metal-line cooling, molecular clouds likely had less fragmentation, causing Pop III stars to be more massive and luminous (e.g., Bromm et al., 1999; Abel et al., 2002; Bromm, 2013). The actual initial mass function (IMF) of this mode of star formation is unknown, though because of their increased mass, Pop III stars had short lives that ended in either a supernova or a direct collapse to a black hole.

The dark matter halos which formed Pop III stars were very small and highly susceptible to feedback. A typical core-collapse Pop III supernova will release $\sim 10^{51}$ erg of kinetic energy, which is potentially many orders of magnitude higher than the typical gravitational binding energy of these early halos. Because of this, a single supernova could completely unbind all of the gas in a halo, causing Pop III stars to form in very small numbers or perhaps even in isolation (e.g., Machacek et al., 2001; Wise & Abel, 2007; O'Shea & Norman, 2008; Shapiro et al., 2004; Visbal et al., 2018; Mebane et al., 2018).

There are many uncertainties involved in modeling the formation of Pop III stars. Because we have never directly observed a Pop III star forming halo, we do not know their IMF, star formation efficiency, luminosity, or abundance. We also do not know how they produced metals, or how these metals mixed in to their birth halos to begin the transition to metal-enriched Pop II star formation. While there have been many studies of Pop III star formation including analytic models (e.g., McKee & Tan 2008; Kulkarni et al. 2013), semi-analytic models (e.g., Trenti et al. 2009; Crosby et al. 2013a; Jaacks et al. 2018; Visbal et al. 2018; Mebane et al. 2018), and numerical simulations (e.g., Machacek et al. 2001; Wise & Abel 2007; O'Shea & Norman 2008; Xu et al. 2016; Stacy et al. 2012; Hirano et al. 2015; Maio et al. 2010; Sarmento et al. 2018), all of these must probe a very large range in parameter space. In order to better understand this star formation, we must eventually detect the formation of Pop III stars through either direct or indirect methods.

As astronomers build larger telescopes, we are able to probe smaller galaxies at higher

redshifts. This is very important for understanding the luminosity function of the high redshift galaxies that reionize the neutral hydrogen in the intergalactic medium (IGM), although we are still very far away from probing the luminosities and redshifts of Pop III halos. Unfortunately, due to the extremely low star formation efficiency of these minihalos, it is unlikely that we will ever be able to directly observe Pop III star formation (Schauer et al. 2020 find we would need a $\sim$ 100 m telescope in space). Upcoming telescopes such as the James Webb Space Telescope (JWST) will detect the dimmest and highest redshift galaxies ever oberved, so even if we do not directly observe a Pop III halo, we may see the byproducts of its evolution. Despite this, however, we may have to turn to indirect methods to observe Pop III star formation.

For the first project in my thesis, I developed a new semi-analytic model studying the formation and evolution of Pop III star forming halos (Mebane et al., 2020). This model follows individual dark matter halos, tracking their Pop III star formation, metal enrichment, and transition to Pop II star formation. I include self-consistent calculations of both the local and global feedback processes that affect these small minihalos. Since there are so many uncertainities involved in modeling Pop III star formation, I include studies of many different models, varying the Pop III IMF and star formation prescription as well as the formation process of Pop II stars. I then used this semi-analytic model in my other thesis projects to study the cosmic 21-cm background and constrain models of warm dark matter.

The cosmological 21-cm background is produced from neutral hydrogen atoms in the early Universe. This background is the product of the hyperfine "spin-flip" transition of neutral hydrogen which can absorb or emit photons at a wavelength of 21-cm. At the redshifts when the first stars are forming, hydrogen in the IGM is almost completely neutral. We expect to detect this signal in either absorption or emission relative to the dominant radio background at that time, generally thought to be the cosmic microwave background (CMB). The spin temperature of neutral hydrogen, which defines the relative fraction of hydrogen atoms in

each of the hyperfine states, is set by the ultraviolet (UV) and X-ray radiation backgrounds generated by the first stars. As star formation progresses, the 21-cm background will go through three distinct phases (Furlanetto, 2006).

The first of these phases occurs when a strong Lyman-α background is built up throughout the Universe from early star formation. These Lyα photons, produced from the $n = 2$ to $n = 1$ electronic transition of neutral hydrogen, couple to the spin temperature of the IGM and produce an absorption signal. Measuring the timing and depth of this signal will teach us much about the onset of star formation in the early Universe.

The second phase occurs when remnants from early star formation begin to build up an X-ray background. These X-rays have a long mean free path, causing them to uniformly heat the IGM. This pushes the 21-cm signal out of absorption and potentially into emission relative to the CMB. An observation of this heating will not only teach us about the formation of the first stars but also the emission properties of their remants.

The final phase occurs when star formation has built up a sufficiently strong ionizing background to completely reionize the neutral hydrogen in the IGM. At this point, the 21-cm signal vanishes. It is unlikely that Pop III star formation in minihalos will contribute much to this process, as most models predict their formation ends well before the epoch of reionization.

For my second thesis project, I studied the effects that early generations of star formation have on the 21-cm global signal. I performed a calculation of this signal using an altered form of the 21-cm simulation code ARES (Mirocha, 2014) which interfaces with my semi-analytic model and computes the effects of Pop III radiation backgrounds on the main 21-cm absorption feature (Mebane et al., 2020).

Beyond the global evolution of this background, there is also much information in the spatial variations of the 21-cm signal. This may be very important for studying Pop III star forma-

tion, as these stars form in minihalos far smaller and more abundant than more traditional galaxies. If Pop III stars can affect the 21-cm signal on different scales than "normal" star formation, they may have a unique signature in measurements of the 21-cm power spectrum. For my third thesis project, I looked for unique signatures of Pop III star formation in the 21-cm power spectrum using an updated version of the code 21CMFAST (Mesinger et al., 2011).

Observations of the 21-cm background will occur as both global signal experiments which measure the average evolution of the signal as well as power spectrum or imaging experiments which measure its spatial structure. So far, only the Experiment to Detect the Global EoR Signature (EDGES) has claimed a detection of the 21-cm global signal (Bowman et al., 2018), though there are many concerns that this detection may be the result of instrumental artifacts (e.g., Hills et al., 2018; Sims & Pober, 2020; Tauscher et al., 2020) and confirmation from another experiment is required. Future experiments such as the Hydrogen Epoch of Reionization Array (HERA) and the Square Kilometre Array (SKA) will probe the structure of this signal at the highest sensitivies yet, and they should be able to detect the 21-cm background if current models of its evolution are correct.

Much of the work on these subjects assumes that the dark matter which forms the underlying structures for star formation is "cold" with very small thermal velocities. Through measurements of the Lyα forest and gravitational lensing studies, we have been able to probe this assumption on relatively small scales to test if there is a "warm" component of dark matter. Many species of these thermalized warm dark matter particles have been theorized, such as the sterile neutrino (e.g. Kusenko, 2009). Regardless of the specific nature of warm dark matter, however, it will affect the formation of small scale structure in the Universe. In particular, the formation of halos with a virial velocity below the scale of the velocity dispersion of this dark matter will be suppressed. This effect is strongest at the high redshifts and low halo halos masses where the first stars form. Even within current observational limits on

the effects of warm dark matter, the abundance of the halos which form Pop III and early Pop II stars can be greatly affected. By studying this effect on early star formation and the resulting 21-cm background we can probe the formation of structure at mass scales below that of other methods. For my final thesis project, I studied the effects of warm dark matter on Pop III star formation and the 21-cm signal by using an altered version of my Pop III semi-analytic model.

My thesis is outlined as follows: In Chapter 2 I describe my semi-analytic model for Pop III star formation. In Chapter 3 I present my study of the effects of Pop III star formation on the 21-cm global signal. In Chapter 4 I investigate unique signatures of Pop III star formation on the 21-cm power spectrum. In Chapter 5 I study the effects of warm dark matter on early Universe star formation and the 21-cm signal. Finally, I summarize my results in Chapter 6.

CHAPTER 2

The Persistence of Population III Star Formation

2.1   Introduction

The first stars to have formed in the Universe were likely very different from those observed today, and their formation was crucial to the early evolution of galaxies. It is thought that these Population III (Pop III) stars formed in metal-free gas clouds through molecular hydrogen cooling, and they were therefore much more massive (Bromm et al., 1999; Abel et al., 2002) and luminous than today's metal-enriched stars (see Bromm 2013). Because of their high luminosity and the small size of their birth halos, feedback may have played an important role in the formation of Pop III stars (Machacek et al., 2001; Wise & Abel, 2007; O'Shea & Norman, 2008; Shapiro et al., 2004), and they most likely formed in very small numbers, perhaps in isolation (Visbal et al., 2018). Despite their small numbers, they must have been able to produce enough metals to eventually allow their halos to begin forming the more traditional Population II (Pop II) stars in a reasonably short amount of time.

There have been many attempts to study the formation and properties of these Pop III stars through the use of detailed numerical simulations (e.g., Machacek et al. 2001; Wise & Abel 2007; O'Shea & Norman 2008; Xu et al. 2016; Stacy et al. 2012; Hirano et al. 2015; Maio et al. 2010; Sarmento et al. 2018), analytic arguments (e.g., McKee & Tan 2008; Kulkarni et al. 2013), and semi-analytic models (e.g., Trenti et al. 2009; Crosby et al. 2013a; Jaacks et al. 2018; Visbal et al. 2018). Simulations of their supernovae (Heger & Woosley 2002 and

Heger & Woosley 2010) have found that such stars are able to produce a very high mass of metals that will eventually be used to cool gas more efficiently and form stars from a more traditional initial mass function (IMF). In some simulations, Pop III stars are found to form often in binaries (Turk et al. 2009), which could potentially produce a cosmologically relevant abundance of Pop III high-mass X-ray binaries.

While there has been much work done to study the properties of Pop III stars, we have yet to directly observe a Pop III halo. There has been one candidate at $z \sim 7$ described in Sobral et al. (2015), although there are still many other possible explanations (e.g., Bowler et al. 2017 and Agarwal et al. 2016), and recent ALMA observations have detected [CII] consistent with a normal star-forming galaxy (Matthee et al., 2017). Unfortunately, since it is thought that Pop III stars form in very low mass halos at high redshift, it may prove incredibly difficult to directly observe a Pop III source. If the mixing of metals in Pop III halos is very inefficient, as in Sarmento et al. (2018), Pop III stars may be able to coexist with metal-enriched Pop II stars to late times, allowing for a better chance of observation. Even if these halos are too faint to observe with the James Webb Space Telescope (JWST), however, we may be able to detect their supernovae with an instrument such as the Wide-Field Infrared Survey Telescope (WFIRST) (Whalen et al. 2013), or we could potentially see their effect on the cosmological 21-cm background (Mirocha et al. 2018). All of these measurements are very sensitive to the overall shape of the Pop III star formation rate density and the timing of the transition to Pop II star formation.

In order to understand how Pop III halos make the transition to Pop II star formation, we must focus on both internal and external processes. In a particular halo, star formation produces important feedback effects such as supernovae and photoionization (see Bromm et al., 2003; Whalen et al., 2008a,b). These effects can either limit or completely cut off Pop III star formation based on the size of the halo and its growth due to mass accretion.

But the Pop III phase is also sensitive to large-scale radiation fields generated by those

stars and their successors. The evolution of Pop III star formation in the presence of global feedback driven by Pop II star formation is not well understood and is a key interest to this work. In particular, UV photons in the Lyman-Werner band emitted by Pop II stars can destroy the molecular hydrogen in Pop III clouds necessary for cooling (Haiman et al. 1997). This sets the minimum halo mass at which molecular hydrogen can self shield in a halo and cool to form stars (Visbal et al. 2014). This minimum mass is a crucial physical quantity, as the halo mass function is very steep. The properties of even the Pop II halos at these redshifts are unknown, however, so studying their effects on the formation of Pop III stars in a flexible model is of much use.

In this work, we employ an efficient and flexible semi-analytic model that allows us to model the formation of Pop III stars over a wide range of parameters and assumptions. While our model is certainly simpler than numerical simulations with similar goals, we are able to compare many different models while still self-consistently computing the effects of a wide range of feedback processes including a meta-galactic Lyman-Werner background, supernovae, photoionization, and chemical feedback. As described below, we use many results from observations, simulations, and analytic arguments to simplify our model and justify our assumptions.

Pop III star formation is a complex process that can proceed through different channels. In this work, we will focus on the "classical" process through which primordial gas remains neutral while it accretes onto a dark matter halo and then cools purely through H_2 line emission (Bromm et al., 1999; Abel et al., 2002). The resulting star-forming regions are relatively hot and thus have Jeans masses of $\gtrsim 100\,M_\odot$, which likely leads to massive stars (though their actual masses are the subject of intense debate; e.g., Bromm et al. 1999; Abel et al. 2002; Clark et al. 2011; Hirano & Bromm 2017). In this paper, we distinguish this "minihalo" mode from star formation in halos with virial temperatures $\gtrsim 10^4$ K: in that case, the chemistry differs from the classic case (e.g., HD cooling becomes significant; Oh

& Haiman 2002; Johnson & Bromm 2006; Yoshida et al. 2007b; McGreer & Bryan 2008),
and the resulting stars, even if they remain metal-free, form in very different environments.
Moreover, as we show below, in this regime halos become more stable to supernova feedback
and are likely to develop quasi-equilibrium interstellar media, inside which metal mixing
will become significant. Our model will therefore focus primarily on Pop III star formation
inside "minihalos" below the atomic cooling threshold. We will study how long this mode
can persist through the early generations of galaxies. Several other studies consider the
possibility of Pop III star formation in more massive halos, including the mixing of metals
throughout the interstellar medium (e.g., Sarmento et al. 2018).

In Section 2.2 we describe the properties of dark matter halos in our model, including the
halo mass function and the growth of halos. In Section 2.3 we discuss our treatment of
the first minihalos which will form metal-free Pop III stars. In Section 2.4 we describe the
properties of the Pop II halos which form the very first generations of metal-enriched stars.
We present our results in Section 2.5, caveats to our model in Section 2.6, a discussion of
their implications for observations of star formation in the early universe in Section 2.7, and
conclude in Section 2.8.

In this work, we use a flat, ΛCDM cosmology with $\Omega_{\mathrm{m}} = 0.28$, $\Omega_{\mathrm{b}} = 0.046$, $\Omega_{\Lambda} = 0.72$,
$\sigma_8 = 0.82$, $n_{\mathrm{s}} = 0.95$, and $h = 0.7$, consistent with the results from Planck Collaboration
et al. (2015). Any distances presented are shown in comoving units.

2.2 Halo Properties

Our model will follow the growth of a set of dark matter halos from very early times to
$z = 6$. To begin, we choose a set of halos with $z = 6$ masses from $10^6 M_\odot$ to $10^{13} M_\odot$ in
10,000 logarithmically spaced bins. These halos are then tracked backwards to $z = 50$ using
the abundance matching technique described in section 2.2.2 in 1 Myr timesteps. With these

mass histories in hand, we then track each halo individually, applying the semi-analytic model discussed in future sections to determine the feedback-limited star formation histories of both Pop III and Pop II stars. Global quantities (to be discussed in the following section) such as the star formation rate density and Lyman-Werner background are found by averaging all halos over the mass function.

2.2.1 The Halo Mass Function

The first component of our model is the number density of dark matter halos. We assume that all halos which can accrete gas will form stars, so knowing their abundance is of vital importance.

The halo mass function can be written as

$$n(M) = \frac{\bar{\rho}}{M} f(\sigma) \left| \frac{\mathrm{d} \log \sigma}{\mathrm{d}M} \right|, \tag{2.1}$$

where σ is the density variance, $\bar{\rho}$ is the matter density, and $f(\sigma)$ depends on the particular form of the mass function. In general, $f(\sigma)$ can be found through fits to simulations or through analytic arguments. We test the dependence of our model on the chosen mass function by examining a Sheth-Tormen mass function (Sheth & Tormen, 1999) and the mass function of Trac et al. (2015), which is a fit to high redshift simulations. These two choices do not lead to any significant differences in our results, especially given the wide uncertainty in the other model parameters (see Fig. 2.1). We employ the Trac et al. (2015) mass functions throughout the rest of this paper.

2.2.2 The Growth of Dark Matter Halos

There have been many attempts to model the overall mass accretion rates of dark matter halos following simulations or analytic arguments (e.g., McBride et al., 2009; Behroozi et al.,

2013; Dekel & Krumholz, 2013; Goerdt et al., 2015). For example, Dekel & Krumholz (2013) write the overall mass accretion rate as

$$\dot{M} = AM^{\mu} (1+z)^{\beta}, \tag{2.2}$$

where M is the halo mass, A is a normalization, $\mu \gtrsim 1$ from simulations (see McBride et al. 2009 and Trac et al. 2015), and $\beta = 2.5$, which is consistent with analytic arguments (e.g., Neistein & Dekel, 2008). By fitting to numerical simulations, Trac et al. (2015) found that $\mu = 1.06$ for $M \sim 10^8$–$10^{13} M_{\odot}$ at $z \sim 6$–10, which overlaps with the mass and redshift range we need but does not probe the full range we require.

While these accretion rates have been tested in simulations at moderate mass ranges and redshifts ($z \sim 6$), it is unclear whether they are valid for the smallest halos which begin forming stars at very high redshift. Since the focus of our model is on Pop III star formation, we use another model for the growth of halos.

We make the simple assumption that halos maintain their comoving number densities throughout time. This allows us to determine the mass histories of halos directly from the halo mass function by matching their abundances given by the mass function over a range of redshifts (see Furlanetto et al. 2017 for a more detailed description of this technique). The mass histories for a number of halos in our model found through abundance matching are shown in Fig. 2.1. Results with our two mass functions only differ by a factor of ~ 2 at the highest redshifts, so our analysis does not depend strongly on its exact form. The dotted curves use the Trac et al. (2015) simulation fit to eq. 2.2, which has a much larger discrepancy. However, it is only off by a factor of order unity for low mass halos and does not have a large effect on persistence of Pop III star formation in minihalos(see section 2.6.1).

We note that our model for the growth of dark matter halos only follows the average growth, and thus we ignore the effect of mergers. Behroozi & Silk (2015) found that the majority of accretion onto dark matter halos at high redshift occurs as smooth accretion from the IGM,

though we will revisit the effects of mergers in section 2.6.2.

2.3 Properties of Pop III Halos

The first star-forming minihalos were very small and likely contained only a handful of very massive, metal-free stars. These stars formed in molecular clouds that were cooled by molecular hydrogen, rather than the metal-line cooling which occurs in star-forming regions today. Correctly modeling the growth of these halos and the time at which the first stars form is of vital importance to this work so that we can self-consistently model the feedback-limited star formation in the early universe and the transition to more typical, Pop II star formation. In this section, we will describe the properties of these halos and the processes by which minihalo Pop III star formation began.

2.3.1 The Minimimum Mass

In our model, we allow a new halo to begin forming stars only when it passes a minimum mass determined by the time-weighted Jeans mass (filtering mass) and the physics of H_2 cooling. Tegmark et al. (1997) found that a halo must exceed a certain fraction of molecular hydrogen in order for cooling to become efficient, which is given by

$$f_{\text{crit, H}_2} \approx 1.6 \times 10^{-4} \left(\frac{1+z}{20} \right)^{-3/2} \left(1 + \frac{10 T_3^{7/2}}{60 + T_3^4} \right)^{-1} \exp \left(\frac{512\text{K}}{T} \right), \qquad (2.3)$$

where T is the virial temperature of the halo and $T_3 = T/10^3\text{K}$. In these halos, molecular hydrogren is formed primarily through the process

$$\text{H} + \text{e}^- \rightarrow \text{H}^- + h\nu \qquad (2.4)$$

$$\text{H}^- + \text{H} \rightarrow \text{H}_2 + \text{e}^-, \qquad (2.5)$$
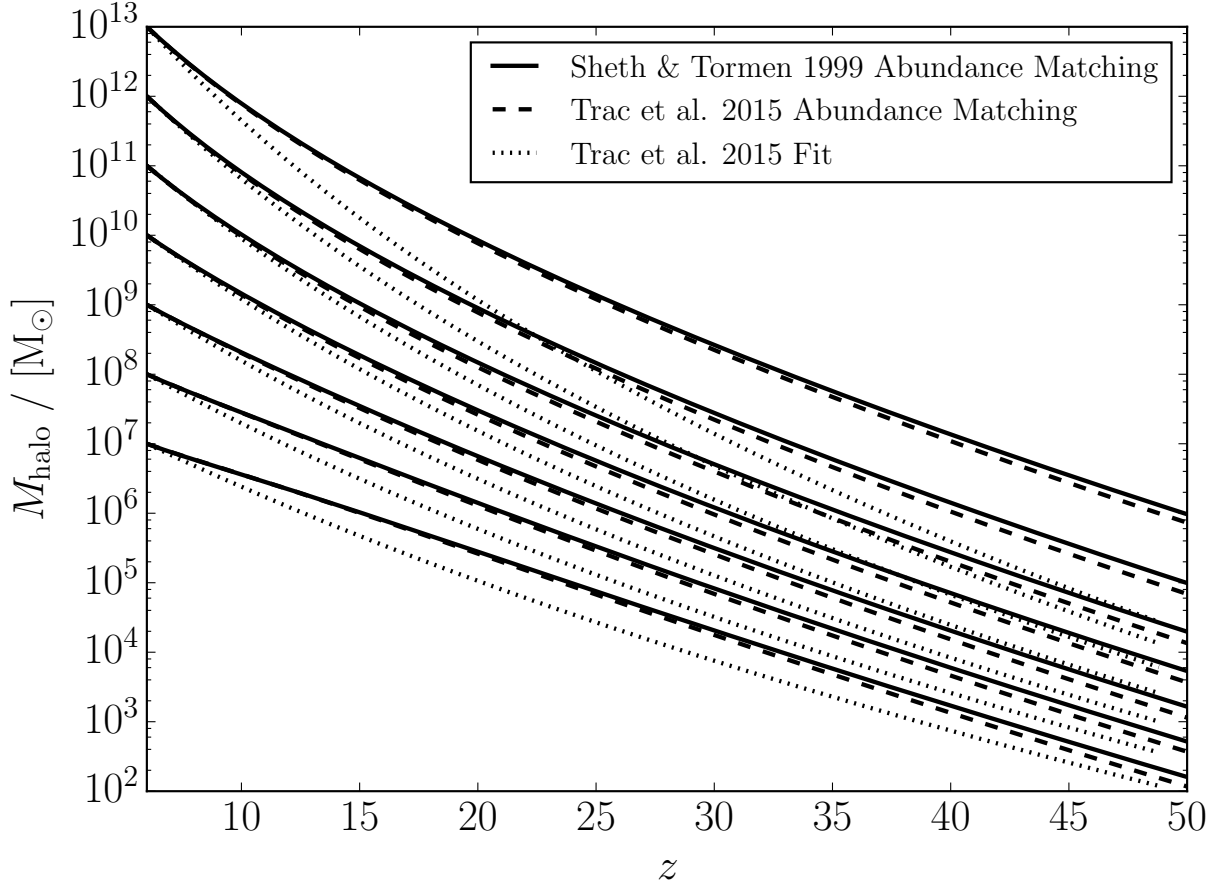
Figure 2.1: Mass histories of halos in our model. Halo growth is determined by abundance matching, where we assume halos remain at a constant comoving number density throughout time and find their mass by comparing mass functions at each time step (see section 2.2.2). The solid and dashed lines use mass functions from Sheth & Tormen (1999) and Trac et al. (2015), respectively. The dotted line is made using the Trac et al. (2015) fit to eq. 2.2. Halos are initialized at the same mass at $z = 6$, and their masses are then tracked backwards to $z = 50$.

where free electrons catalyze the reaction. At high redshifts, H^- can be easily destroyed by cosmic microwave background (CMB) photons, so we must balance the formation rate with the destruction rate to get the overall H_2 fraction in a halo. Tegmark et al. (1997) found this fraction to scale with a halo's virial temperature as

$$f_{H_2} \approx 3.5 \times 10^{-4} \, T_3^{1.52}. \tag{2.6}$$

Once $f_{H_2} > f_{crit,\,H_2}$, molecular hydrogen cooling will become efficient enough to cool gas into the first star-forming molecular clouds. In our model, we assume star formation begins immediately after this criterion is met, with no delay. This occurs in very small halos with masses $\sim 10^5 \, M_\odot$ at the highest redshifts in our model ($z \sim 50$).

After the first stars form, however, the minimum mass will instead be set by the metagalactic Lyman-Werner background. The Lyman-Werner (LW) band consists of photons in the energy range 11.5-13.6 eV that photodissociate molecular hydrogen through the Solomon process (see Stecher & Williams, 1967). If a halo is present in a high enough background of Lyman-Werner photons, it can lose all of its molecular hydrogen and no longer be able to cool gas in star-forming regions. Therefore, a self-consistent calculation of this background is required to determine the minimum masses of Pop III halos (see Haiman et al., 1997; Holzbauer & Furlanetto, 2012; Visbal et al., 2014).

Following Visbal et al. (2014) the background can be written as

$$J_{LW}(z) = \frac{c}{4\pi} \int_z^{z_m} \frac{dt}{dz'} \, (1+z)^3 \, \epsilon(z') dz', \tag{2.7}$$

where $\epsilon(z)$ is the specific Lyman-Werner comoving luminosity density and z_m is the maximum redshift at which Lyman-Werner photons can be emitted before they redshift into a Lyman line. For simplicity, we assume that all photons can be redshifted by a maximum of 4% (Visbal et al., 2014) before being absorbed by a Lyman resonance of neutral hydrogen in the IGM. This can be found from a simple fit to calculations of the redshifting of these lines.

We calculate $\epsilon(z)$ as

$$\epsilon(z) = \int_{M_{\mathrm{min}}}^{\infty} n(M) \frac{\Omega_{\mathrm{b}}}{\Omega_{\mathrm{m}}} \frac{\dot{M}_*}{m_{\mathrm{p}}} \left(\frac{N_{\mathrm{LW}} E_{\mathrm{LW}}}{\Delta\nu_{\mathrm{LW}}} \right) \mathrm{d}M, \qquad (2.8)$$

where M_{min} is the minimum mass at which a halo can form stars, $\dot{M}_*$ is the star formation rate in a halo of mass M, N_{LW} is the number of LW photons produced per baryon in stars, E_{LW} is the average energy of a LW photon, and $\Delta\nu_{\mathrm{LW}}$ is the frequency range of the LW band. We take $N_{\mathrm{LW}} = 1 \times 10^5$, which is roughly constant for massive Pop III stars (Schaerer, 2002), $N_{\mathrm{LW}} = 9690$ for Pop II stars (Barkana & Loeb, 2005), $E_{\mathrm{LW}} = 11.9$ eV, and $\Delta\nu_{\mathrm{LW}} = 5.8 \times 10^{14}$ Hz. We compute $\dot{M}_*$ individually for each halo in both the Pop II and Pop III phases.

In order to determine which halos can form stars under a given LW background, we look to hydrodynamical simulations (e.g., Machacek et al., 2001; Wise & Abel, 2007; O'Shea & Norman, 2008). Visbal et al. (2014) find that the critical mass above which halos can form stars under a given LW background can be approximated by

$$M_{\mathrm{min}} = 2.5 \times 10^5 \left(\frac{1+z}{26} \right)^{-1.5} \left(1 + 6.96 \left(4\pi J_{\mathrm{LW}} \right)^{0.47} \right). \qquad (2.9)$$

Once we calculate J_{LW} from our model, we can determine which minihalos will form Pop III stars by only considering masses where $M > M_{\mathrm{min}}$.

For a halo to obtain enough gas to begin star formation, its gas mass must exceed the time-weighted Jeans mass, known as the filtering mass (see Gnedin & Hui, 1998). We enforce this in our model, only allowing stars to form in halos where the gas mass exceeds the fit to the filtering mass found in Naoz & Barkana (2007). In practice, this mass is always below the minimum mass from the Lyman-Werner background after the first stars form, and it only exceeds the Tegmark et al. (1997) mass at redshifts much higher than we are interested. Therefore, the filtering mass does not have a noticeable impact on our results.

In this work, we neglect the potential feedback effects of X-rays, which can catalyze H_2 formation by enhancing the free electron fraction and thus act as a source of positive feedback,

or, could alternatively heat gas and prevent further fragmentation and star formation (e.g., Machacek et al., 2003; Kuhlen & Madau, 2005). The importance and sense of the feedback (i.e., positive or negative) will depend on the interplay between the Lyman-Werner and X-ray backgrounds, which in turn depends on the detailed properties of sources and their number density as a function of redshift (e.g., Ricotti, 2016). For now, we neglect these effects and defer a more detailed consideration to future work.

We also neglect potential H^- photodetachment triggered by an infrared background (as discussed in Wolcott-Green et al., 2017) which can halt the formation of H_2. To test this assumption, we calculate the photodetachment rate, k_{H^-}, using the conversion rate presented by Agarwal et al. (2016) and our model Lyman-Werner backgrounds. We find that, even in the case where this effect should be most important (i.e., only Pop II star formation at lower redshifts with a high star formation rate density), k_{H^-} is well below the threshold for H^- photodetachment to dominate over the Lyman-Werner background (Wolcott-Green et al., 2017) . We note, however, that the calculation in Wolcott-Green et al. (2017) is for halos at the atomic cooling threshold, while our Pop III halos are generally at lower mass. We defer a detailed calculation of this effect for lower mass halos to the future.

2.3.2   The Pop III Initial Mass Function

Once a halo has exceeded the minimum mass required for Pop III star formation, we begin to add the first stars. Since the gas clouds forming these stars cool primarily through molecular hydrogen, which is less efficient than metals, these kinds of Pop III stars were likely very massive (Bromm et al., 1999). The Pop III IMF is very uncertain, however, so we leave this as a parameter in our model (see Table 2.1). Stars are randomly sampled from the chosen IMF and placed in isolation in each star forming region.

The simplest IMF we consider is a delta function, where all Pop III stars form at a single

mass. The prefered mass is not known a priori, but one well-motivated choice is to follow McKee & Tan (2008), who find the maximum mass of a massive Pop III star by calculating the mass at which radiation pressure will stop accretion. McKee & Tan (2008) find this maximum mass to be

$$M_{\mathrm{max}} \approx 145 M_\odot \left(\frac{25}{T_3}\right)^{0.24}. \tag{2.10}$$

If Pop III stars form in isolation in minihalos, then it is possible that all stars eventually reach this mass. In this case, we simply set the mass of every Pop III star to this maximum mass. This case is especially interesting as it is just above the minimum mass at which pair-instability supernovae occur, so small details in the stellar masses are actually quite important.

We also allow for both lower mass and higher mass cases compared to the McKee & Tan (2008) model. In these cases we use a Salpeter-like IMF in various mass ranges. For the low-mass case, we use a minimum mass of 20 $M_\odot$ and a maximum mass of the McKee & Tan (2008) mass (see Bromm et al. 1999 for a discussion of the fragmentation of protostellar disks and its effect on stellar masses). As an extreme high-mass case, we use a minimum mass of 200 $M_\odot$ and a maximum mass of 500 $M_\odot$. As we will discuss in section 2.3.4, the choice of IMF has great implications for supernova feedback and its effects on these growing halos.

We note that our Pop III model assumes a single star or binary system per site of star formation, with a mass drawn from the IMFs described above. This differs from other treatments (e.g., Jaacks et al., 2018; Visbal et al., 2018), which often utilize a fixed mass of star formation or a mass-dependent star formation efficiency. We compare to these similar works in section 2.5.5, as well as test the dependence of our results on this assumption.

It is thought that these massive stars may often form in binaries (Turk et al., 2009), so we also investigate the case of a non-zero binary fraction. Mirocha et al. (2018) find that high-mass x-ray binary systems can produce a unique signature in the global 21-cm signal

although, in this work, a nonzero binary fraction only serves to increase the overall star formation efficiency.

2.3.3   Photoionization Feedback from Pop III Stars

In order to determine how many Pop III star forming regions should form in a single halo, we appeal to photoionization feedback. Since Pop III stars were likely very massive and luminous, they would be able to ionize much of their surrounding material, making it unable to cool and form stars. Assuming a massive Pop III star emits like a blackbody with effective temperature T_{eff} (see Stacy et al., 2012), the number of ionizing photons produced is given by

$$\dot{N} = \frac{\pi L}{\sigma T_{\text{eff}}^4} \int_{\nu_{\text{min}}}^{\infty} \frac{B_\nu}{h\nu} d\nu, \tag{2.11}$$

where L is the star's luminosity, σ is the Stefan-Boltzmann constant, ν_{min} is the minimum photon frequency required for ionization, and B_ν is the blackbody spectrum of the star. We approximate the luminosity of the star over its lifetime as the zero-age main sequence (ZAMS) luminosity, and we calculate T_{eff} assuming the star emits like a blackbody. We use the ZAMS stellar radius and luminosity given by Stacy et al. (2012) as

$$L_{\text{ZAMS}}(M) = 1.4 \times 10^4 L_\odot \left(\frac{M}{10M_\odot}\right)^2, \tag{2.12}$$

$$R_{\text{ZAMS}} = 3.9 R_\odot \left(\frac{M}{10M_\odot}\right)^{0.55}. \tag{2.13}$$

Once a minihalo Pop III star is formed, it will begin to ionize the surrounding gas in its birth cloud. If this radiation is able to ionize all of the gas available for star formation, then no more stars will form. The size of the ionized region around a star is given by the Strömgren radius,

$$R_S = \left(\frac{3\dot{N}}{4\pi n_{\text{H}}^2 \alpha_B}\right), \tag{2.14}$$

Table 2.1: Pop III initial mass functions used in this work. Note that the metal yields are given as the mass of metals produced per unit mass of star formation.

IMF	M_{min}	M_{max}	Slope	E_{SN}/M_* [ergs / $M_\odot$]	C Yield	O Yield
Low Mass	20 $M_\odot$	$\sim 145 M_\odot$ (eq. 2.10)	-2.35	1.58×10^{49}	5.63×10^{-3}	6.25×10^{-2}
Mid Mass	$\sim 145 M_\odot$ (eq. 2.10)	$\sim 145 M_\odot$ (eq. 2.10)	N/A	6.90×10^{49}	3.13×10^{-2}	3.16×10^{-1}
High Mass	200 $M_\odot$	500 $M_\odot$	-2.35	1.41×10^{49}	1.41×10^{-3}	4.49×10^{-2}

where $\dot{N}$ is given by equation (2.11) and n_{H} is the hydrogen number density. Bromm & Larson (2004) find that H_2 cooling tends to drive gas in these halos to densities of around $n_{\mathrm{H}} \sim 10^4$ cm^{-3} at $T \sim 200$ K.

We then assume that the maximum number of stars allowed in a halo can be found by simply packing the halo with Strömgren spheres. Under these assumptions, we find that a single star is able to ionize most of the gas in a minihalo at the masses and redshifts relevant to Pop III star formation. Halos above the atomic cooling threshold would be able to accommodate multiple star formation locations, but they are outside the scope of our model, as we have already assumed that they have transitioned to stable star formation. We note that a single star is still able to ionize the majority of its surrounding gas even if we utilize a more complex model for the distribution of gas in a halo, such as the disc model described in Muñoz & Furlanetto (2013).

We note that Whalen et al. (2008a) also find similar results for the destruction of H_2 in halos forming massive Pop III stars. In their simulations, a 120 M$_\odot$ star is able to completely photodissociate all H_2 in a halo during its lifetime. As these stars form primarily through H_2 cooling, it is unlikely the gas in such a minihalo could cool and form stars near another Pop III star.

It is also possible that internal Lyman-Werner feedback from a Pop III star could dissociate H_2 and stop star formation in a single halo (see Glover & Brand 2001). We neglect this process because ionizing feedback from the same star is already able to ionize the majority of the gas.

2.3.4 Pop III Supernovae

When a massive Pop III star reaches the end of its life, taken to be 5 Myr in this model as stellar lifetimes do not vary appreciably at high mass (Schaerer, 2002), the star will either

explode in a supernova or collapse directly into a black hole. Stars with a mass between 40 $M_\odot$ and 140 $M_\odot$ and those with masses above 260 $M_\odot$ will not end their lives in a supernova, but they will rather collapse directly into a black hole. Stars below this range will explode in a typical core-collapse supernova, while stars in the intermediate range will end with a pair-instability supernova. We therefore only take into consideration supernovae from stars which fall into these two categories. We assume that core-collapse supernovae release a kinetic energy of 10^{51} ergs, while pair-instability supernovae release 10^{52} ergs (see Wise & Abel 2008 and Greif et al. 2010).

Supernova feedback is particularly important in the early universe, as the typical kinetic energy released in a supernova could be orders of magnitude larger than the binding energy of the gas in a halo, which is of order (Loeb & Furlanetto, 2013):

$$E_b \approx 2.53 \times 10^{50} \left(\frac{\Omega_m}{\Omega_m(z)}\right)^{1/3} \left(\frac{M}{10^6 M_\odot}\right)^{5/3} \left(\frac{1+z}{10}\right) h^{2/3} \text{erg}. \tag{2.15}$$

Every time a supernova explodes in a halo, we assume that the kinetic energy released is distributed throughout the remaining gas and calculate the corresponding temperature, assuming ionized, primordial gas. We then assume that the velocities of particles in this gas follow a Maxwell-Boltzmann distribution. This allows us to calculate the fraction of gas remaining in the halo and the fraction exceeding the halo's escape velocity. We then eject this gas, adding it to a reservoir that we later allow to re-accrete onto the halo over a time-scale equal to the halo's free fall time at the moment the gas is ejected,

$$t_{\text{ff}} = \frac{1}{4}\sqrt{\frac{3\pi}{2G\bar{\rho}_{\text{vir}}}}, \tag{2.16}$$

where $\bar{\rho}_{\text{vir}}$ is the average density of the halo (see Yoshida et al. 2007a for a simulation of the re-incorporation of gas into a halo at these redshifts). Note that this can be a significant fraction of a Hubble time as the highest redshifts considered here. If the velocity of the expelled gas is greater than $\sqrt{10}v_{\text{esc}}$, we assume that the gas has completely escaped and will never re-accrete. We discuss the importance of this assumption on our model in section 2.6.4.

This model for gas ejection has strong implications for a halo's transition to Pop II star formation. We assume that the metals released by a supernova follow the gas, so the fraction of metals expelled is the same as the fraction of total gas expelled. This is discussed further in section 2.6.3, where we investigate the fraction of metals which must be retained after a supernova in order for a halo to transition quickly.

2.3.5 Transitioning out of Pop III Star Formation in Minihalos

One very important aspect of our model is the transition between metal-free, minihalo Pop III star formation and metal-enriched Pop II star formation. The minihalo Pop III stars we have discussed are likely born in only one star-forming region per halo (see section 2.3.3), whereas Pop II stars form from a more traditional, low-mass IMF (i.e., a Salpeter IMF). In order to determine at what point halos switch to Pop II star formation, we must look at how gas is cooled to form each type of star.

Once a halo reaches a virial temperature of $T_{\mathrm{vir}} = 10^4$ K, atomic line emission begins to dominate the cooling. This is, coincidentally, also the point where the gas in a halo tends to reach a binding energy of $\sim 10^{51}$ erg (the typical kinetic energy released in a core-collapse supernova) and becomes more stable to supernovae. At this point, we assume that enough gas will be left behind after a supernova for the halo to develop an ISM regulated by internal feedback. We then transition to the model described in Furlanetto et al. (2017). If a halo reaches this point but has yet to retain any metals, we track the first generation of stars formed after this point as a separate population of metal-free stars. As seen in Fig. 2.7, this mode of star formation tends to occur at significantly lower rates than both our fiducial Pop III treatment and metal-enriched Pop II star formation. Note we assume that, after this initial burst of metal-free star formation, metals immediately mix through the halo gas, so that subsequent star formation is Pop II. The transition will be much slower if mixing is inefficient, but we refer the reader to models focusing on that process (e.g., Sarmento et al.

2018).

Before a halo reaches the atomic cooling threshold, it can only transition to Pop II star formation if it has retained enough of the metals released in supernovae. Bromm & Loeb (2003) find that the most important metal transitions to consider when looking at this critical point are CII and OI. In particular, they find the metallicities at which metal line cooling will become more efficient than molecular hydrogen cooling to be $[\mathrm{C/H}]_{\mathrm{crit}} \approx -3.5$ and $[\mathrm{O/H}]_{\mathrm{crit}} \approx -3.05$, where $[\mathrm{A/H}] = \log\left(N_A/N_H\right) - \log\left(N_{A,\odot}/N_{H,\odot}\right)$. Once a halo's mean metallicity surpasses one of these criteria, we then make the switch to the Pop II star-forming regime. Dust cooling may also be efficient down to metallicities as low as $[\mathrm{O/H}] \sim$ -5, so we include a model using this phase of cooling for comparison (see Schneider et al. 2006 and Omukai et al. 2010).

We take our metal yields of Pop III stars from Heger & Woosley (2010) and Heger & Woosley (2002), which provide yields for core-collapse and pair-instability supernovae, respectively. Even though a single supernova may produce enough metals for the halo to reach the critical metallicity, this may not necessarily cause the halo to immediately begin forming Pop II stars since not all metals will be retained. As discussed in section 2.3.4, if metals are ejected from the halo, we must either wait until they re-accrete, until a later period of star formation where the halo is more stable to supernovae feedback, or until enough metals are retained in the presence of supernova feedback.[1] If the binding energy of the halo is small enough that the material is never re-accreted or the halo grows enough during the re-accretion time that the metal mass is insignificant, a minihalo may "forget" about its earliest periods of Pop III star formation and require another burst of star formation before it can make the transition to metal-enriched stars.

Our model assumes that the mean metallicity of the halo is the deciding factor in the

---

[1]Note that we do not assume that the metals have thermalized; rather, we assume that they are entrained in the outflow from the halo.

transition to Pop II star formation, although this may not necessarily be the case. If metals can be more concentrated in certain regions of the halo, it is possible that Pop II stars could begin to form even if the halo does not meet our critical metallicity requirements. We discuss the effects of this assumption in section 2.6.3 and leave a more detailed model of inhomogeneous mixing to a future work.

We also do not include the effects of external enrichment from nearby halos which could allow these massive halos to transition more quickly and also allow low mass halos to skip the Pop III phase altogether (see Smith et al. 2015). Jaacks et al. (2018) find that the total metals produced in their model is not enough to raise the volume averaged metallicity in their simulations above the critical metallicity, indicating that, while a single halo may be able to produce enough metals to cut off star formation locally, it does not affect global Pop III values.

2.4 The Properties of Atomic Cooling Halos

Above $T_{\mathrm{vir}} \sim 10^4$ K, halos are far more stable to supernova feedback, and their cooling channel changes significantly (especially if they are able to retain metals). We therefore assume that star formation proceeds smoothly beyond this point, and we shift our stellar parameters to those appropriate to Pop II stars. In our model, we use a Salpeter IMF and break the assumption that stars form in isolation. We also stop tracking individual stars and simply prescribe the star formation efficiency in each halo. We assume a feedback-regulated star formation efficiency, as in Furlanetto et al. (2017) and Sun & Furlanetto (2016), where star formation is regulated by supernovae through either energy or momentum conservation.

We note that our treatment of star formation above the atomic cooling threshold is much simpler than that of Pop III stars in minihalos. We are mostly concerned with the minihalo stage of halo growth, so our model for more massive halos is only used to calculate the

radiation backgrounds that may contribute to limiting Pop III star formation in minihalos. For simplicity, we will mostly assume that star formation in these massive halos is Pop II, and we will refer to this stage as "Pop II."

In our fiducial model, we find the star formation efficiency in a halo by balancing the kinetic energy released by supernovae with the binding energy of the halo. We follow Furlanetto et al. (2017), who parameterize the star formation efficiency (defined here as the fraction of accreting material which turns into stars) as

$$f_* \approx \frac{1}{1 + \eta\left(M_h, z\right)}, \tag{2.17}$$

where η relates the rate at which gas is ejected due to feedback to the star formation rate, $\dot{M}_{\mathrm{ej}} = \eta \dot{M}_*$.

For energy-regulated star formation, we balance the rate at which supernova energy is released with the rate at which the binding energy of a halo is growing through newly accreted material,

$$\frac{1}{2} \dot{M}_{\mathrm{ej}} v_{\mathrm{esc}}^2 = \dot{M}_* \epsilon_{\mathrm{k}} \omega_{\mathrm{SN}}. \tag{2.18}$$

Here, v_{esc} is the escape velocity from the halo, $\dot{M}_*$ is the star formation rate, ϵ_{k} is the fraction of a supernova's kinetic energy used to drive a wind and lift gas out of the halo, and ω_{SN} is the kinetic energy released in supernovae per unit mass of stars. With this in mind, Furlanetto et al. (2017) find η to be

$$\eta_{\mathrm{E}} = 10 \epsilon_{\mathrm{k}} \omega_{49} \left(\frac{10^{11.5} M_\odot}{M_h}\right)^{2/3} \left(\frac{9}{1+z}\right). \tag{2.19}$$

Here, $\omega_{\mathrm{SN}} = 10^{49} \omega_{49}$ erg $M_\odot^{-1}$ and $\epsilon_{\mathrm{k}} = 0.1$ in our fiducial model.

We also consider the case where momentum is conserved, and we balance the star formation efficiency by comparing the momentum released in supernovae to the momentum required to eject gas from the halo. In this case, Furlanetto et al. (2017) find η to be of the form

$$\eta_{\mathrm{p}} = \epsilon_{\mathrm{p}} \pi_{\mathrm{fid}} \left(\frac{10^{11.5} M_\odot}{M_h}\right)^{1/3} \left(\frac{9}{1+z}\right)^{1/2}, \tag{2.20}$$

where $\epsilon_{\rm p}$ is the fraction of the momentum released in a supernova which drives the winds (taken here to be $\epsilon_{\rm p} = 0.2$ in our fiducial model) and $\pi_{\rm fid}$ defines the momentum injection rate from stars formed from a given IMF, defined as

$$\dot{P} = \pi_{\rm fid} \dot{P}_0 \left(\frac{\dot{m}_*}{M_\odot/\text{yr}} \right). \tag{2.21}$$

Here, $\dot{P}_0 = 2 \times 10^{33}$ g cm/s^2 and $\pi_{\rm fid}$ is of order unity for a Salpeter IMF (see Furlanetto et al. 2017 for a more detailed discussion of this model).

In both of these cases, we impose a maximum value on the fraction of accreted mass that will form stars, f_*. In our fiducial models, we assume $f_{*\rm max} = 0.1$ in the energy-regulated case and $f_{*\rm max} = 0.2$ in the momentum driven case as in Furlanetto et al. (2017). We also assume that some fraction of newly accreted gas may be virial shock heated and be unavailable for star formation. We follow Faucher-Giguère et al. (2011), who find the fraction of accreted material that will be able to cool onto the halo and form stars to be

$$f_{\rm cool} = 0.47 \left(\frac{1+z}{4} \right)^{0.38} \left(\frac{M_h}{10^{12} M_\odot} \right)^{-0.25}. \tag{2.22}$$

This fraction is only less than 1 in the case of very massive halos at relatively low redshifts, so we find that this process does not have a large effect on our results.

We compare our results to to the observed luminosity functions of Bouwens et al. (2015) in Fig. 2.2.[2] We find reasonable agreement for our models at $z = 7$, although our model overpredicts the abundance of halos at $z = 10$. This was seen as well in Furlanetto et al. (2017), who alleviated this discrepancy by including a redshift independent model of Pop II star formation which fits the data better. We also include this model, which is identical to

---

[2]We note that other groups have produced luminosity functions at these redshifts (e.g., McLure et al., 2013; Oesch et al., 2013; Schenker et al., 2013; Bowler et al., 2015; Finkelstein et al., 2015) that are generally consistent with our results. The Finkelstein et al. (2015) data has a lower amplitude than our results and those of Bouwens et al. (2015), although their shape is similar so this does not affect the model significantly as the amplitude is degenerate with our assumptions on the star formation efficiency. See Mirocha et al. (2017) and Mason et al. (2015) for more detailed comparisons.
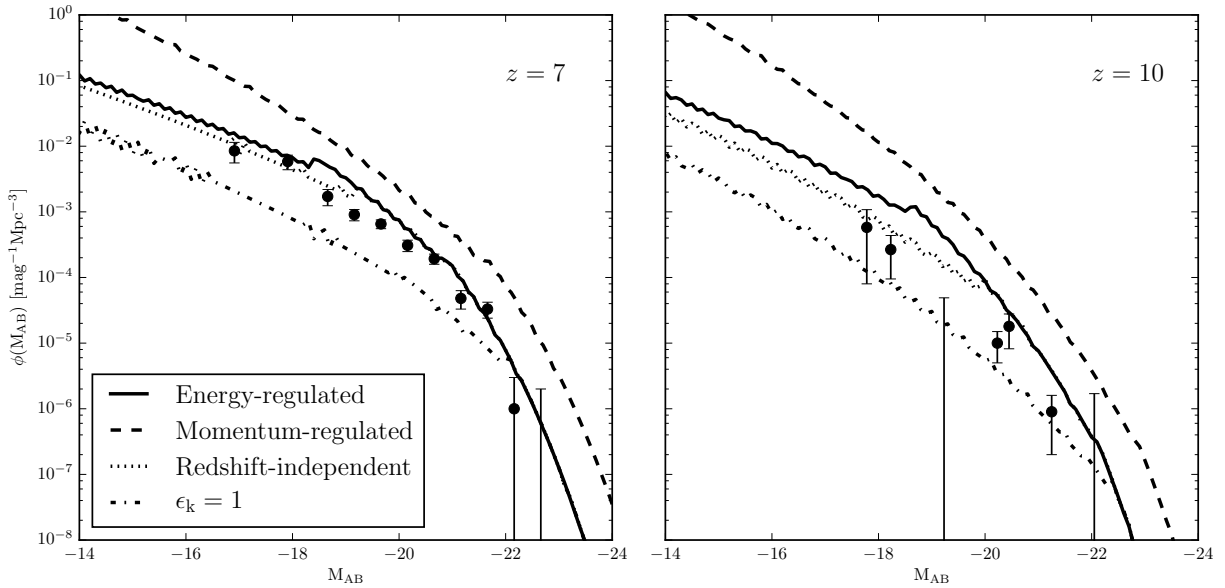
Figure 2.2: Luminosity functions for Pop II stars in our fiducial model compared to the observed luminosity functions of Bouwens et al. (2015). We do not include the luminosity functions for Pop III stars as they are far too dim. In general, our results agree reasonably well with the data at $z = 7$, but the energy- and momentum-regulated models overpredict the abundance of halos at $z = 10$. We therefore also include a redshift-independent model which fits the data better. Finally, we include an energy-regulated model with $\epsilon_k = 1$ (i.e., all of the kinetic energy released by supernovae couples to a halo's gas to drive a wind).

the energy-regulated model at $z = 8$ with $\epsilon_k = 0.2$ but ignores the redshift dependence in equation (2.19).

2.5 Results

With all the components of our model in place, we now consider how our ensemble of halos evolves through the Pop III era. In our fiducial model:
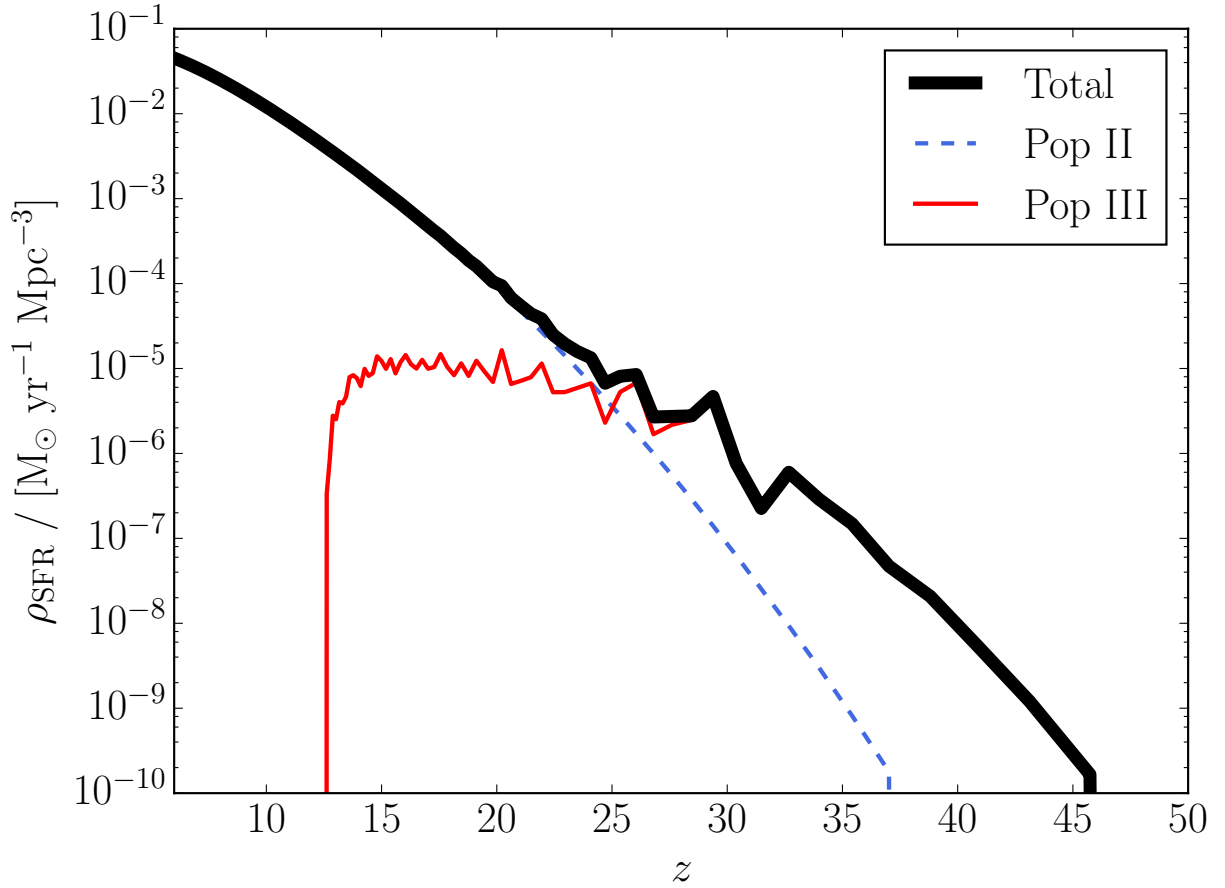
Figure 2.3: Star formation rate density of minihalo Pop III and Pop II star formation in our fiducial model. This mode of Pop III star formation ends in our model once the minimum mass for star formation rises above the atomic cooling threshold (see Fig. 2.8).

1. We assume a Salpeter IMF from 20 $M_\odot$ up to the limit in equation (2.10) (henceforth referred to as "low-mass" in comparison to more extreme models; see Table 2.1).

2. We set the gas re-accretion time equal to the halo free-fall time.

3. We assume that each star formation event generates just a single star or pair of stars, and we set the binary fraction to 0.5.

4. We assume energy regulation (eq. 2.19) for the Pop II phase.

5. We take the Trac et al. (2015) halo mass function and set the halo growth rate via abundance matching.

We also consider a broad set of variations around these fiducial values.

Fig. 2.3 shows the total, minihalo Pop III, and Pop II star formation rate densities of our fiducial model.[3] We see that Pop III star formation in minihalos gradually rises until $z \sim 25$, when the Lyman-Werner background has grown enough to narrow the allowed mass range of Pop III halos sufficiently to begin the decline in star formation (see Fig. 2.4). Note how minihalo Pop III stars are able to dominate the Lyman-Werner background for a relatively long ($z \sim 20$ instead of $z \sim 25$) time, even though Pop II star formation has come to dominate the star formation rate densities much earlier (Fig. 2.3). Since massive Pop III stars produce more UV photons per unit mass, small star formation rates can still create a large Lyman-Werner background. As this is happening, Pop II star formation continues to rise as more Pop III halos retain enough metals to make the transition, continuing until $z \sim 25$ where Pop II star formation finally begins to dominate the total star formation in the Universe. After this, minihalo Pop III star formation still continues on until $z \sim 12$, albeit at a much lower level than the total star formation. It is at this point that the minimum mass

---

[3]The fluctuations in these curves are caused by our finite number of mass bins. Since the mass range in which halos are actively forming Pop III stars is relatively narrow, individual halos turning their star formation on or off are seen as features in the star formation rate density.

for Pop III star formation rises above the atomic cooling threshold, cutting off the formation of any new Pop III stars in minihalos.

We next explore the origins of these features and their robustness in different scenarios of early star formation.

2.5.1 Pop III Star Formation in Individual Minihalos

To that end, we next consider the star formation histories of single halos. These are seen in Fig. 2.5, which shows the total Pop III stellar mass formed in example halos of three different masses. The burstiness of star formation is reflected in the discrete increases in the total mass when new stars are formed. Note that the halos which form latest – and hence in our prescription have the smallest masses – produce a *larger* number of minihalo Pop III stars than their more massive counterparts, even though the latter began forming their stars much earlier. This is due to the redshift dependence of the binding energy of a halo: at fixed halo mass, $E_b \propto (1+z)$ from eq. (2.15). This allows a halo that forms earlier to become stable to supernovae feedback much more quickly, and it can therefore retain its metals after fewer periods of star formation.

Typically, minihalos go through no more than ~ 10 periods of Pop III star formation, with a delay which depends on the accretion rate of the halo. In a halo with a smaller accretion rate, it may take a few million years to accumulate enough mass to form a single cloud above the local Jeans mass if supernovae from previous episodes have cleared out the halo. In halos with large accretion rates, however, star formation may be able to begin again with virtually no delay. There is much stochasticity in this relationship, however, as can be seen in Fig. 2.6. This is due to our Monte-Carlo treatment of the minihalo Pop III star formation, where stars are randomly sampled from an IMF. If the IMF produces a significant number of stars which will not end their lives in a supernova (such as in the low-mass IMF model
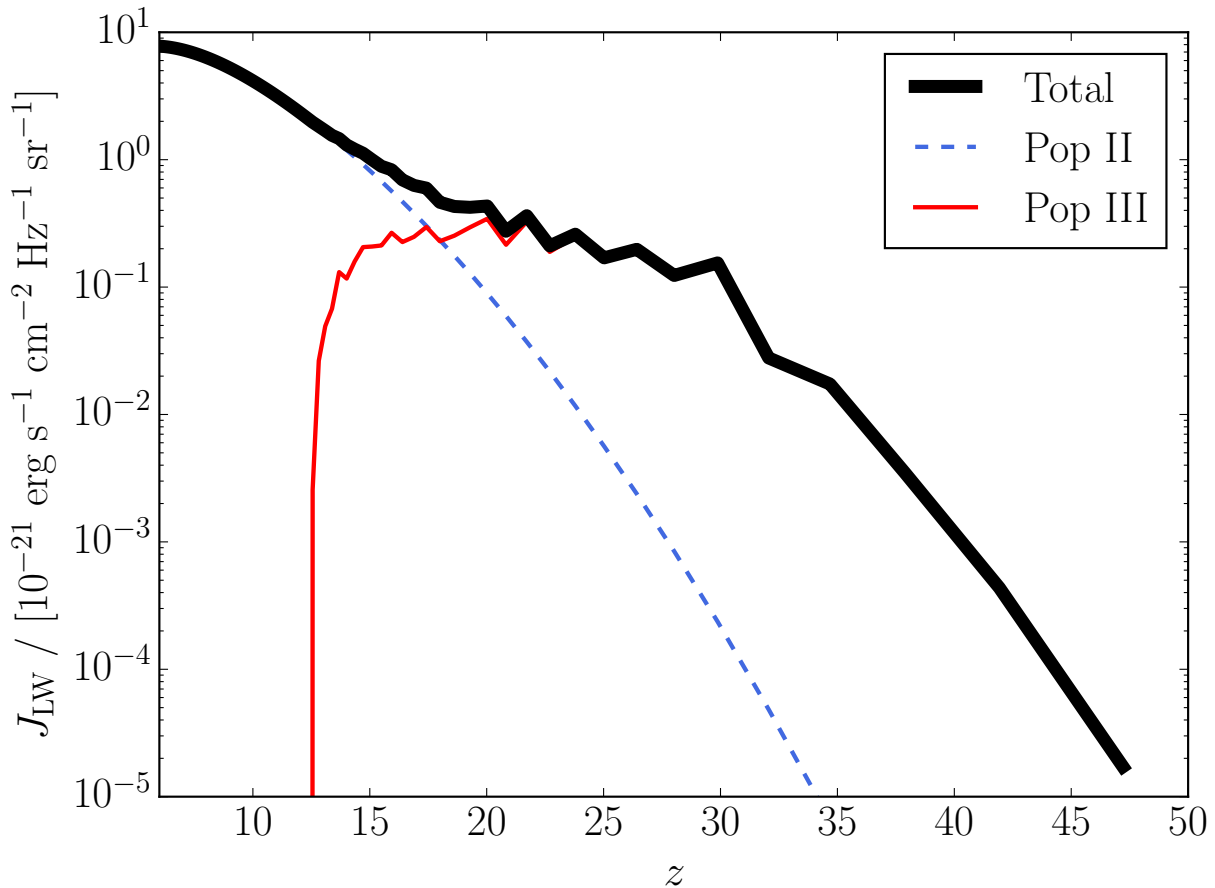
Figure 2.4: Lyman-Werner background for our fiducial model. Note how the contribution from Pop III stars in minihalos is dominant for longer than the star formation rate densities in Fig. 2.3. This is because these Pop III stars are able to produce UV photons more efficiently than their Pop II counterparts, so even a small amount of Pop III star formation can continue to produce a high Lyman-Werner background.

shown here), a halo can "forget" about earlier generations of Pop III star formation as any metals produced will be lost to the black hole.

We find that halos in our model generally tend to become stable to supernovae shortly before reaching the atomic cooling threshold. In fact, most halos which transition by reaching the critical metallicity will end up crossing this threshold within the next $\sim$10 Myr, causing the minimum mass for Pop II star formation to be very close to the atomic cooling threshold. Our results therefore generally support assumptions made in previous works that metal-enriched star formation will only occur in halos above the atomic cooling threshold.

Our model allows for a minihalo which has formed Pop III stars in the past to fall below the minimum mass and cease star formation. This could, in principle, allow halos to stay dormant after a few earlier periods of star formation. In practice, however, we find that this does not happen, as halos tend to grow faster than the minimum mass, at least until the Lyman-Werner background has grown large enough to completely shut off Pop III star formation in minihalos.

2.5.2 The Duration of Pop III Star Formation in Minihalos

The key question we wish to address in our models is how long Pop III star formation in minihalos persists under a variety of physics assumptions. Figure 2.7 shows this for our suite of models. We find that, generically, the star formation rate density increases rapidly at early times before slowing dramatically or flattening. This "plateau" period is typically comparable to the age of the Universe at that time before minihalo Pop III star formation ends entirely. Extended Pop III star formation such as this is also seen in the Renaissance Simulations (see Xu et al., 2016).

We also track the formation of the first generation of Pop III stars in atomic cooling halos (see section 2.3.5). This "Pop III.2" star formation is shown for our fiducial model in Fig. 2.7,
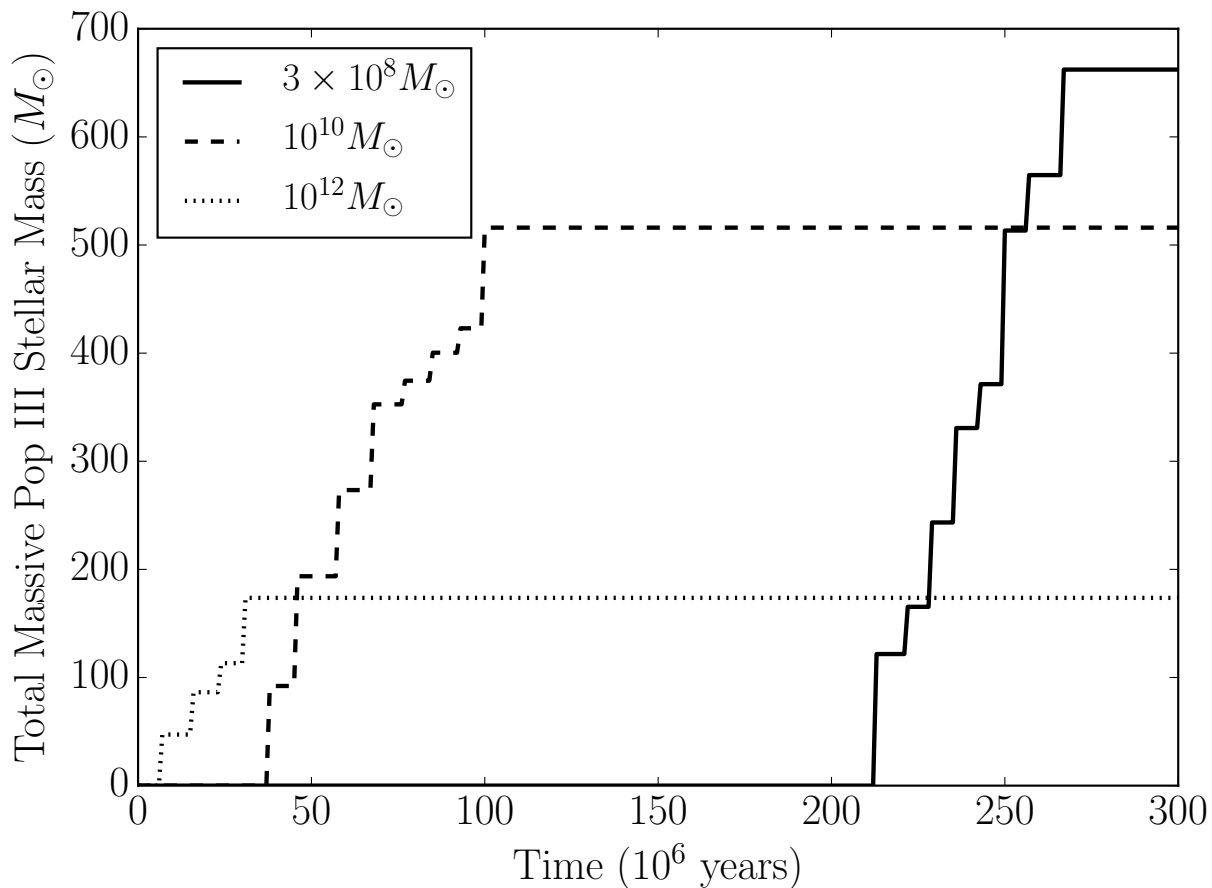
Figure 2.5: Total minihalo Pop III stellar mass for three example halos of different masses. In general, halos that form later have more periods of star formation, which leads to a higher total mass produced. Masses shown are the final masses at $z = 6$.
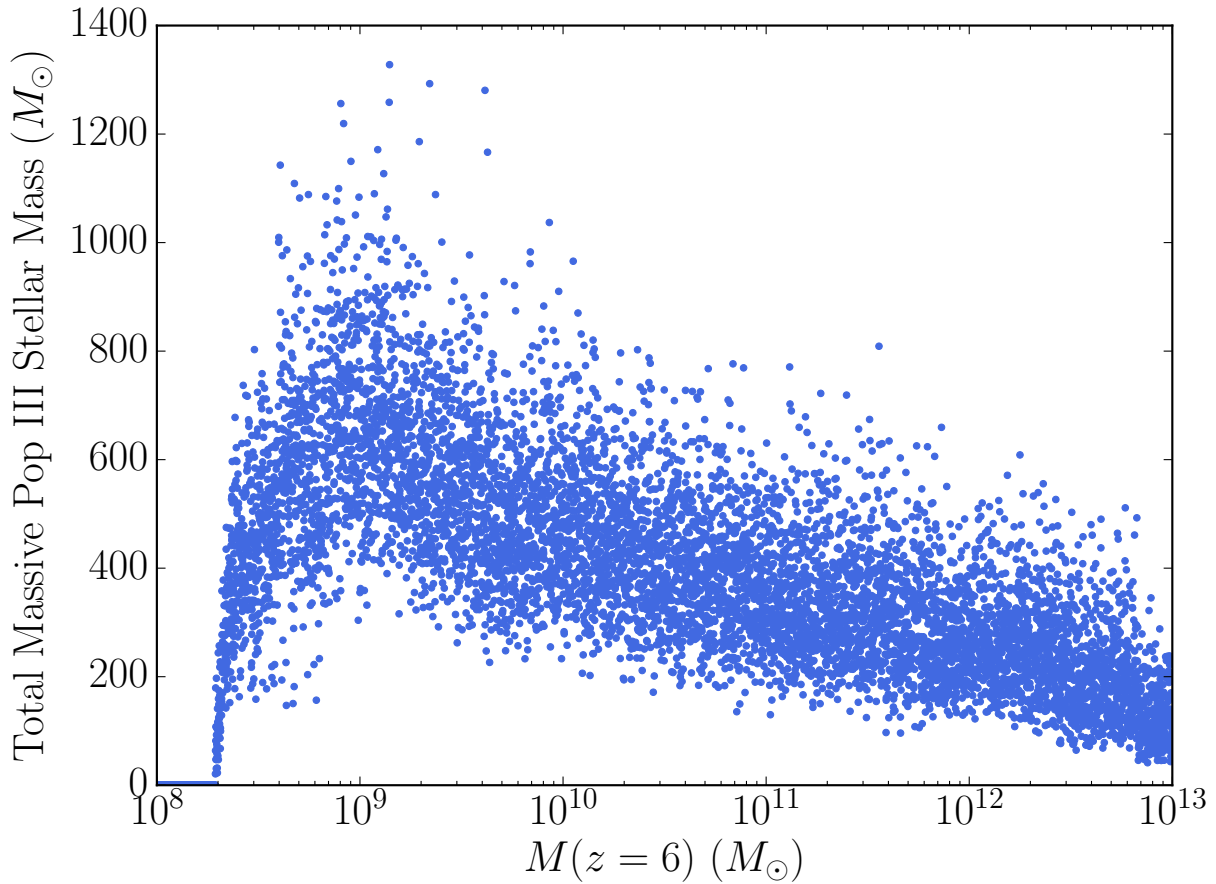
Figure 2.6: Total mass of Pop III stars formed in halos by $z = 6$ as a function of mass. Each point corresponds to a halo in our fiducial model. Note that, since stars in our model form in isolation and will always die before the next period of star formation, this mass is not the total mass of Pop III stars at $z = 6$. Rather, this is the total mass that has formed in the halo, as most of the stars will have either exploded in a supernova or collapsed to a black hole.

and we see a similar result for all other models. This mode of star formation tends to occur at least an order of magnitude below the Pop III star formation in minihalos, although it has a much longer tail as new halos which have yet to form stars cross the atomic cooling threshold and become more stable to supernovae. Of course, this ratio is a result of our assumption that only the *first* burst of star formation in these halos is Pop III, and the SFRD could be much larger if the metals mix inefficiently (see Sarmento et al. 2018).

The reason for the decline and end of minihalo Pop III star formation is seen in Figs. 2.4 and 2.8. As the Lyman-Werner background begins to build up at a faster rate when halos transition to Pop II star formation, the minimum mass rises. As it gets closer to the atomic cooling threshold, the mass range in which minihalos are able to form Pop III stars narrows, causing the star formation rate density to begin to plateau. Once the minimum mass rises above the atomic cooling threshold, this mode of Pop III star formation ends.

2.5.3 The Importance of Pop II Stars for Minihalo Pop III Star Formation

As seen in the bottom panels of Fig. 2.7, the Pop III star formation rate densities in models with momentum regulated Pop II star formation are quite distinct from those with energy regulated Pop II star formation. Because the star formation efficiency is higher in low mass halos (which are very abundant at these redshifts) under momentum regulation, the Lyman-Werner background and minimum mass of Pop III halos rise much more quickly. This is seen in the plots of star formation rate density as a much earlier transition to Pop II star formation, which generally occurs at around the same time as the plateau. Also, since we transition away from Pop III star formation once minihalos pass the atomic cooling threshold and become more stable to supernova feedback, all new halos will skip this phase of star formation and begin forming stars following the Furlanetto et al. 2017 model at this point (see Fig. 2.8).
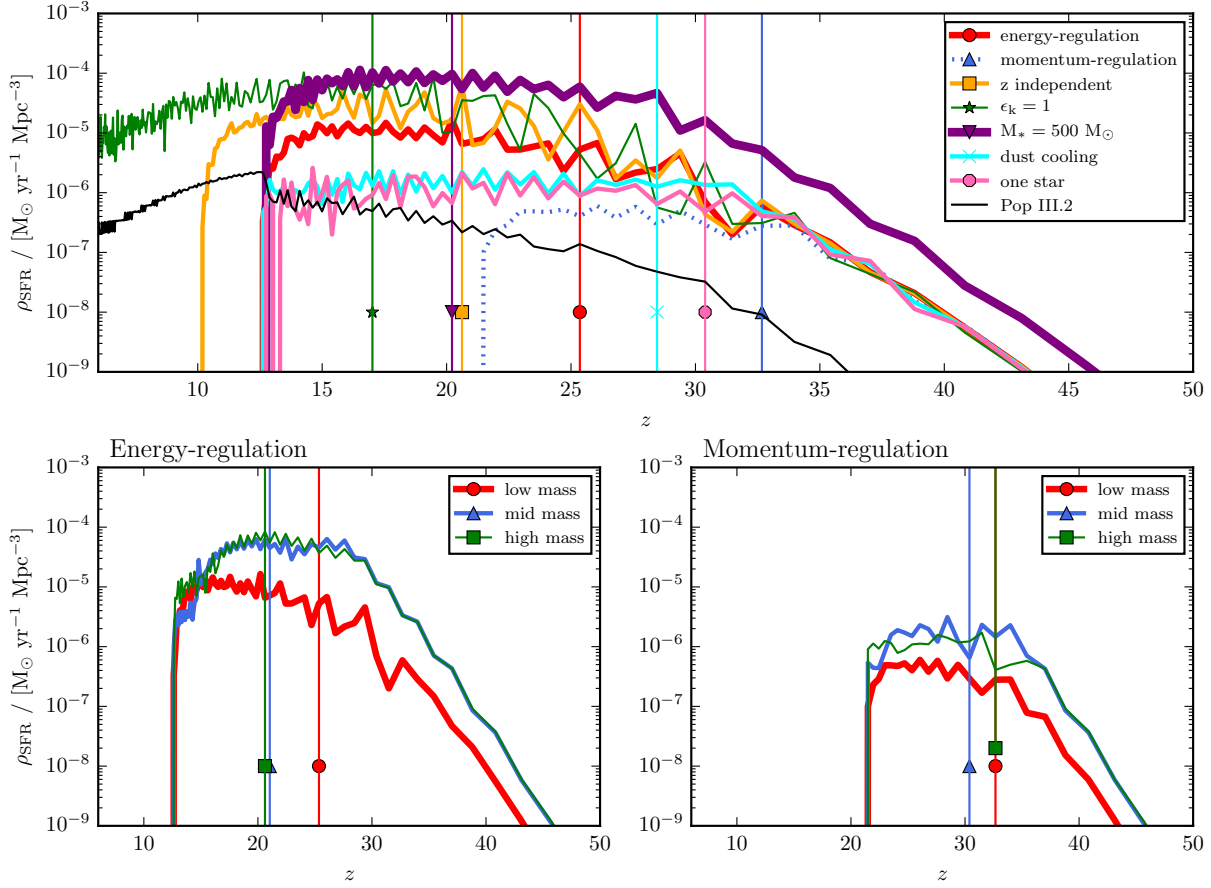
Figure 2.7: Star formation rate density of minihalo Pop III stars for a variety of our models. Symbols indicate where Pop II star formation overtakes Pop III star formation. The upper panel shows our results for a low mass Pop III IMF under a variety of different assumptions for the Pop II and III star formation prescriptions. The bottom panels show a comparison between three different Pop III IMFs using energy- and momentum-regulated Pop II star formation, respectively. Note that models which employ momentum-regulated Pop II star formation will form stars more efficiently in low-mass halos, raising the minimum mass above the atomic cooling threshold faster and transitioning from the minihalo Pop III phase sooner.
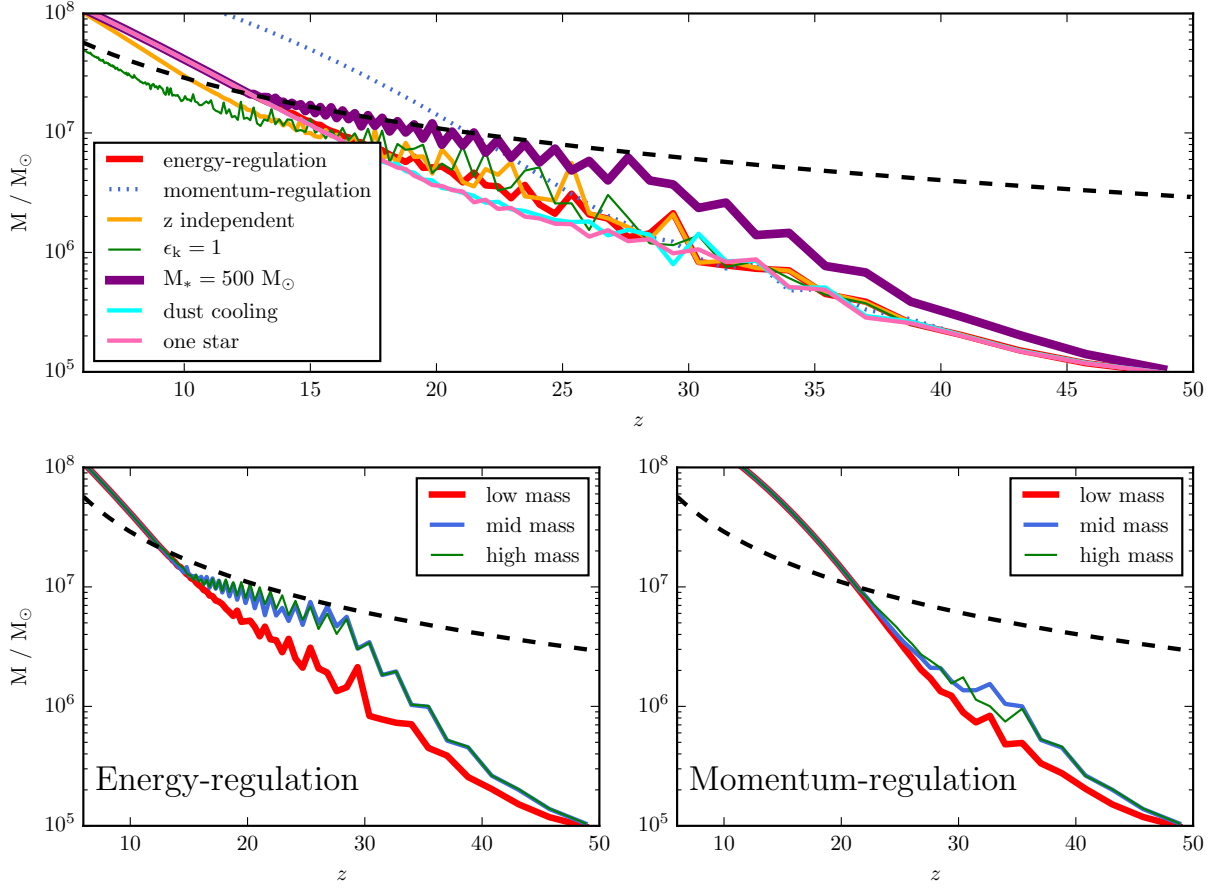
Figure 2.8: Minimum mass for Pop III star formation for a variety of our models. The atomic cooling threshold is shown as the dashed line. The top panel shows our results for the low mass Pop III IMF under a variety of different assumptions for the Pop II and III star formation prescriptions. The bottom panels compare our results for different Pop III IMFs using the energy- and momentum- regulated Pop II star formation prescriptions. Once the minimum mass crosses the atomic cooling threshold, any new halos will begin forming low-mass stars, even if they form out of primordial gas. This is why the Pop III star formation rate density vanishes so quickly in the momentum regulated models.
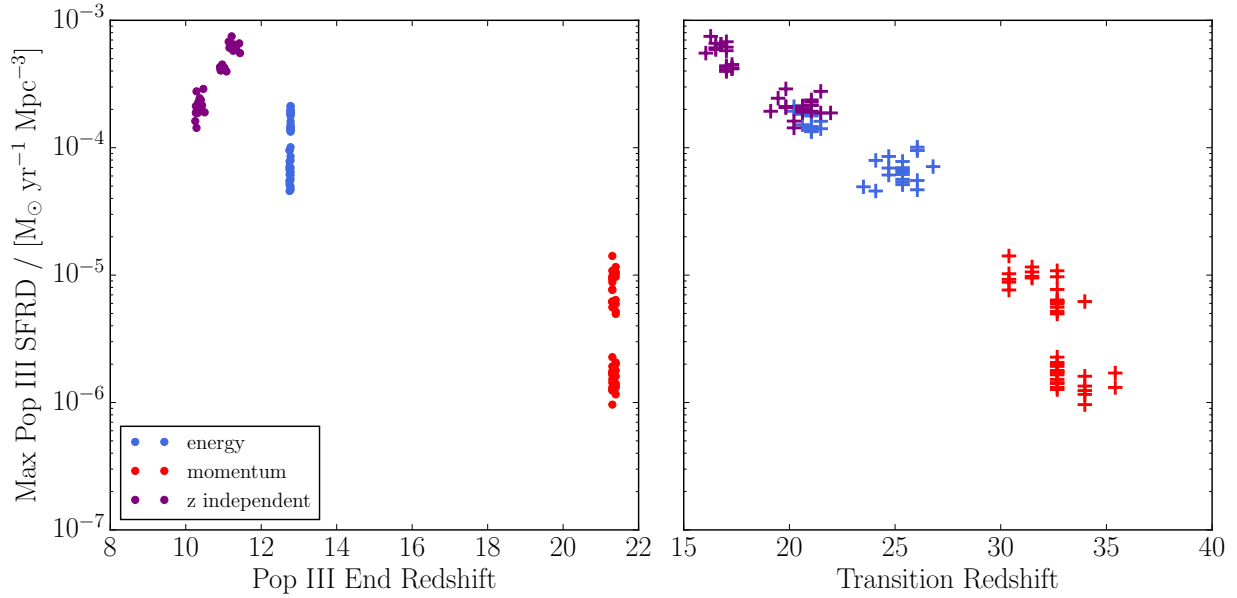
Figure 2.9: Maxmimum Pop III star formation rate densities and important redshifts for a number of different Pop II star formation prescriptions. Points correspond to the ending redshift of Pop III star formation in the left panel, and crosses correspond to the redshift at which Pop II star formation overtakes Pop III in the right panel. Scatter for each model is caused by varying IMFs as well as our Monte Carlo approach to model Pop III star formation. Note how there is very little scatter in the Pop III end redshift within each Pop II model. By the time Pop III star formation ends, the Lyman-Werner background is completely dominated by Pop II star formation, so all models typically end at the same time.

The IMF appears to have a more pronounced effect in the cases with energy-regulated star formation. In the case of the mid- and high-mass IMFs, the minimum mass follows the atomic cooling threshold before finally crossing it when Pop II star formation is high enough. With more massive stars, the contribution to the Lyman-Werner background from minihalo Pop III stars is larger, allowing these stars to more effectively regulate themselves near the atomic cooling threshold. Pop III star formation inside minihalos does not entirely cease, however, until Pop II stars contribute enough to the Lyman-Werner background to completely shut off star formation by themselves.

Figure 2.9 illustrates these points for a wide range of model parameters. It shows two key transition points for several of our models. The left panel shows z_{end}, the times at which Pop III star formation in minihalos ends for each model. The right panel shows z_{II}, the moments at which the Pop II SFRD overtakes the Pop III SFRD in each model. Within a given Pop II model, there is very little spread in the redshift at which minihalo Pop III star formation ends. This is due to the fact that, by the time this happens, the Lyman-Werner background is completely dominated by Pop II stars. Fig. 2.8 shows this as well: for a given Pop II prescription, all the minimum mass curves cross the atomic cooling threshold at the same time, which marks the final endpoint of Pop III star formation in minihalos. However, there is quite a bit of scatter in the maximum star formation rate density at this time, because that depends more sensitively on our assumptions about the Pop III stars. In fact, there appear to be two distinct "clouds" for each Pop II star formation prescription in the plot. This is caused by our choice of IMF models, which separate (relatively) low- and (extremely) high-mass stars into contrasting cases. Because the prescriptions both form individual stars, the high-mass case produces about an order of magnitude more stellar mass per event, which directly affects the maximum star formation rate density. If we utilized a wider range of IMF models which uniformly spanned the relevant ranges in stellar mass, these "clouds" would be connected.

The transition redshift z_{II} also has a moderate amount of scatter, because it depends upon the amplitude of the Pop III star formation rate density, which is sensitive to our assumptions. It is apparent that, in all of our models, the minihalo Pop III era never reaches more than $\sim 10^{-3}$ $\mathrm{M}_\odot$ Mpc^{-3} yr^{-1}, and in most cases much less. This is comparable to the measured SFRD at $z \sim 10$ from *bright* galaxies (Zheng et al., 2012; Coe et al., 2013; Oesch et al., 2014; McLeod et al., 2015; Atek et al., 2015), although in our models the total Pop II SFRD is always much larger by $z \sim 10$. This illustrates the difficulty of detecting the extremely faint Pop III halos, if they exist.

Figures 2.7 and 2.9 also show that the redshift independent case (which matches the observations best at $z = 10$) yields a slightly more extended Pop III star formation history, as it produces a smaller rate of star formation in low mass halos. As an extreme case, we also include in Figure 2.7 a model with energy regulated Pop II star formation, but with $\epsilon_{\mathrm{k}} = 1$. In other words, all of the kinetic energy released by supernovae in this model is able to couple to the gas and work to lift it out of the halo. Since feedback is stronger in this case, we see a smaller Pop II star formation efficiency in halos, and therefore a lower Lyman-Werner background. As a result, the minimum mass to produce Pop II stars never crosses the atomic cooling threshold. Because of this, Pop III star formation in minihalos is able to continue on until at least $z = 6$. However, Figure 2.2 shows that this model substantially underpredicts the observed luminosity function at $z \sim 7$. We include it only to emphasize that the longevity of the minihalo Pop III phase is very sensitive to the details of Pop II star formation in low-mass halos.

2.5.4 Self-Regulation of Pop III Star Formation

In order to test the ability of Pop III stars in minihalos to self-regulate themselves, we next consider a model in which Pop III stars do not contribute to the Lyman-Werner background by setting $\mathrm{N}_{\mathrm{LW}} = 0$ for Pop III stars. The minimum mass of Pop III halos for this case is

shown in Fig. 2.10. The Lyman-Werner background and therefore minimum mass will be lower at early times when Pop III star formation is dominant. Without a Lyman-Werner background, halos form Pop III stars earlier. But the time at which the minimum mass crosses the atomic cooling threshold is unchanged, because it is feedback from Pop II stars which eventually causes Pop III star formation to end inside minihalos. Because of this, while Pop III stars may be able to regulate their own minimum mass at early times, global Pop III star formation will not be terminated by feedback from Pop III stars.

2.5.5 Comparison to Other Works

Our model can be compared to similar models of Pop III star formation which use different approaches and study the effect of other parameters. Because this phase of star formation has yet to be observed, there are many uncertainties, and it is important to consider a wide range of models. We find that many of our results generally agree with the numerous other models of similar nature, although there are some distinct differences due to our specific assumptions.

For example, Jaacks et al. (2018) run a hydrodynamical simulation where Pop III supernova remnants are "painted" onto the fluid with their properties calibrated from simulations and analytical arguments. They assume a fixed mass of ~ 500 M$_\odot$ per star formation event once a gas particle passes the thresholds of $n = 100$ cm^{-3} with $T \leq 10^3$ K. They find, like us, that Pop III star formation is not a self-terminating process. However, we come to this conclusion differently. They find that halos are simply not able to produce enough metals to raise the volume-averaged metallicity of their box above the critical metallicity required for Pop II star formation. In our models, we find instead that Pop III stars in minihalos never form rapidly enough to raise the Lyman-Werner background high enough to completely cut off star formation in halos below the atomic cooling threshold on their own. We must instead wait until Pop II star formation begins to dominate. We also find that, even if minihalo
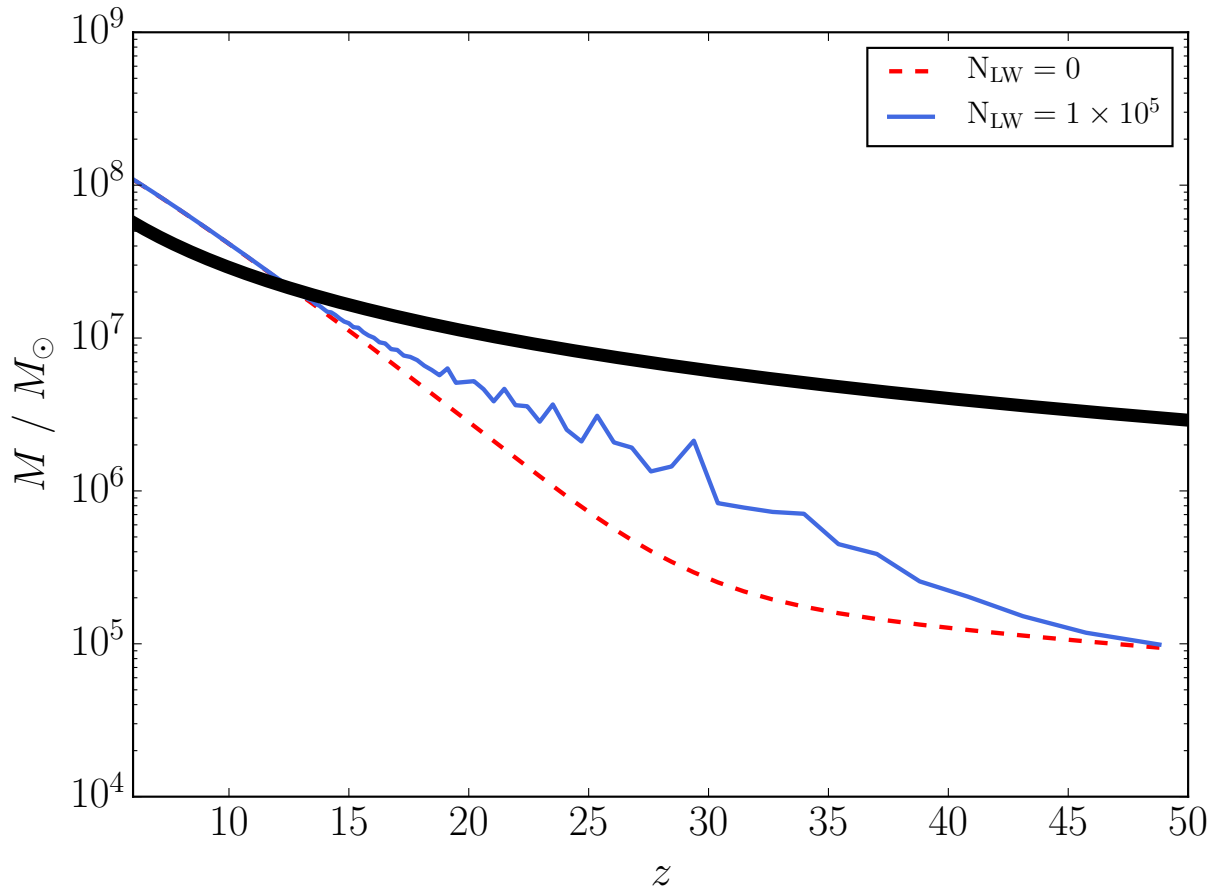
Figure 2.10: Minimum masses for Pop III star formation for varying values of N_{LW}. The minimum mass is higher in the case where Pop III stars contribute to the Lyman-Werner background, although all cases rise above the atomic cooling threshold at the same time. This indicates that global feedback from Pop II star formation is really what ends the Pop III phase in the universe.

Pop III stars do not contribute at all to the Lyman-Werner background, star formation will still end at the same time (see section 2.5.4). They also find a maximum star formation rate density of around 10^{-3} M$_\odot$ yr^{-1} Mpc^{-3}, however, which is about an order of magnitude higher than the star formation rate densities found in most of our models.

In order to fully compare with their results, we include a model which also forms a fixed mass of 500 M$_\odot$ per star formation episode. We note that, even under this assumption, we still find a star formation rate density about an order of magnitude smaller than theirs. This model is shown in Figs. 2.7 and 2.8. In this case, the minimum mass is higher before Pop III star formation ends, because more stars form and the Lyman-Werner background is larger. However, the redshift at which minihalo Pop III star formation ends is virtually unchanged, because by that point Pop II star formation dominates by far. Thus this model can lead to a slightly larger Pop III star formation rate density in minihalos (though still about an order of magnitude smaller than that of Jaacks et al. 2018) but does not affect our major conclusions. Halos in this model tend to have a similar number of minihalo Pop III star formation episodes as halos in our fiducial models, as the increased star formation results in more energy injected into the system from supernovae. While more metals are produced, they are much more easily ejected out of the halo, causing halos to be unable to transition due to reaching the critical metallicity. Thus, these halos tend to transition away from minihalo Pop III star formation simply by reaching the atomic cooling threshold.

The differences between our models and those of Jaacks et al. (2018) are mainly caused by different assumptions about the Pop II star formation rate density. Their models have systematically lower star formation in the Pop II phase than ours (their eq. 21), causing a lower Lyman-Werner background and therefore minimum mass. They also assumed lower values of $N_{\rm LW}$ for both Pop II and Pop III stars (by factors of 5 and 10, respectively), exaggerating the decline in the Lyman-Werner background.

Visbal et al. (2018) apply a semi-analytic model to N-body dark matter simulations, allowing

them to take into account any processes which require spatial information such as clustering and mergers. They allow stars to form at a specific fraction of a halo's baryonic mass, fiducially taken to be 10^{-3} (we find $\sim 5 \times 10^{-4}$ for the total Pop III stellar mass formed in a minihalo in our fiducial, low-mass model). They find star formation rate densities consistent with ours, although their models only run to $z \sim 20$ so it is difficult to compare any results which rely on feedback from Pop II stars, such as the duration of Pop III star formation in the universe. They do find that the effects of external metal enrichment may be important only if metals are allowed to travel far from their original halos. This is similar to Jaacks et al. (2018), who find that small halos which are externally enriched exhibit much lower metallicities than more massive halos which are internally enriched by their own star formation. While we do not include the effects of external enrichment in our model, we note that it would work to transition halos faster, potentially turning the plateau seen in many of our star formation rate densities into a more gradual decline.

Trenti & Stiavelli (2009) use a semi-analytic model similar to ours with dark matter halos from the Press-Schechter formalism (Press & Schechter 1974). They find star formation rate densities comparable to ours in cases where Pop III stars form in isolation. They also study the importance of Pop III stars forming in halos above the atomic cooling threshold. This form of star formation was only important when Pop III stars were allowed to form with efficiencies much larger than what is found in our models, even in the cases where multiple generations of Pop III stars can form per halo.

Crosby et al. (2013b) carry out a semi-analytic model based on dark matter halos from numerical simulations. They use a similar model for the ejection of metals produced by Pop III supernovae as in this work, although they find, in contrast to us, that halos are generally able to retain enough metals to transition to Pop II star formation after the first supernova. This is because they assume a substantially smaller fraction of a supernova's total energy is used to drive outflows from a halo. Their star formation rate densities are

therefore lower than our fiducial model by about an order of magnitude.

Maio et al. (2010) use a detailed set of numerical simulations spanning a wide range of parameters to study the onset of metal-free Pop III star formation and the transition to metal-enriched Pop II stars. They find star formation rates densities that plateau to values comparable or less than ours for their range of models. Similar to us, they also explore the effects of different Pop III IMFs which may drastically change the relative number and energy of their supernovae. They find that high mass IMFs generally result in a lower star formation rate density as these stars will produce more supernovae quicker and enrich their halos faster. As shown in the bottom panels of Fig. 2.7, we find the opposite result as higher mass stars will be able to blow out metals easier due to their higher supernova energies, therefore allowing Pop III star formation in minihalos to persist for longer.

Many of these models make the assumption that only one Pop III star forms per halo before making the transition to Pop II star formation. We include a model with this feature for comparison (see Fig. 2.7). Since halos in our fiducial model generally have ~ 10 periods of Pop III star formation, the resulting star formation rate density is lower by around an order of magnitude.

2.6 Caveats

In this section we describe some of the simplifications of our model and their consequences.

2.6.1 Mass Growth Rates

In Fig. 2.1 we compare not only halo growth from our abundance matching technique, but also growth histories from the Trac et al. (2015) fit to eq. 2.2. In this case, halos which will end up with the same mass at $z = 6$ will be less massive by a factor of order unity at $z = 50$.

These halos will therefore take slightly longer to cross the minimum mass and form their first Pop III star. For example, in models using these accretion rates, the first Pop III star will form at $z \sim 40$, compared to $z \sim 45$ in our fiducial models. Once Pop III star formation begins to plateau, however, the two models become very similar. Because this assumption does not affect Pop II star formation, the Lyman-Werner background is the same at later times, causing minihalo Pop III star formation to end at the same time in both cases.

2.6.2 Mergers

Our fiducial model assumes that halos grow primarily through smooth accretion from the IGM. While Behroozi & Silk (2015) have shown that this is the primary source of growth for halos at high redshift, it is possible that mergers could also play an important role. In our model, the primary way in which mergers could change our results is if combining the metals produced in two merging halos allowed the halo to transition to the Pop II phase sooner than it would have on its own. However, we find that only a narrow range of minihalos are able to form Pop III stars at any given time. Thus, with the exception of major events, only the larger mass progenitor would have been capable of creating stars in the past, so the smaller halo would have no metals to contribute. Even if it did, merging two halos currently forming Pop III stars would still not cause a halo to exceed the critical metallicity unless one of the halos had already transitioned, as both the halos' gas and metals would be mixed. Because of this, we neglect the effect of mergers in our model. Nevertheless, we plan to investigate the effects of mergers in more detail in the future.

2.6.3 Metal Retention and the Critical Metalicity

In order to test the importance of our Maxwell-Boltzmann treatment of the ejected gas as discussed in section 2.3.4, we include an alternate prescription in which we fix the fraction

of metals left behind after supernova feedback. Since Pop III stars are able to produce such high masses of metals (see Table 2.1), we find that even if only a very small fraction ($\sim$5%) of metals remain inside the halo after a supernova event, halos will *immediately* transition to Pop II star formation. This is shown in Fig. 2.11, where a halo that retains 1% of its metals is able to stay in the Pop III phase for multiple episodes of star formation, while a halo with 5% will transition much more quickly. This has the biggest effect in models which use a Pop III IMF where every star ends its life in a supernova. In our low- and high-mass models, for example, some fraction of stars will directly collapse into a black hole, adding no metals to the halo itself. In this case, no matter how high the metal retention fraction is, a minihalo could go through many periods of Pop III star formation if it happens to have formed a number of stars in mass ranges which do not produce supernovae.

As discussed in section 2.3.5, we also include a case where dust cooling is efficient. In this model, halos can transition to Pop II star formation at a much lower metallicity. We find that this causes individual halos to transition quicker as they do not need to retain as many metals after a supernova. This shows up in Fig. 2.7 as a lower total star formation rate density, although the timing of the Pop III phase remains the same.

2.6.4   Gas Re-accretion

In our fiducial model, we assume that ejected gas re-accretes after one free-fall time, t_{ff}, calculated at the time the gas is ejected. In order to test this assumption, we ran models where this time was set to $1/10t_{\text{ff}}$ and $10t_{\text{ff}}$. In each case, we found results almost identical to our fiducial model. This indicates that re-accreted material is not important for the transition to Pop II star formation, and halos which transition before the atomic cooling threshold do so when they become more stable to supernovae feedback and are able to retain metals produced in current periods of star formation. This is because halos grow very quickly during the early phases of the Pop III era, so they quickly transition from being so fragile
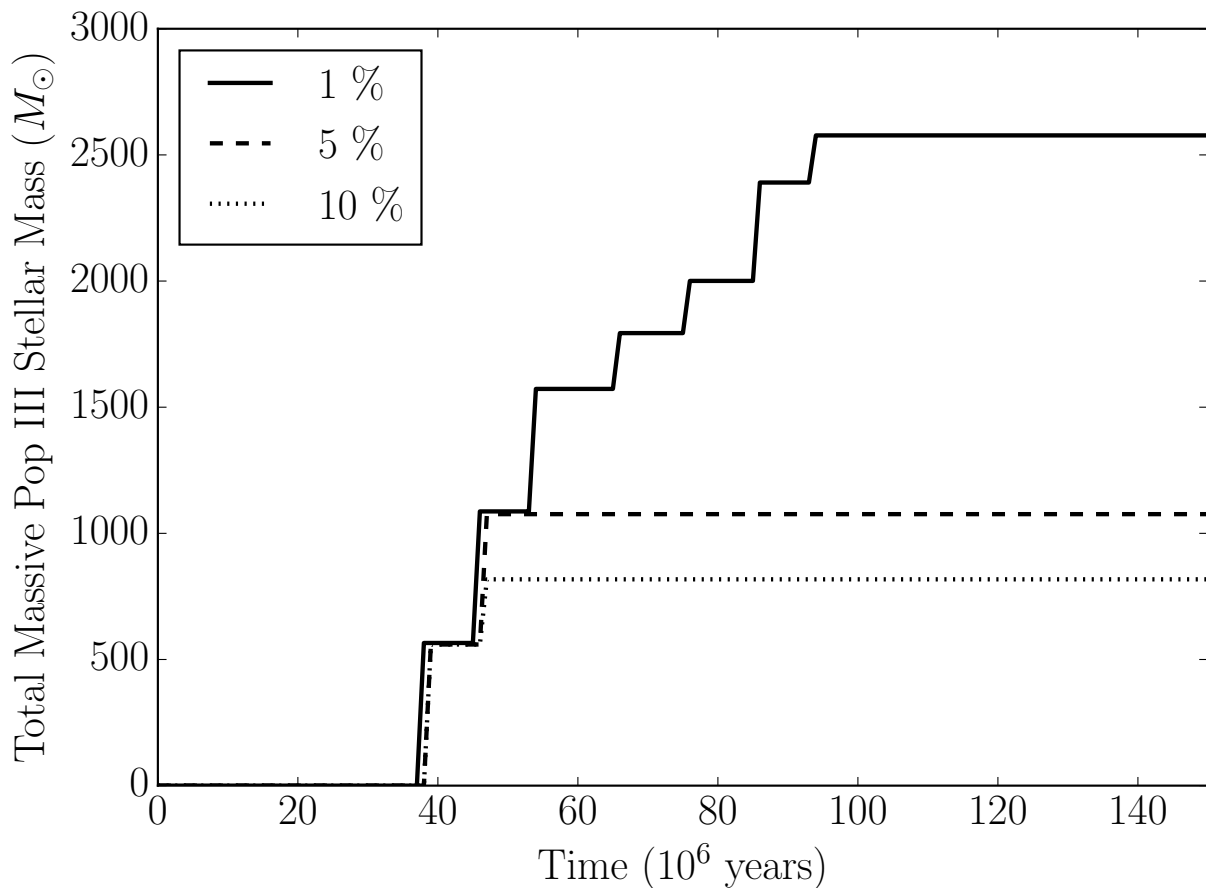
Figure 2.11: Star formation histories of a $10^{10} M_\odot$ halo with various metal retention fractions. Note that the results shown here are for the "mid" IMF in order to ensure every star will supernova and release metals.

that they are completely blown apart by a supernova (with no re-accretion) to being able to retain a fair fraction of their metals.

2.6.5 Photoionization Heating

Although we consider photoionization feedback inside each source's halo, assuming that it limits each halo to a single star forming region at any given time, we do not consider the effects of the photoionization on the gas surrounding the halo. Because the excess energy from ionizing photons typically heats gas to $\sim 10^4$ K, the resulting H II regions will be much hotter than the average IGM. Even if the gas recombines, it will retain excess entropy, which will reduce the rate at which gas accretes onto the host halo (Oh & Haiman, 2003). For simplicity, we ignore the potential of photoheating to suppress accretion onto the small minihalos in which our Pop III stars form, which amounts to assuming that most of the accretion occurs through dense filaments that self-shield from the stellar radiation. If photoheating does suppress accretion, Pop III halos will experience longer delays between star formation episodes. In the most extreme case, accretion would halt until the halos surpass a virial temperature of $\sim 10^4$ K, which we have shown is also approximately the point at which they become stable to supernova feedback. At that point, star formation will likely proceed similarly to our Pop II prescription.

2.7 Observational Implications

2.7.1 Observing Pop III Halos Directly

Unfortunately, the luminosities of Pop III minihalos in our model are very small and well below the capabilities of any current telescopes. We find that the absolute magnitude of these halos can vary between $M_{\mathrm{AB}} \sim -5$ for the lower mass Pop III models to ~ -10 for

the higher mass IMFs. Our models with a fixed mass of Pop III stars are only slightly brighter, reaching $M_{\mathrm{AB}} \sim -10.5$. While these halos are faint, though, they are actually quite abundant. Fig. 2.12 shows the number density of Pop III minihalos for a variety of models. In the cases where Pop III halos are around for the longest, their abundance is actually comparable to that of Pop II galaxies (Fig. 2.2). Unfortunately, Pop III minihalos in our model are far too dim to be detected by any forthcoming instruments, and they would likely require the use of lensing or an even more advanced generation of telescope to detect.

Observations of the luminous Lyα emitter CR7 by Sobral et al. (2015) have indicated the potential presence of a Pop III halo at $z = 6.6$ with a stellar mass of $\sim 10^7 M_{\odot}$. In order to find a halo with these properties in our model, we would have to break our single star-forming region assumption, as it is not possible for us to reach this mass with only a handful of Pop III stars. We would also have to allow halos to form massive Pop III stars in halos above the atomic cooling threshold, as it would otherwise be impossible for a halo to form such a high mass in stars (see Fig. 2.8). Recently, however, ALMA observations of this object have detected [CII] consistent with a normal star forming galaxy, so it is unlikely that CR7 actually contains 10^7 M$_{\odot}$ in Pop III stars (Matthee et al., 2017).

2.7.2 Pop III Supernova Rates

While it is very unlikely that we will be able to directly observe a Pop III minihalo in the near future, it may be possible to observe their supernovae. When a Pop III star with a mass between $140 M_{\odot}$ and $260 M_{\odot}$ reaches the end of its life, it will likely explode in a pair-instability supernova. If Pop III halos form many of their stars in this range (as in our model using McKee & Tan 2008 masses or the high-mass, Salpeter-like IMF), then it may be possible to observe them with JWST or WFIRST. In particular, Whalen et al. (2013) find that Pop III supernovae will be detectable out to $z = 30$ for JWST and $z = 20$ for WFIRST, which is in the redshift range in which our model produces the most supernovae.
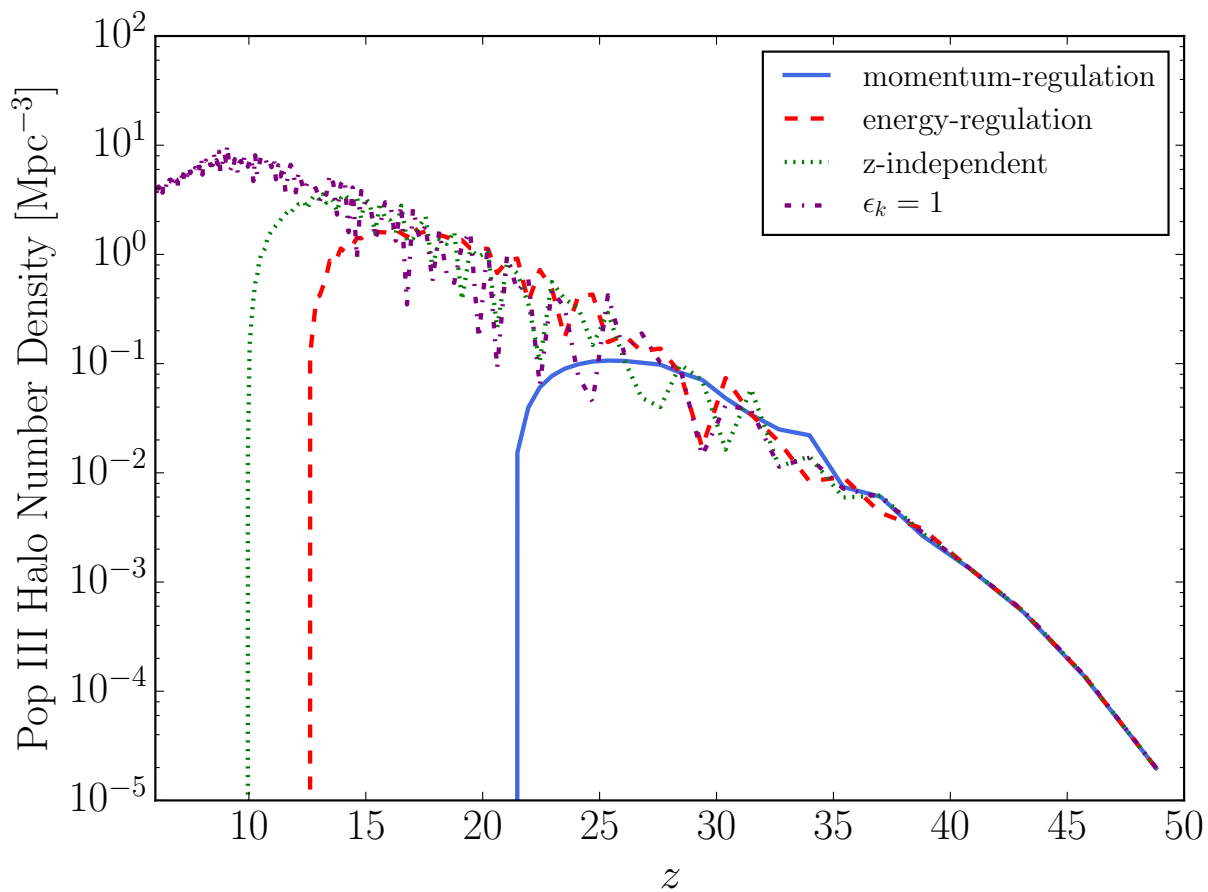
Figure 2.12: Number densities of Pop III halos for a variety of models. This is calculated as the number of halos which are currently forming Pop III stars (i.e, halos in the allowed mass range which have formed a Pop III star in the past and have yet to make the transition to Pop II star formation.)

The Pop III supernova rates from various models are shown in Fig. 2.13. At $z = 20$, an event rate of $\sim 10^{-6}$ Mpc^{-3} yr^{-1} translates to ~ 3 events per year per square degree per unit redshift. Thus, provided minihalo Pop III stars produce luminous supernovae, these events may be within reach of large-scale surveys.

2.7.3 The 21cm Global Signal

Pop III stars will also affect the surrounding intergalactic medium (IGM) through their radiation fields. The sky-averaged ("global") 21-cm signal is a particularly appealing tracer of the IGM as it is sensitive not just to the ionization state, but the temperature and Lyman-α intensity as well. Its sensitivity to the thermal history of the IGM opens up the possibility that X-rays from Pop III remnants could leave traces of their existence, in addition to the impact of Pop III stars themselves.

In Mirocha et al. (2018), we indeed find that the remnants of Pop III stars have a unique impact on the signal. While in general the addition of new sources of X-rays reduces the contrast between otherwise cold neutral regions and the CMB and thus weakens the 21-cm background, Pop III minihalos also give rise to a characteristic asymmetry due to the generic rise and fall of the Pop III SFRD from minihalos. In contrast, models neglecting Pop III sources tend to be quite symmetrical (Mirocha et al., 2017).

2.8 Conclusions

We have presented a simple, semi-analytic model investigating the formation of Pop III stars in minihalos in the early universe and the subsequent transition of their halos to the more traditional Pop II star formation. Our model works by combining the results of a number of numerical simulations and analytic arguments with our self-consistent calculations of im-
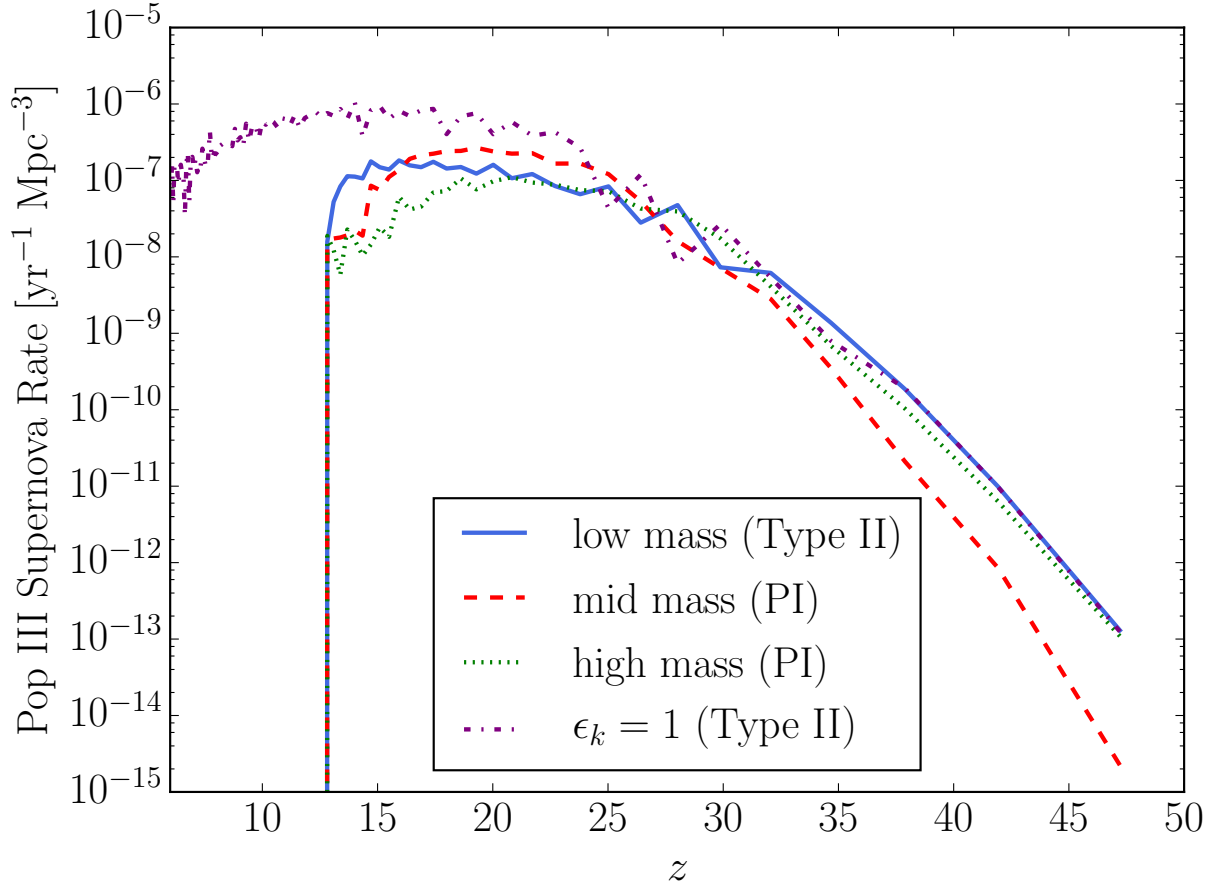
Figure 2.13: Pop III supernovae rates for three of our fiducial models with energy-regulated Pop II star formation. Note that the low mass model does not produce pair-instability supernovae. Whalen et al. (2013) find that these supernovae can be detected by JWST and WFIRST out to $z = 30$ and $z = 20$, respectively, which is where our calculated supernovae rates begin to flatten. The case with energy-regulated Pop II star formation with $\epsilon_k = 1$ is shown as an example of a model which produces Pop III supernovae out to at least $z = 6$.

portant feedback processes such as a meta-galactic Lyman-Werner background, supernovae, photoionization, and chemical feedback. From our results, we conclude that the star formation rate density of minihalo Pop III stars increases rapidly as structure formation generates more halos at very high redshifts, until the stellar population increases enough to generate a substantial Lyman-Werner background, which slows the rate of star formation relative to halo formation. However, because Pop III star formation is limited in each halo by chemical feedback, minihalo Pop III stars are never able to self-terminate globally by generating a dominant Lyman-Werner background. Instead, more massive galaxies forming Pop II stars are ultimately responsible for choking off Pop III star formation in minihalos

More specifically:

1. Depending on our choice of Pop II star formation prescription, Pop III stars can continue to form in minihalos at a low level for an extended period of time, in principle until $z \sim 6$ at rates of around $10^{-4} - 10^{-5}$ M$_\odot$ yr^{-1} Mpc^{-3}. In general, models with efficient star formation in low mass galaxies (i.e., our momentum-regulated model) will cut off minihalo Pop III star formation much earlier by raising the minimum mass required Pop III star formation to occur. Alternatively, inefficient star formation in low mass galaxies (i.e., our energy-regulated model) will allow Pop III star formation in minihalos to last longer.

2. The key parameters driving our results are the Pop II star formation prescription and the Pop III IMF. Secondary effects are the binary fraction, halo mass function, and Lyman-Werner yield of Pop III stars.

3. Supernova feedback is the most important feedback process in a single halo, because efficient expulsion of metals allows Pop III star formation to persist in single minihalos for several generations. On a cosmological scale, the Lyman-Werner background dictates the halo masses at which Pop III stars can form, and it is responsible for stopping

the formation of new minihalo Pop III stars once it causes the minimum mass to exceed the atomic cooling threshold where halos are also more stable to supernova feedback.

4. If metal mixing is inefficient in Pop III halos, metal-free star formation may persist in halos with masses above the atomic cooling threshold. They may from from a different IMF, however, as the cooling channels will be different than in the minihaloes that are the focus of this work.

5. While it may be possible to observe the presence of Pop III stars in minihalos through their supernovae or through cosmological 21-cm experiments, it is very unlikely that we will be able to directly observe a Pop III halo in the near future. Our model produces Pop III minihalos with magnitudes in the range of $M_{\mathrm{AB}} = -5$ to -10 depending on our assumptions of the IMF, which is well below the capabilities of any current instruments.

CHAPTER 3

The Effects of Population III Radiation Backgrounds on the Cosmological 21-cm Signal

3.1 Introduction

The first generation of stars was formed from pristine gas with zero metallicity, and their properties were likely very different from the stars that form today. These early stars, known as Population III (Pop III) stars, are thought to have been very massive and luminous due to the decreased efficiency of molecular hydrogen cooling in metal-free minihalos (Bromm et al., 1999; Abel et al., 2002; Bromm, 2013). Since their birth halos were likely very small with relatively low binding energies, feedback from this form of star formation likely played a crucial role in limiting them to only form in very small clusters or even in isolation (Machacek et al., 2001; Wise & Abel, 2007; O'Shea & Norman, 2008; Shapiro et al., 2004; Visbal et al., 2018). Despite this, however, they must have played a vital role in the evolution of early galaxies as they were the first sources of metals required for more traditional star formation.

As there have been no observations of a Pop III star forming halo, most studies have been in the form of analytical models (e.g., McKee & Tan 2008; Kulkarni et al. 2013), numerical simulations (e.g., Machacek et al. 2001; Wise & Abel 2007; O'Shea & Norman 2008; Xu et al. 2016; Stacy et al. 2012; Hirano et al. 2015; Maio et al. 2010; Sarmento et al. 2018), or semi-analytic models (e.g., Trenti et al. 2009; Crosby et al. 2013a; Jaacks et al. 2018; Visbal

et al. 2018; Mebane et al. 2018). The parameters of this mode of star formation are largely unconstrained, and many models predict that it will be nearly impossible to directly observe a Pop III star, even with the next generation of space telescopes such as JWST. Because of this, we may have to look to indirect observations such as their supernovae or their effect on the cosmological 21-cm background.

The prospect of indirectly detecting Pop III stars through the cosmic 21-cm signal is strengthened by the recent claimed first detection of such a signal by the EDGES experiment last year (Bowman et al., 2018). Their claimed detection was somewhat anomalous when compared to current theoretical predictions of the 21-cm signal. In particular, the trough was deeper than expected, and the timing of the signal was inconsistent with empirically-calibrated models of high-z galaxies extrapolated down to the atomic cooling threshold (Mirocha & Furlanetto, 2019). There has been much discussion of this signal, and potential explanations include, for example, exotic physics, a radio background in excess to the CMB at these redshifts, and new modes of star formation such as metal-free Pop III stars (see, for example Barkana, 2018; Slatyer & Wu, 2018; Hirano & Bromm, 2018; Muñoz et al., 2018; Berlin et al., 2018; Kovetz et al., 2018; Cheung et al., 2019; Moroi et al., 2018; Chianese et al., 2019; Falkowski & Petraki, 2018; Lawson & Zhitnitsky, 2019; Jia, 2019; Costa et al., 2018). One intriguing explanation is that there is a previously unexplained radio background present at high redshift that dominates over the CMB (Feng & Holder, 2018), which requires that only 10% of the excess radio background reported by the ARCADE 2 experiment in Fixsen et al. (2011) is produced at very high redshifts (e.g., Ewall-Wice et al., 2018; Fialkov & Barkana, 2019).

In this paper we investigate the effect of Pop III stars on the global 21-cm signal by combining the Pop III semi-analytic model described in Mebane et al. (2018) with the 21-cm global signal simulation code ARES (Mirocha, 2014). In particular, we consider the potential effects of Pop III stars on the timing, shape, and depth of the 21-cm absorption trough. We ask when UV emission from the stars themselves can naturally trigger the absorption trough,

how rapidly X-ray emission from accreting Pop III remnant black holes can heat the gas and transform the absorption into emission, and finally whether radio emission from these black holes can raise the radio background temperature far enough to affect the amplitude of the absorption. We also examine the differences between various Pop III models and how the environments around their birth halos may alter their effect on this signal.

In Section 3.2 we outline the details of our Pop III semi-analytic model (explained in more detail in Mebane et al., 2018). We describe the details of the global cosmic 21-cm signal in Section 3.3, and we examine the emission properties of Pop III remnants in Section 3.4. We present the results of our model, including our best fits to the EDGES signal, in Section 3.5, and we conclude in Section 3.6.

In this work, we use a flat, ΛCDM cosmology with $\Omega_\mathrm{m} = 0.28$, $\Omega_\mathrm{b} = 0.046$, $\Omega_\Lambda = 0.72$, $\sigma_8 = 0.82$, $n_\mathrm{s} = 0.95$, and $h = 0.7$, consistent with the results from Planck Collaboration et al. (2015).

3.2   Semi-Analytic Model

In this section, we briefly summarize the details of our semi-analytic model for Pop III star formation, which is detailed further in Mebane et al. (2018). We initialize a set of halos in which stars will eventually form at $z = 50$ and evolved until $z = 6$. Halo masses are chosen to span the range of $10^6 M_\odot$ to $10^{13} M_\odot$ at $z = 6$[1]. The growth rate of these halos is calculated through abundance matching, where we assume that halos maintain their comoving number density throughout cosmic time. To do this calculation, we use mass functions found from fits to high redshift simulations of dark matter halo growth by Trac et al. (2015). We note that these assumptions only track the average growth of halos, and thus we do not include the

---

[1]We note that increasing the maximum halo mass has a trivial effect on our results as halos above this mass are very rare.

effects of mergers. This is consistent with Behroozi & Silk (2015), who find the majority of halo growth at these redshifts comes from smooth accretion of material from the intergalactic medium (IGM).

3.2.1 Pop III Star Formation

Once we have a collection of dark matter halos and their mass histories, we then begin to model their star formation. Because the first star-forming halos were very small and consisted only of pristine gas, Pop III stars were likely very massive and formed in isolation. As they formed and subsequently died, they released metals into their birth halos that would eventually allow for the formation of more traditional Pop II stars. Flexibly modeling this transition is a main goal of this model, as these Pop II halos will be much easier to observe than their Pop III counterparts.

The first step in our semi-analytic Pop III star formation model is to determine the minimum halo mass at which molecular hydrogen cooling becomes efficient enough to allow gas clouds to collapse and form stars. Before the first stars form, this is determined by the amount of H_2 that a halo can form. Tegmark et al. (1997) found the required fraction of H_2 in a halo at high redshift for cooling to be efficient is given by

$$f_{\text{crit, H}_2} \approx 1.6 \times 10^{-4} \left(\frac{1+z}{20} \right)^{-3/2} \left(1 + \frac{10 T_3^{7/2}}{60 + T_3^4} \right)^{-1} \exp\left(\frac{512\text{K}}{T} \right). \tag{3.1}$$

Here, T is the virial temperature of the halo and $T_3 = T/10^3\text{K}$. In such a halo, molecular hydrogen is formed through the process

$$H + e^- \rightarrow H^- + h\nu \tag{3.2}$$

$$H^- + H \rightarrow H_2 + e^-, \tag{3.3}$$

where free electrons catalyze the reaction. At these redshifts, cosmic microwave background (CMB) photons can easily destroy H^-, so a halo's H_2 abundance depends on the balance of

the formation and destruction rates of the intermediate ion. Tegmark et al. (1997) showed the fractional abundance to be a function of the halo's virial temperature (and hence mass)

$$f_{H_2} \approx 3.5 \times 10^{-4} \, T_3^{1.52}. \tag{3.4}$$

Once a halo's H_2 has exceeded the critical fraction shown in eq. 3.1, Pop III star formation can begin.

After the first halos begin star formation, however, the minimum halo mass to form Pop III stars is instead determined by the Lyman-Werner (LW) background. The LW band consists of photons in the energy range of 11.5 to 13.6 eV, which can photodissociate H_2 through the Solomon process (see Stecher & Williams, 1967). Once star formation begins, a large enough LW background is quickly built up to limit Pop III star formation to only halos massive enough to form enough molecular hydrogen to shield themselves from this background and allow cooling in their inner regions. Visbal et al. (2014) find this critical mass to be

$$M_{\min} = 2.5 \times 10^5 \, M_\odot \, \left(\frac{1+z}{26}\right)^{-1.5} \left(1 + 6.96 \, (4\pi J_{LW})^{0.47}\right). \tag{3.5}$$

We calculate the specific intensity of the LW background self-consistently from star formation in our model, and we require halos to exceed this critical mass before they can begin forming Pop III stars. We note that Pop III stars are expected to emit approximately an order of magnitude more total LW photons per baryon than Pop II stars (see Schaerer, 2002; Barkana & Loeb, 2005). Due to the increased UV photon yield, we might expect Pop III stars to have an early, noticeable effect on the cosmological 21-cm background through the Wouthuysen-Field effect (see section 3.3).

We note that there have been other studies that find the minimum mass required for Pop III star formation to instead be set by the relative streaming velocity between baryons and dark matter (e.g., Schauer et al., 2019). In general, we find that the minimum mass calculated from the Lyman-Werner background is always higher than the minimum mass from this streaming effect in our models so we do not include the effects of velocity offsets in our

study. In comparison to Schauer et al. (2019), our models (including the LW background) have minimum masses comparable to their "v3" simulation, which corresponds to offset velocities three standard deviations from the mean. Thus only in very rare volumes, or in the very earliest epoch of star formation (well before the absorption trough becomes significant) do streaming velocities significantly affect the minimum mass.

Once we determine the mass range of halos that can form Pop III stars, we then make the assumption that Pop III stars form in isolation in these halos due to their feedback and begin to add them to the halo. The mass of each star is individually drawn from the chosen IMF, and a new star can only form after the old star dies. If this star ends in a supernova that blows out most of the gas, we must wait for the halo to accrete enough new material for star formation to begin again. This typically causes a delay of a few million years between star formation episodes in models where supernovae are common.

We allow for a number of different initial mass functions (IMF) for Pop III stars. Because there have yet to be any observations of this mode of star formation, the IMF is largely unconstrained. McKee & Tan (2008) calculate the maximum mass of a Pop III star by stopping its growth once radiative feedback from LW photons, Lyman-α pressure on infalling material, and ionization becomes strong enough to limit accretion. They find this maximum mass to scale with the virial temperature of a halo as

$$M_{\mathrm{max}} \approx 145 M_\odot \left(\frac{25}{T_3} \right)^{0.24}. \tag{3.6}$$

In our fiducial models we test the case of three separate IMFs. The first, referred to as our "low" IMF in the rest of this paper, is a Salpeter-like IMF with a minimum mass of 20 $M_\odot$ and a maximum mass given by eq. 3.6. Our "mid" IMF assumes that, since Pop III stars grow in isolation, they will all be able to reach the maximum mass in eq. 3.6. Finally, our "high" IMF allows for the possibility of very massive Pop III stars which form from a Salpeter-like IMF spanning the range of 200 $M_\odot$ to 500 $M_\odot$.

Because the halos forming Pop III stars are so small (we find they can be as small as $10^5 M_\odot$ at the highest redshifts) feedback from Pop III star formation is very important. In particular, supernova feedback plays a vital role in regulating this mode of star formation, as the binding energies of these halos are of the order (Loeb & Furlanetto, 2013):

$$E_b \approx 2.53 \times 10^{50} \left(\frac{\Omega_{\mathrm{m}}}{\Omega_{\mathrm{m}}(z)} \right)^{1/3} \left(\frac{M}{10^6 M_\odot} \right)^{5/3} \left(\frac{1+z}{10} \right) h^{2/3} \mathrm{erg}. \tag{3.7}$$

Since a core-collapse supernova can release kinetic energy on the order of 10^{51} erg and a pair-instability supernova can exceed that by an order of magnitude (see Wise & Abel 2008 and Greif et al. 2010), a single supernova from a Pop III star can potentially unbind all of the gas in its birth halo (assuming ~ 1 to 10% of this kinetic energy is able to bind to the gas). This has implications for the transition to Pop II star formation as any metals released in a supernova can potentially be carried out of the halo. We use metal yields of Pop III stars from Heger & Woosley (2010) and Heger & Woosley (2002), which provide yields for core-collapse and pair-instability supernovae, respectively. In general, the specific yields of supernovae are not very important, as a single supernova provides more than enough carbon and oxygen to allow for efficient metal-line cooling assuming at least a few percent of the metals are retained by the halo.

Whenever a supernova occurs in a halo (typically ~ 5 Myr after the Pop III star forms), we assume 10% of the kinetic energy released binds to the gas in that halo. We then track this ejected gas's mass and metallicity, allowing it to reaccrete after a free-fall time. In the intervening time, pristine material from the IGM is still allowed to accrete onto the halo. This means that, in our model, multiple generations of Pop III stars are allowed to form before a halo becomes massive enough to retain the metals released in a supernova and transition to Pop II star formation. We find that halos typically form ~ 10 Pop III stars before becoming tightly enough bound to retain enough metals and transition. This typically occurs around the same time a halo reaches the atomic cooling threshold at a virial temperature of 10^4 K.

We note that our fiducial semi-analytic model differs slightly from similar models in that we allow allow multiple generations of Pop III stars to form in a single halo and these stars form in isolation. For example, Visbal et al. (2018) and Jaacks et al. (2018) only allow a single generation of Pop III stars to form in a halo before transitioning to metal enriched star formation. We investigate the differences between these two approaches as well as compare a run of our model with only one generation of Pop III star formation per halo in Mebane et al. (2018).

3.2.2 Pop II Star Formation

The formation of Pop II stars is also an important part of our model, as Pop II stars very quickly begin to dominate the LW background and set the minimum halo mass for Pop III star formation. We use the feedback-regulated models of Furlanetto et al. (2017) who test models where either energy or momentum is conserved in supernova winds. In these models, the star formation efficiency, f_*, is defined as the fraction of accreting material that will turn into stars and is written as

$$f_* \approx \frac{1}{1 + \eta\left(M_h, z\right)}, \tag{3.8}$$

where η, defined as $\dot{M}_{\mathrm{ej}} = \eta \dot{M}_*$, relates the star formation rate to the rate at which gas is ejected from the halo due to feedback. In the energy-regulated case, η is determined by balancing the rate at which kinetic energy is released into the halo by supernovae with the rate at which the halo gains binding energy from accretion. This can be written as

$$\eta_{\mathrm{E}} = 10\epsilon_{\mathrm{k}}\omega_{49}\left(\frac{10^{11.5}M_\odot}{M_h}\right)^{2/3}\left(\frac{9}{1+z}\right), \tag{3.9}$$

where ϵ_{k} is the fraction of a supernova's kinetic energy which is used to drive a wind, and ω_{49} is the amount of energy released in supernovae per unit mass of star formation in units of 10^{49} erg $M_\odot$. In our fiducial model, $\omega_{49} = 1$ and $\epsilon_{\mathrm{k}} = 0.1$. In the momentum-regulated

case we instead conserve momentum in this calculation and write η as

$$\eta_{\mathrm{p}} = \epsilon_{\mathrm{p}} \pi_{\mathrm{fid}} \left(\frac{10^{11.5} M_{\odot}}{M_h} \right)^{1/3} \left(\frac{9}{1+z} \right)^{1/2}. \tag{3.10}$$

Here, ϵ_{p} defines the fraction of the momentum released in a supernova that is used to drive winds in the halo and is taken to be 0.2 fiducially. π_{fid} parameterizes the momentum injection rate from stars formed from a given IMF and is of order unity for a Salpeter IMF (see Furlanetto et al. (2017) for a more detailed derivation of these quantities). These parameter choices match the observed luminosity functions at $z \gtrsim 6$ reasonably well but offer contrasting extrapolations to higher redshifts and smaller halo masses.

In general, the momentum-regulated case allows for more efficient star formation in low mass halos than the energy-regulated case, which yields a higher LW background. This cuts off Pop III star formation at a much earlier time, as the minimum mass rises very quickly.

The results of our semi-analytic model are summarized in Fig. 3.1, which shows the star formation rate density of Pop III stars for a variety of models.

3.3   The Global 21-cm Signal

The 21-cm differential brightness temperature can be written as (Furlanetto, 2006)

$$\delta T_b \simeq 27 x_{\mathrm{HI}} \left(1 + \delta \right) \left(\frac{\Omega_{\mathrm{b}} h^2}{0.023} \right) \left(\frac{0.15}{\Omega_{\mathrm{m}} h^2} \frac{1+z}{10} \right)^{1/2} \left(\frac{T_{\mathrm{S}} - T_{\mathrm{rad}}}{T_{\mathrm{S}}} \right) \ \mathrm{mK}, \tag{3.11}$$

where δ is the overdensity, x_{HI} is the fraction of neutral hydrogen in the universe, T_{rad} is the temperature of the radio background (typically the CMB temperature), and T_{S} is the spin temperature of neutral hydrogen,

$$T_{\mathrm{S}}^{-1} = \frac{T_{\mathrm{rad}}^{-1} + x_\alpha T_\alpha^{-1} + x_{\mathrm{c}} T_{\mathrm{K}}^{-1}}{1 + x_{\mathrm{c}} + x_\alpha}. \tag{3.12}$$

Here, x_{c} is the collisional coupling coefficient, T_α characterizes the strength of the Lyman-α background, and T_{K} is the kinetic temperature of the gas. x_α is the radiative coupling

coefficient quantifying the Wouthuysen-Field effect (Wouthuysen, 1952; Field, 1958) and is defined as (Chen & Miralda-Escudé, 2004; Hirata, 2006)

$$x_\alpha = 1.81 \times 10^{11}(1+z)^{-1}J_\alpha, \tag{3.13}$$

where J_α is the Lyα flux computed from the Pop III and Pop II sources in our semi-analytic model. We combine the semi-analytic model described above with the global 21-cm simulation code ARES, which computes the relevant radiation backgrounds and temperatures and is described in more detail in Mirocha (2014), to compute the effects of Pop III star formation on the global 21-cm background.

Recently Bowman et al. (2018) reported the first detection of a cosmological 21-cm global signal with the EDGES experiment. While this detection has yet to be confirmed by another experiment, it shows some features inconsistent with previous theoretical predictions. Specifically, it has an absorption feature centered around a frequency of ~ 78 MHz or $z \sim 18$. This is earlier than the predictions of most models which study star formation in *atomic* cooling halos (i.e., Mirocha et al., 2017), suggesting that an unknown source of star formation generated a Ly-α background at these early times. Also, the absorption feature appears to be much deeper than predicted at $\sim$500 mK, potentially implying that the gas had somehow cooled faster than expected for adiabatic expansion or the existence of another radio background (over and above the CMB) against which the 21-cm absorption occurs. We note that, due to the challenging nature of these observations, there are still concerns about the cosmic origin of this signal due to systematics and foreground contamination (e.g., Hills et al., 2018; Draine & Miralda-Escudé, 2018; Spinelli et al., 2019; Bradley et al., 2019; Sims & Pober, 2019).

The global 21-cm signal is determined by the factors $x_{\rm HI}$ – likely near unity throughout the era of Pop III star formation – and the temperature. The latter depends on: (1) the ultraviolet background (through x_α), and hence the star formation rate; (2) the X-ray background, which likely determines T_K because X-rays can propagate large distances through the IGM;

and (3) the radio background, if $T_{\rm rad}$ differs from the CMB. The first follows directly from the Pop III semi-analytic model described in §3.2, but the other factors require us to follow the growth of black holes in the early Universe. In the next section, we describe how we supplement our semi-analytic model to do that.

3.4   Emission From Black Holes

In our semi-analytic model, we self-consistently model the production and growth of black holes from Pop III stars as well as their X-ray and radio emission. Once the first Pop III star of the appropriate mass in a halo reaches the end of its life, we form a black hole that grows throughout the rest of the run of the model. This is where our choice of IMF has the most effect, as it is thought that a star with mass between $140\,M_\odot$ and $260\,M_\odot$ will end its life in a pair-instability supernova which will not leave behind a remnant. Similarly, a star with mass in the range $40\,M_\odot$ and $140\,M_\odot$ and above $260\,M_\odot$ will not result in a supernova but will instead collapse directly into a black hole, in which case we form a black hole with a mass equal to that of the star (i.e., Heger & Woosley, 2002, 2010).

The growth of a single black hole in a halo is governed by

$$\dot{M}_{\rm BH} = f_{\rm Edd} f_{\rm gas} \dot{M}_{\rm Edd} + \dot{M}_{\rm BH,\ new}, \tag{3.14}$$

where $\dot{M}_{\rm Edd}$ is the rate of Eddington-limited accretion, $\dot{M}_{\rm BH,\ new}$ is the rate at which new black holes are produced in the halo, and $f_{\rm Edd}$ is the fraction of the Eddington limit at which black holes are allowed to accrete (fiducially taken to be 0.1). Since we track the amount of gas that is available inside a halo due to accretion and feedback, we do not allow black holes to accrete if there is not sufficient gas in the halo. The factor $f_{\rm gas}$ is hence unity if the halo has a gas reservoir available and zero otherwise. Halos typically contain more than enough gas for accretion onto the central black hole, and it is only in the first few million years after a supernova that $f_{\rm gas} = 0$. Since halos in our fiducial model can form multiple
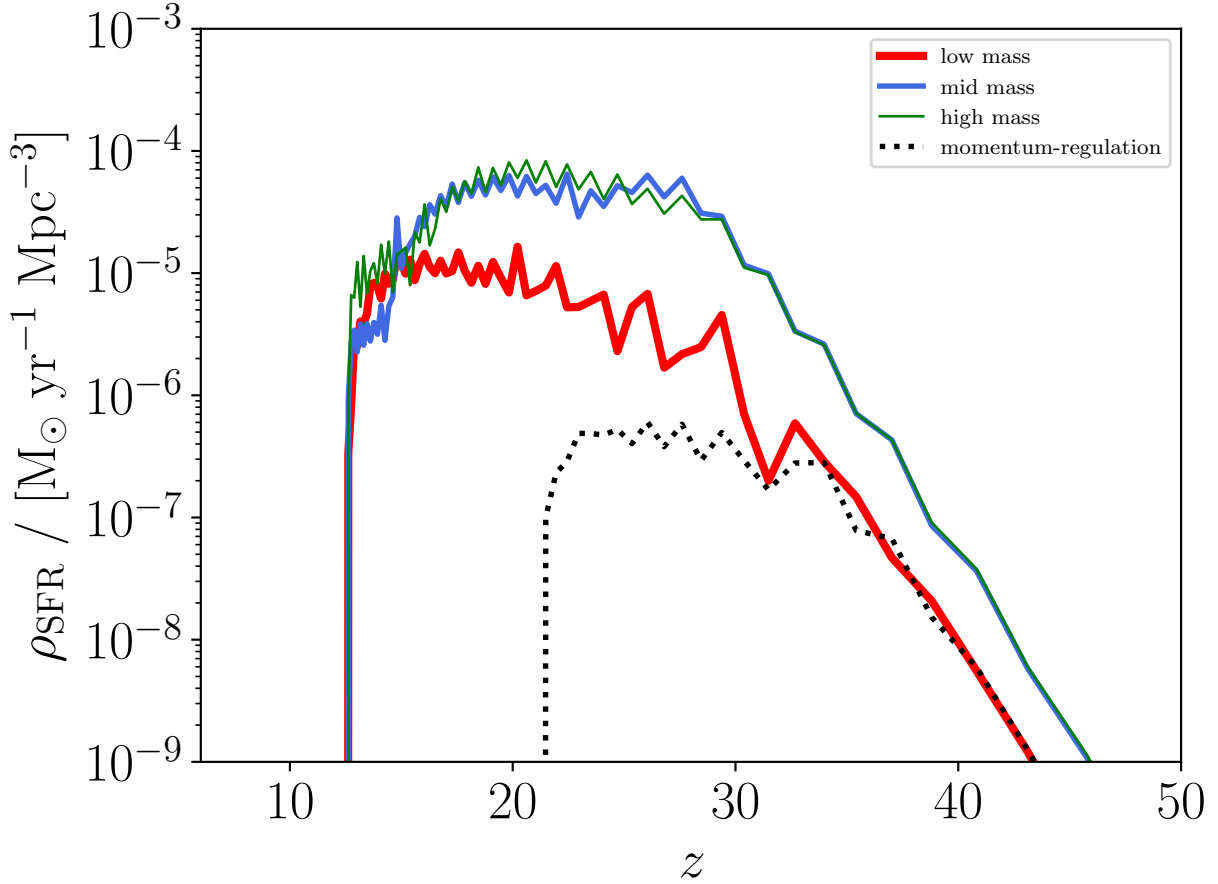
Figure 3.1: Star formation rate densities of Pop III stars in minihalos for the models used in this paper. The black dotted curve shows a model using momentum-regulated Pop II star formation, while the other curves assume energy-regulation. Since our momentum-regulated models produce a higher LW background, molecular hydrogen in minihalos is much more easily destroyed and Pop III star formation ends much earlier. The three curves with energy-regulated Pop II star formation compare our low-, mid-, and high-mass models for a Pop III IMF. Since the mid- and high-mass models typically produce stars around an order of magnitude more massive than the low-mass IMF, the differences in the star formation rate densities shown here can be attributed to the different stellar masses. While these models may have similar star formation rate densities, the details of the IMF are very important for determining the formation of black holes (see Fig. 3.2) which may cause a larger difference in the 21-cm signal.

generations of Pop III stars, we make the simple assumption that all new black holes will eventually merge with the central black hole in the halo, so anytime a new black hole is created its mass is added to that of the main black hole. Once a halo transitions to Pop II star formation, all future growth is from accretion rather than the production of new black holes. Note that we do ignore any new black holes that Pop II galaxies form; in the models we examine, the IGM is already heated significantly by this point, so such black holes do not affect our conclusions.

We show the resulting comoving black hole mass density, under several different assumptions in our model, in Fig. 3.2. In all cases, we assume that black holes accrete at 10% of the Eddington limit. In general, creation of new black holes is dominant over growth via accretion, especially during the early stages of growth when black holes are still small. We note that the specific parameters governing black hole growth in the early universe are not well known (i.e., our assumptions of $f_{\mathrm{Edd}} = 0.1$ and that all Pop III black holes in a halo will eventually merge), although our results are at least qualitatively the same for a large range of black hole growth assumptions.

If there is a significant population of accreting Pop III remnants at high redshift, they should emit in the X-ray as well as the radio. Both such backgrounds have strong implications for the 21-cm signal: an X-ray background will serve to heat the neutral hydrogen in the IGM[2], decreasing the depth of the absorption trough, but a radio background can increase the depth by raising the background radio temperature (Feng & Holder, 2018). Moreover, the onset of both backgrounds – which grow roughly exponentially in the early phases, as shown in Fig. 3.2 – will affect the timing of any 21-cm features. In the next two subsections we explore our models for these backgrounds.

---

[2] We note that a strong X-ray background can also produce an extra Lyman-α background from recombinations in the IGM. We ignore this effect, however, as Mirocha et al. (2018) find that this effect is only noticeable with X-ray backgrounds far greater than what is considered here. Moreover, if the X-ray background is high enough to substantially contribute to the Lyman-α background, the resulting heating of the IGM would be so great that the 21-cm absorption signal would be completely eliminated.
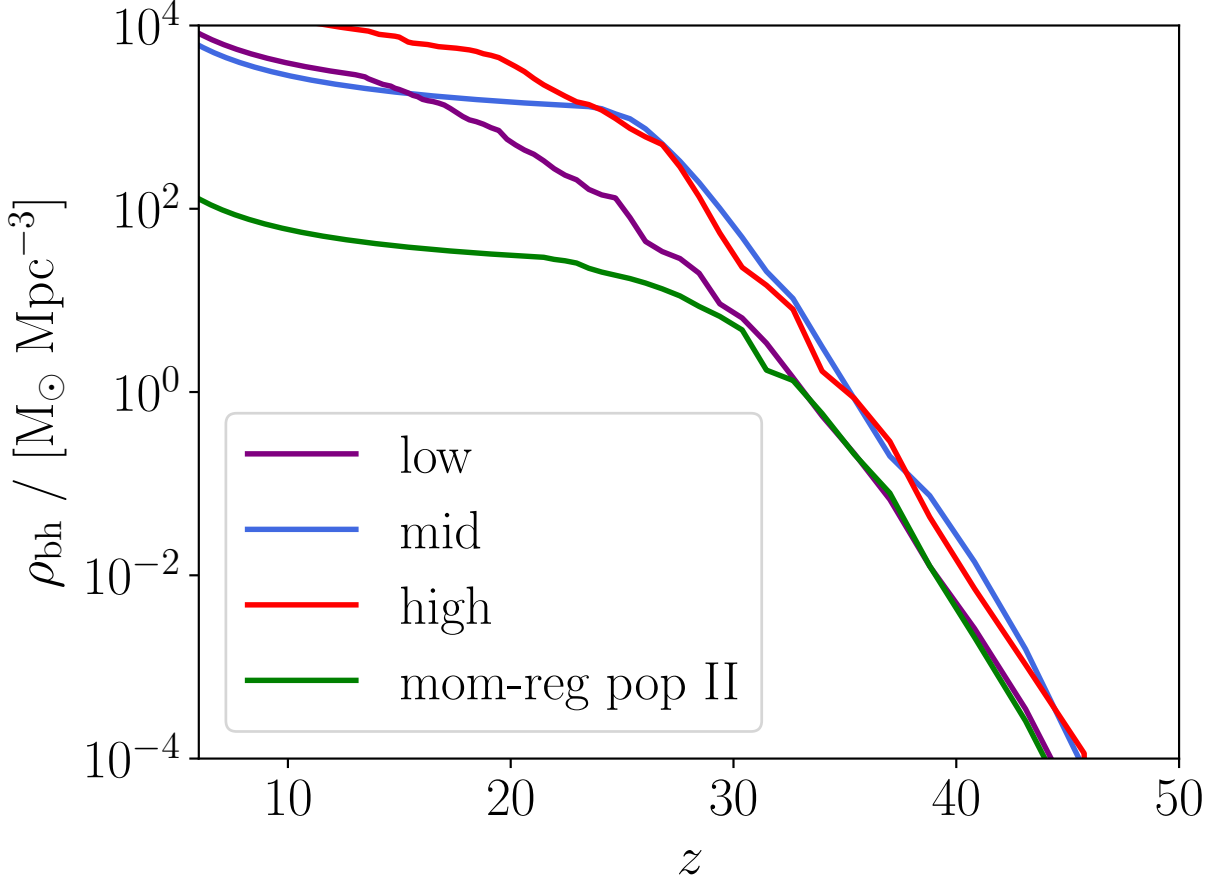
Figure 3.2: Black hole mass density with an accretion efficiency of 10%. The break at z~ 25 in the "mid" model is due to the slight redshift dependence on the maximum Pop III mass from McKee & Tan (2008). At this point, Pop III stars in new halos are massive enough to end in pair instability supernovae, so they do not leave behind a black hole, and any growth in the black hole mass density is due to accretion. Note that these densities are, at their maximum, at least an order of magnitude lower the mass density of black holes at lower redshifts which have been found to be $\sim 10^5$ M$_\odot$ Mpc^{-3}(Aller & Richstone, 2002).

3.4.1 X-ray Heating

To study this effect, we compute the X-ray background in ARES directly from the Pop III remnant black hole mass densities calculated in our semi-analytic model. In our model, we assume that individual accreting black holes emit X-rays with a multi-color disk spectrum (Mitsuda et al., 1984) with luminosity

$$L_{\mathrm{BH}} = 1.26 \times 10^{38} \, f_X \, \mathrm{erg \, s^{-1}} \left(\frac{M_{\mathrm{BH}}}{10 \mathrm{M_\odot}} \right) \left(\frac{f_{\mathrm{Edd}}}{0.1} \right) \left(\frac{f_{0.5-8}}{0.84} \right), \tag{3.15}$$

where $f_{0.5-8}$ is the fraction of the energy emitted in the 0.5 keV to 8 keV band for a 10 $\mathrm{M_\odot}$ black hole. Here f_X is an arbitrary scaling factor that allows us to vary the overall efficiency of X-ray production during accretion.

We note that a significant portion of the X-ray background could be suppressed if halos contain a large enough column density of neutral hydrogen and helium. Ewall-Wice et al. (2018) find that a column density of $\sim 10^{23}$ cm^{-2} is required to block X-ray emission from a halo. We find that halos in our semi-analytic models can only reach these column densities if they contain close to the cosmic baryon fraction of baryons and if all of these baryons can quickly cool onto the center of the halo. While gas can cool fairly easily onto the halo, it is difficult for haloes to keep enough gas in the halo without it being disrupted by Pop III supernovae. Nevertheless, we explore the effects of local absorption more thoroughly in section 3.5.2.

3.4.2 Excess Radio Background

We also include a calculation of the radio background produced by the accreting black holes in our semi-analytic model using the ARES code. The brightness temperature of this background at $\nu = 1420.41$ MHz for a given density of black holes is

$$T_{\mathrm{rad}}(z) = \frac{c^2 J_\nu(z, f_R)}{2 \nu^2 k_B}, \tag{3.16}$$

where $J_\nu(z, f_R)$ is the specific intensity of the radio background experienced by clouds of neutral hydrogen at redshift z. The specific mechanism for the production of this radio background from accreting block holes is not well understood, so we follow Ewall-Wice et al. (2018) who use empirical trends to calibrate this background (see, for example, Merloni et al. 2003 for a discussion of a "fundamental plane" of black hole X-ray and radio emission). They calculate $J_\nu(z, f_R)$ as

$$J_\nu(z, f_R) = \frac{c}{4\pi}(1+z)^3 \int_z^\infty \epsilon\left(\nu\frac{1+z'}{1+z}, z', f_R\right)\frac{dz'}{(1+z')H(z')},\qquad (3.17)$$

where $\nu = 1420.41$ MHz and ϵ is the emissivity of the radio background,

$$\epsilon(\nu, z, f_R) \approx 1.2\times 10^{22}\left(\frac{f_R}{1}\right)\left(\frac{\rho_{\rm bh}}{10^4 h^2 M_\odot {\rm Mpc}^{-3}}\right)\left(\frac{\nu}{1.4\ {\rm GHz}}\right)^{-0.6}\ {\rm W\ Hz}^{-1}h^3{\rm Mpc}^{-3}.\ (3.18)$$

Here $\rho_{\rm bh}$ is the black hole mass density computed from our semi-analytic model (see Fig. 3.2).[3] We also introduce a new dimensionless parameter, f_R, which boosts the emissivity of radio emission from accreting black holes relative to the empirical calibration. We vary this normalization parameter to fix the excess radio background generated from the black holes. We note Mirocha & Furlanetto (2019) require $f_R \sim 100$ to match the amplitude of the EDGES signal, although they do not include the effects of Pop III star formation.

Fig. 3.3 shows the brightness temperature of this radio background for a number of scenarios generated using our model with $f_R = 50$.[4] Assuming accreting Pop III remnant black holes are able to emit in the radio in this way, we find a temperature that can be as much as ~ 100 times the CMB temperature at the relevant redshifts. Since the depth of the primary absorption feature in the global 21-cm signal measures the difference between the spin temperature of the neutral hydrogen gas and the brightness temperature of the dominant

---

[3]Note that we have simplified eq. 3.18 relative to the treatment of Ewall-Wice et al. (2018), as details such as the duty cycle of accretion, $f_{\rm duty}$, are degenerate with our semi-analytic model (which natively tracks when gas is available in a halo for accretion). Similarly, we have omitted factors relating to the fraction of radio loud accreting black holes and absorbed this into f_R.

[4]We show results for the apparently extreme choice of $f_R = 50$ because we will find later that this is roughly the value required to reproduce the depth of the EDGES signal.

radio background, a background such as this would greatly enhance the strength of such a feature.

Models which end Pop III star formation earlier, such as our momentum-regulated Pop II models, tend to have a much lower radio background temperature that eventually begins to fall like the temperature of the CMB due to redshifting. This is due to our assumption that all Pop III black holes will eventually merge combined with the mass dependence of Eddington-limited accretion. Since halos spend a significantly shorter time in the Pop III phase in these models, their black holes do not reach a high mass early on due to mergers. This causes them to grow very slowly through smooth accretion, as they do not get the same "bump" in mass that Pop III black holes would get if their halos formed many more generation of Pop III stars (as in our energy-regulated models).

3.5   Results

We are now ready to examine our Pop III model's implications for the global 21-cm background. We will consider two important aspects of the signal: its *timing*, which includes both the point at which the absorption trough reaches its minimum but also the shape of the signal around it, and its *depth*. The former is important for any model of the early Universe, because it has direct implications for measuring the earliest generations of star and black hole formation. The depth is particular interesting in the context of the EDGES measurement: specifically, we are interested in whether Pop III models can provide a self-consistent explanation for the anomalous depth of the EDGES absorption trough.

Even within the context of our semi-analytic model, the uncertainties in Pop III star formation are large enough that we cannot examine every possible scenario in detail. We therefore focus on two qualitative questions, rather than attempting to provide quantitative constraints from the EDGES claim. First, is it 'natural' for PopIII models to produce an
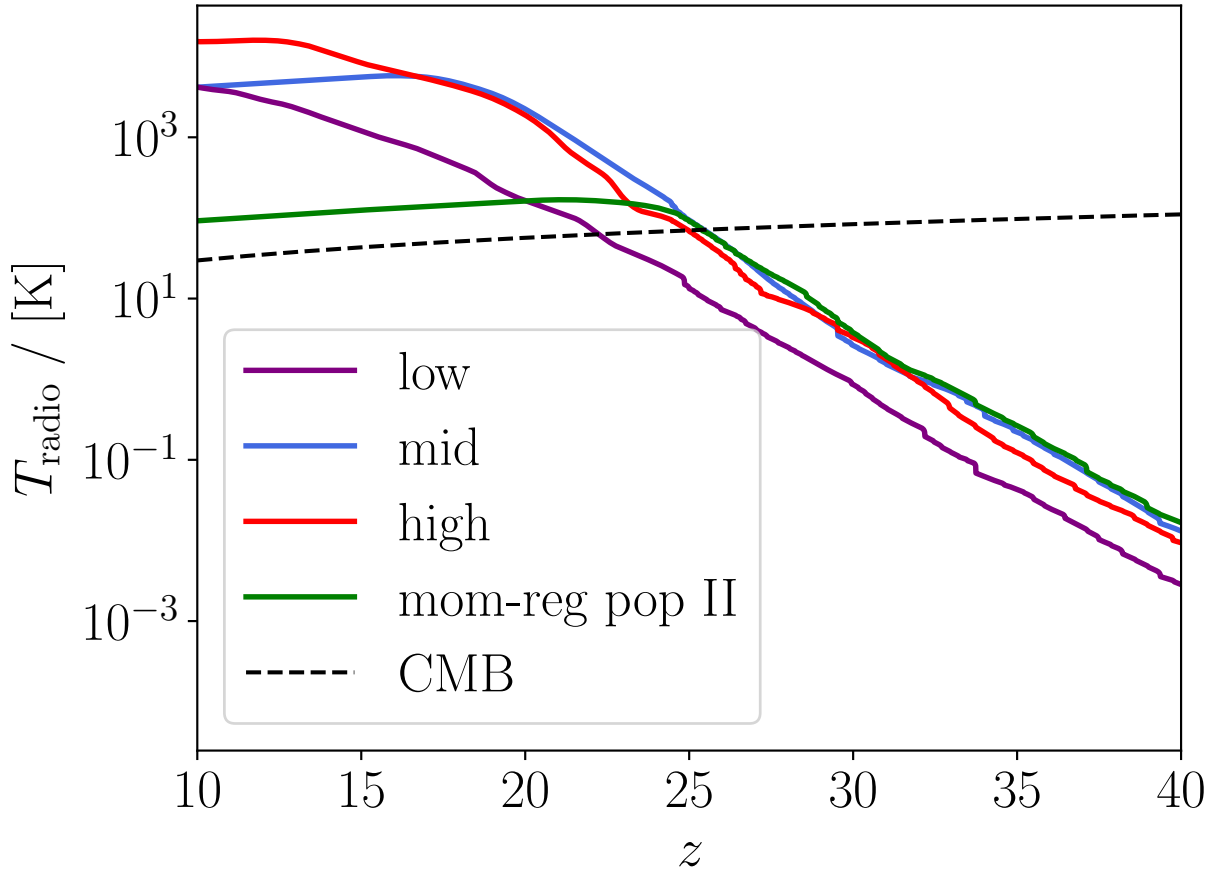
Figure 3.3: Temperature of the excess radio background computed from the black hole mass densities in our semi analytic model. For this calculation we have set $f_R = 50$. The dashed black curve shows the temperature of the CMB. All models assume energy-regulated Pop II star formation besides the green curve, which assumes momentum-regulation. If Pop III remnant black holes are able to efficiently accrete and emit a radio background this strongly, the resulting brightness temperature of the dominant radio background can be much higher than that of the CMB.

early absorption trough, given that PopII-only models do not predict such early features (Mirocha & Furlanetto 2019)? That is, do a broad range of parameters and assumptions produce such a trough? Second, is it *possible* for "fine-tuning" to produce surprising results – in particular, the large amplitude of the EDGES claimed detection?

3.5.1 The Timing of the Global 21-cm Signal

In this section we investigate the timing of the absorption feature of the global 21-cm signal. In general, we expect the addition of Pop III star formation to push the signal to higher redshifts. If early Pop III star formation is able to build up a high enough Lyα background, we should expect Wouthuysen-Field coupling to occur earlier and drive the spin temperature of the gas toward the kinetic temperature at earlier times. This will cause the signal to move into absorption earlier, potentially to $z \sim 18$ where the EDGES signal reaches its minimum.

Figures 3.4 and 3.5 show examples of the global signal computed from the energy-regulated models with a low-mass Pop III IMF described in section 3.2 with the EDGES signal over-plotted. In these figures, we primarily vary the parameters controlling the X-ray and radio backgrounds, f_R and f_X. We hold all other parameters constant for simplicity, taking $f_{\mathrm{Edd}} = 0.1$, assuming no absorption of X-rays due to a local column density of neutral gas, and our "low" mass Pop III IMF. We do vary the Pop II prescriptions: the solid lines assume energy regulation, while the dot-dashed curves assume momentum regulation. We note that our models with energy-regulated Pop II star formation provide the best fits to the EDGES signal, as the momentum-regulated models do not have a large effect on the global signal unless their Pop III emission is tuned to be very high. This is because the star formation efficiency in low mass Pop II halos in the momentum-regulated case is much higher, causing a high LW background which shuts off Pop III star formation sooner.

Regardless of the depth of the signal, we find that, over a broad range of parameter space

and model assumptions, an era of Pop III star formation can generate a large enough UV background to trigger Wouthuysen-Field coupling and hence a 21-cm absorption trough. In this context, the timing of the EDGES trough *does* occur naturally for many Pop III star formation scenarios, in contrast to scenarios that assume star formation in $z > 15$ galaxies follows the same trends as in populations at much lower redshifts (Mirocha & Furlanetto, 2019). As a result, if increasingly efficient Pop II star formation can be ruled out by future galaxy surveys, the global 21-cm signal reported by EDGES would provide strong evidence of Pop III star formation in the early Universe. We do note, however, that regardless of our parameter choices our fiducial model does not match the *shape* of the signal. Specifically, the EDGES team found an absorption trough with a flat bottom and a sharp rise out of absorption. Our models have sharp declines at the onset of absorption but only gradually recover, as also found by Mirocha & Furlanetto (2019). This gradual rise is a natural consequence of the pace of structure formation and the physics of the 21-cm line. Structure formation proceeds exponentially at these times, but the Wouthuysen-Field effect is essentially a threshold process, so that the spin temperature approaches the kinetic temperature very rapidly once $x_\alpha > 1$. However, X-ray heating is a continuous process, so that the recovery is significantly slower (see also Mirocha et al. 2018). Thus, if the EDGES result is confirmed, it will require rapid time evolution in the parameters of the luminous sources. Section 3.5.3 describes one way in which this might happen – in that scenario, features in the stellar mass-remnant black hole mass relation induce a rapid change in black hole formation.

3.5.2 The Depth of the Global 21-cm Signal

In addition to the timing, we are also concerned with the depth of the absorption trough, particularly because of the extreme amplitude measured by EDGES. One way to increase the amplitude is to allow for gas in the IGM to cool faster than expected for an adiabatically expanding universe. A possible mechanism for this to occur is if hydrogen atoms can interact

with dark matter to some degree (e.g., Barkana, 2018). Regardless of the specific mechanism, one can fine tune this phenomenon to achieve the required depth of the EDGES signal after the proper timing has been attained (see, for example, the parameterized approach to cooling in Mirocha & Furlanetto, 2019). In order to match both the timing and depth of the EDGES signal *self-consistently* with Pop III stars, however, we must look at the specific properties of X-ray and radio emission from Pop III remnants in our model.

As discussed in section 3.4.2, accreting Pop III remnant black holes could produce a high enough radio background to dominate over the CMB and increase the reference radio brightness temperature in the global 21-cm signal by factors of up to ~ 100. Fig. 3.4 shows the effects of this background for various values of f_R while holding the boost to X-ray emission constant at $f_X = 1$. In these models, the best fit to the EDGES signal occurs around $f_R \sim 50$, which reproduces both the strength and timing of the signal but does not match the shape. In particular, note that the 21-cm signal remains in absorption throughout reionization. As shown in Fig. 3.3, models with large f_R increase the radio background to $T_R \gtrsim 1000$ K. Seeing the 21-cm signal in emission would require gas heating above this value, which is only possible when f_X is also very large.

These same accreting black holes should also produce X-rays, however, which will heat the surrounding gas and weaken the absorption feature of the signal. This is shown in Fig. 3.5, where we have set our radio boost parameter to it's maximal value of $f_R = 50$ to best see the effects of X-ray heating. In general, allowing X-ray emission at high levels can significantly lessen the strength of the signal, causing the absorption feature to completely disappear in the most extreme cases. If Pop III star formation were found to be the cause of the EDGES signal, we would need a way to allow accreting Pop III remnant black holes to emit efficiently in the radio but not in the X-ray.

This idea is shown in Fig. 3.6, which displays the peak amplitude of the absorption trough from a grid of 225 models varying f_R and f_X from 1 to 100. In general, we find that we
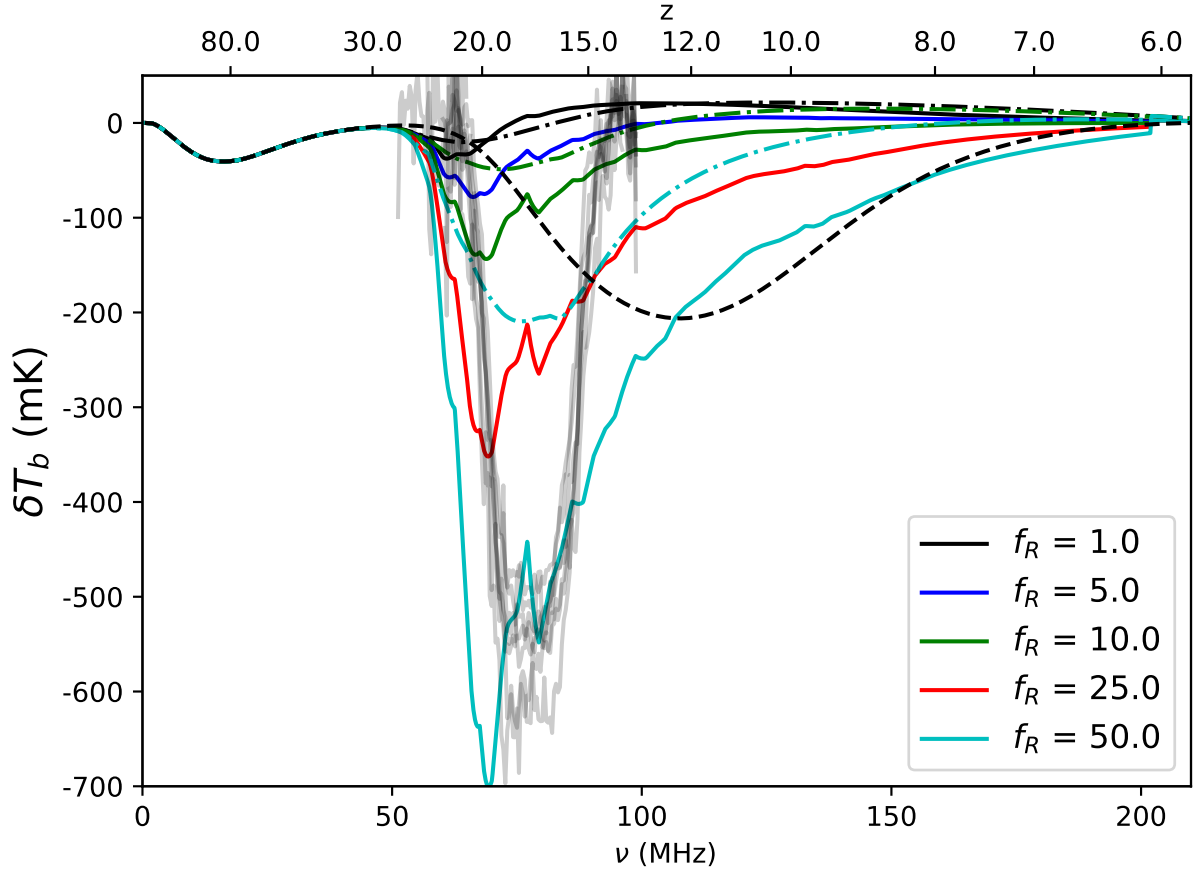
Figure 3.4: Effects of f_R on the global signal with our low mass Pop III IMF and energy-regulated Pop II star formation. The reported EDGES signal fits are overplotted in grey. All models provide a reasonably good fit to the timing of the signal, and the depth of the signal is best fit by boosting the radio emission by a factor of ~ 50. In this model, $f_X = 1$, and there is no excess cooling of the IGM. The dashed line shows a model without Pop III for comparison, and the dashed-dotted lines show our results with momentum-regulated Pop II star formation. In general, it is much harder for us to achieve the large depths of the EDGES signal in these momentun-regulated models.
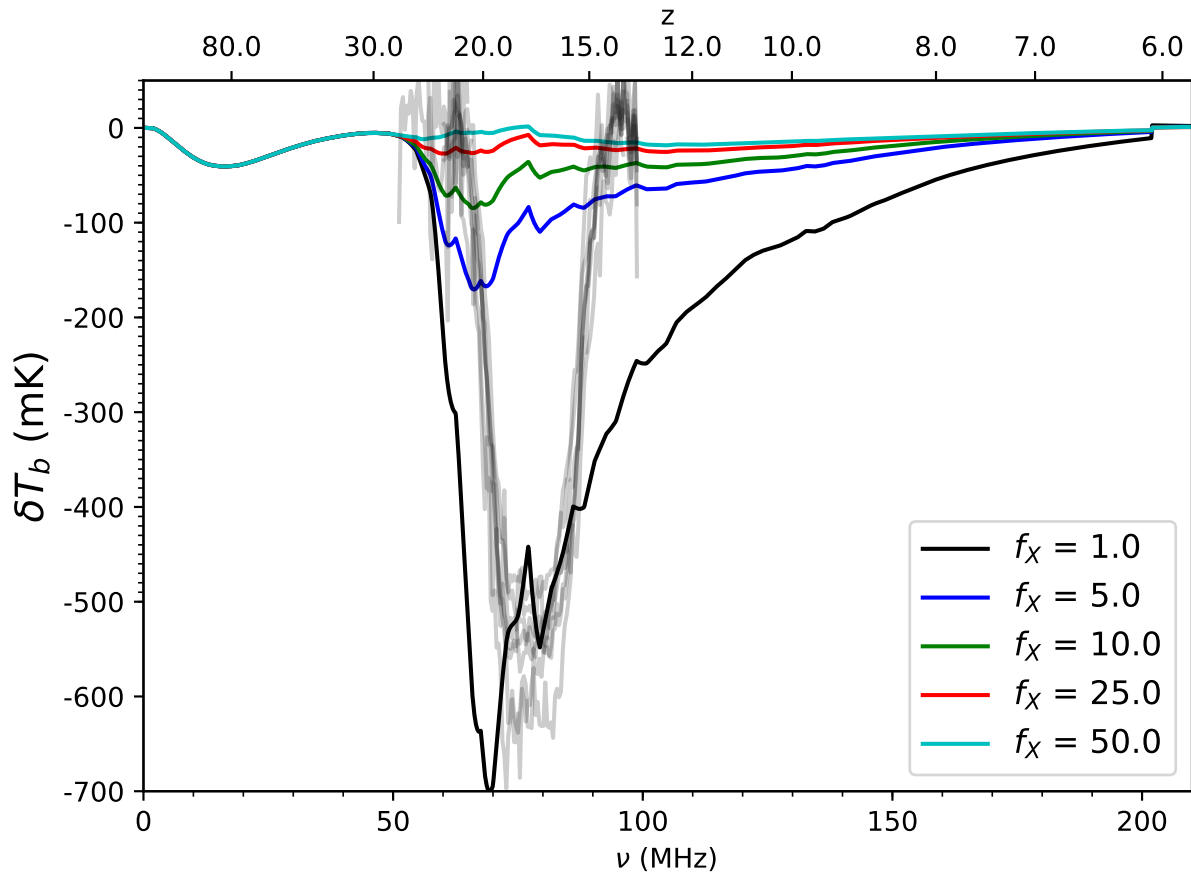
Figure 3.5: Effects of f_X on the global signal with our low mass Pop III IMF. Here we have set $f_R = 50$ to better show the effects of an increasingly strong X-ray background. We do not include a neutral hydrogen column density in this case. In general, stronger X-ray backgrounds will heat the IGM, lessening the depth of the absorption signal.
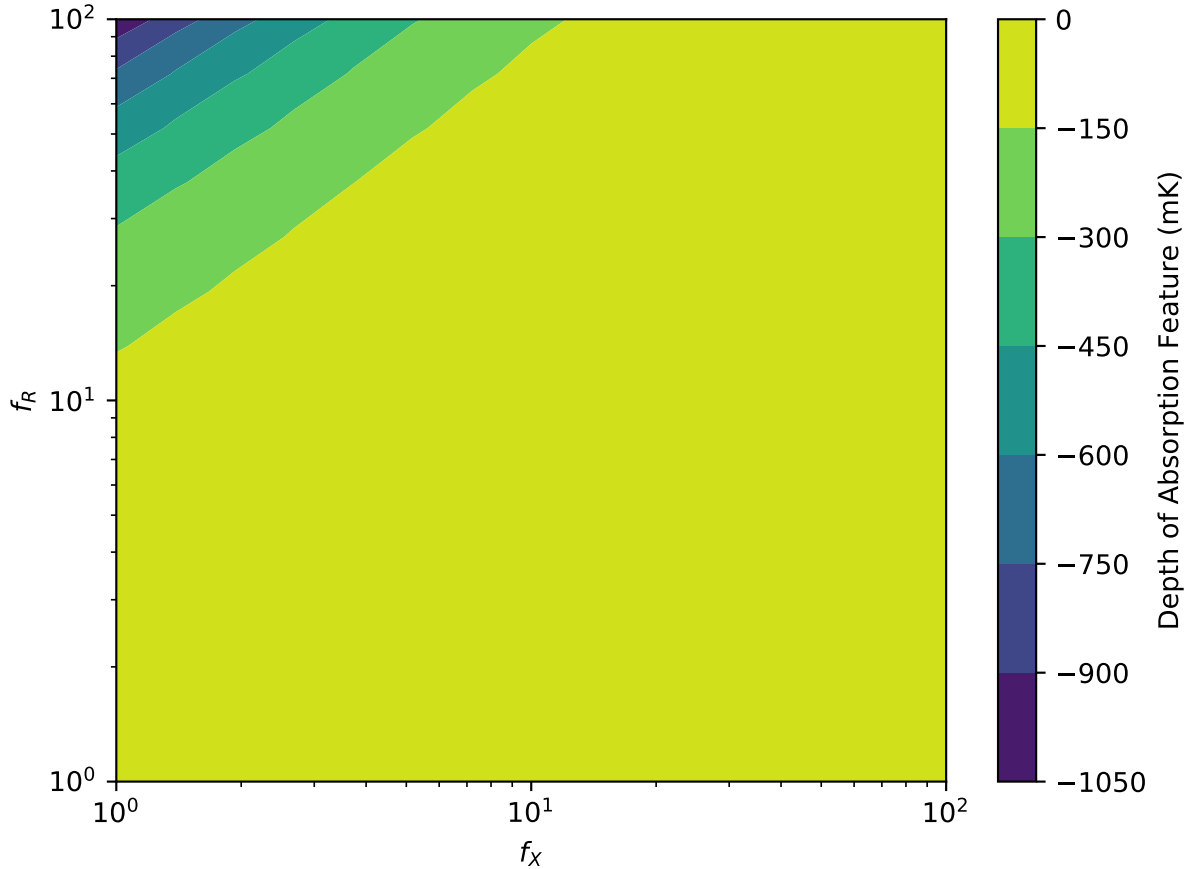
Figure 3.6: Grid of models with varying values of f_X and f_R. Depths similar to those of the edges signal (~ -500 mK) can only occur in our models when f_R is high and f_X is low.

can only reproduce the depth of the EDGES signal in cases with high f_R and low f_X. As discussed in section 3.4.1, this could be possible if halos have very strong radio emission but also have a high enough column density of neutral hydrogen and helium to block X-ray emission from the accreting black holes, although such high column densities are difficult to obtain in Pop III halos in our semi-analytic model. However, they are easier to imagine in larger halos that have transitioned to Pop II star formation, and these halos would still contain the Pop III remnant black holes formed previously.

In order to test the effect of column densities of neutral gas on X-ray emission, we apply

various column densities to our Pop III halos in ARES ranging from $N = 10^{20}$ cm^{-2} to $N = 10^{23}$ cm^{-2} in Fig. 3.7. At the lower column densities there is not much of a difference in the global signal, as lower energy X-rays are able to escape the halo and heat the IGM effectively. As we progress to higher column densities, only the higher energy X-rays can escape the halo and are unable to efficiently heat the IGM. In these cases we have set $f_R = 10$ in order to better match the depth of the EDGES signal. This is due to the decreased effect of X-ray heating from neutral gas requiring less radio emission to produce a deep signal. Similar to Ewall-Wice et al. (2018), we find that a column density of $N \sim 10^{23}$ cm^{-2} is required to fully block this emission and stop X-ray heating of the IGM. As we have mentioned above, however, such high column densities require that Pop III haloes retain all of their gas, which is not likely according to most feedback prescriptions.

3.5.3 Parameter Dependence

Most of our models shown so far used our energy-regulated Pop II star formation models which have less efficient Pop II star formation than the momentum-regulated models. We find that, in general, the momentum regulated models are able to reproduce the timing of the EDGES signal in a similar fashion, but we must increase f_R to much higher values while still keeping f_X low in order to reproduce the depth. This is simply due to the decreased mass density of black holes seen in the momentum regulated models (Fig. 3.2), as the Lyman-Werner background is much higher causing Pop III star formation to end earlier (see Fig. 3.1). This effect is shown in Fig. 3.4, where we have plotted example global signals varying f_R.

We note that our assumption of multiple generations of Pop III star formation in the same halo has large consequences for the effect of this mode of star formation on the 21-cm background. In Mebane et al. (2018) we find that only allowing a single Pop III star to form in a halo will lower the maximum star formation rate density of the Pop III phase by at least an order of magnitude to similar levels as our momentum regulated models. Thus, in
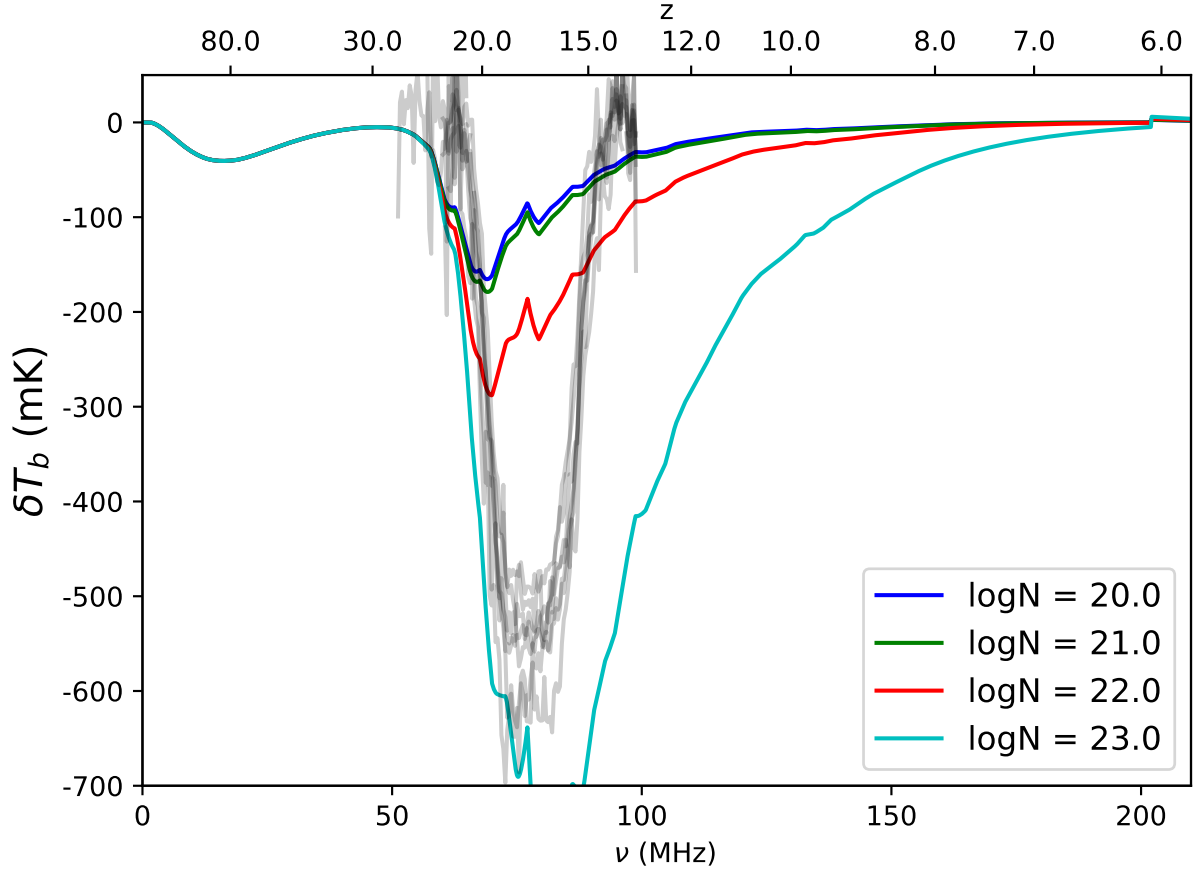
Figure 3.7: Column density effects on the global signal. At lower column densities, low energy X-rays can easily escape the halo and efficiently heat the surrounding IGM. As the column density gets higher, however, these X-rays are blocked and X-ray heating of the IGM becomes inefficient. This causes a significantly deeper absorption feature that takes a much longer time to rise out of its minimum. Here we have set $f_X = 1$ and $f_R = 10$ to better fit the EDGES signal due to the lessened effect of X-ray emission.

these models, it is much more difficult to attain the required depth to match the EDGES signal. Similar models which form a large mass of Pop III stars but in a single generation (e.g., Visbal et al., 2018; Jaacks et al., 2018) should, in principle, still be able to attain this depth with similar assumptions for X-ray and radio emission as their Pop III star formation rate densities are comparable to those of our fiducial models.

We also consider the effects of our choice of IMF for Pop III star formation. All previous plots have used our fiducial, low-mass "low" IMF, but we show the effects of the "mid" and "high" IMFs (described in section 3.2) in Fig. 3.8. Generally speaking, the higher mass IMFs which produce larger black hole mass densities cause a stronger absorption feature in the global signal. For example, matching EDGES with the low mass IMF requires $f_R \sim 50$, while the mid and high mass IMFs require only $f_R \sim 15$. This is simply because larger-mass black holes can grow faster and hence produce more emission.

This is not universally true, however, as IMFs that produce stars in the mass range of $140 M_\odot$ to $260 M_\odot$ are thought to end their lives in a pair-instability supernova that will not leave behind a remnant. One potentially interesting difference between our "mid" and "high" IMF cases is that, while the depth of both signals is roughly the same, the "mid" IMF case has a sharper rise out of the absorption feature. This is due to the redshift and halo mass dependence of the maximum Pop III mass calculated by McKee & Tan (2008). This IMF model assumes that *all* Pop III stars form at this maximum mass which, when combined with our self-consistently computed minimum halo mass for Pop III star formation, implies that, after a certain redshift (depending on the model), every new Pop III star forms in the range for pair instability supernovae. This can be seen in Fig. 3.2 where the "mid" case plateaus after $z \sim 30$. Since all new stars at this point will end in a pair instability supernova, any growth in the black hole mass density after this point is from accretion of new material rather than the creation of new black holes. As a consequence, Fig. 3.3 shows that past this point the radio background temperature begins to decline at $z \sim 20$ while the

temperature continues to rise in the other scenarios. This decline causes the difference in temperatures between the spin temperature of the gas and the radio background to decrease, allowing for the signal to rise more quickly out of absorption. The "high" IMF case also has a much quicker rise out of absorption than our fiducial "low" case, although to a lesser extent than the "mid" model. Again, the reason for this can be seen in Fig. 3.3 where the radio background temperature for this model has begun to level out. While our choice of IMF does not strongly effect the *timing* of the signal, it does indicate that the mass of individual Pop III stars could have an effect on the *shape*.

3.6 Conclusions

We have presented a model to test the effects of Pop III stars and their remnants on the global 21-cm signal. By combining a semi-analytic model for Pop III star formation (Mebane et al., 2018) with a global 21-cm simulation code (Mirocha, 2014), we have found that Pop III stars can have a large effect on this signal if these stars (and their remnants) are allowed to form and emit efficiently. By altering the Pop II and Pop III star formation prescription as well as the properties of radio and x-ray emission from accreting Pop III remnants, we are able to drastically alter the shape and depth of the signal.

Specifically, we find:

1. Our Pop III models with energy-regulated Pop II star formation generate a high enough Lyman-α background at the proper time to produce an absorption feature at around the right time to be consistent with the EDGES signal.

2. Allowing for a radio background from Pop III remnants can significantly increase the strength of the global 21-cm signal. Similarly, an X-ray background from Pop III remnants can significantly heat the IGM and decrease the strength of the signal. Thus
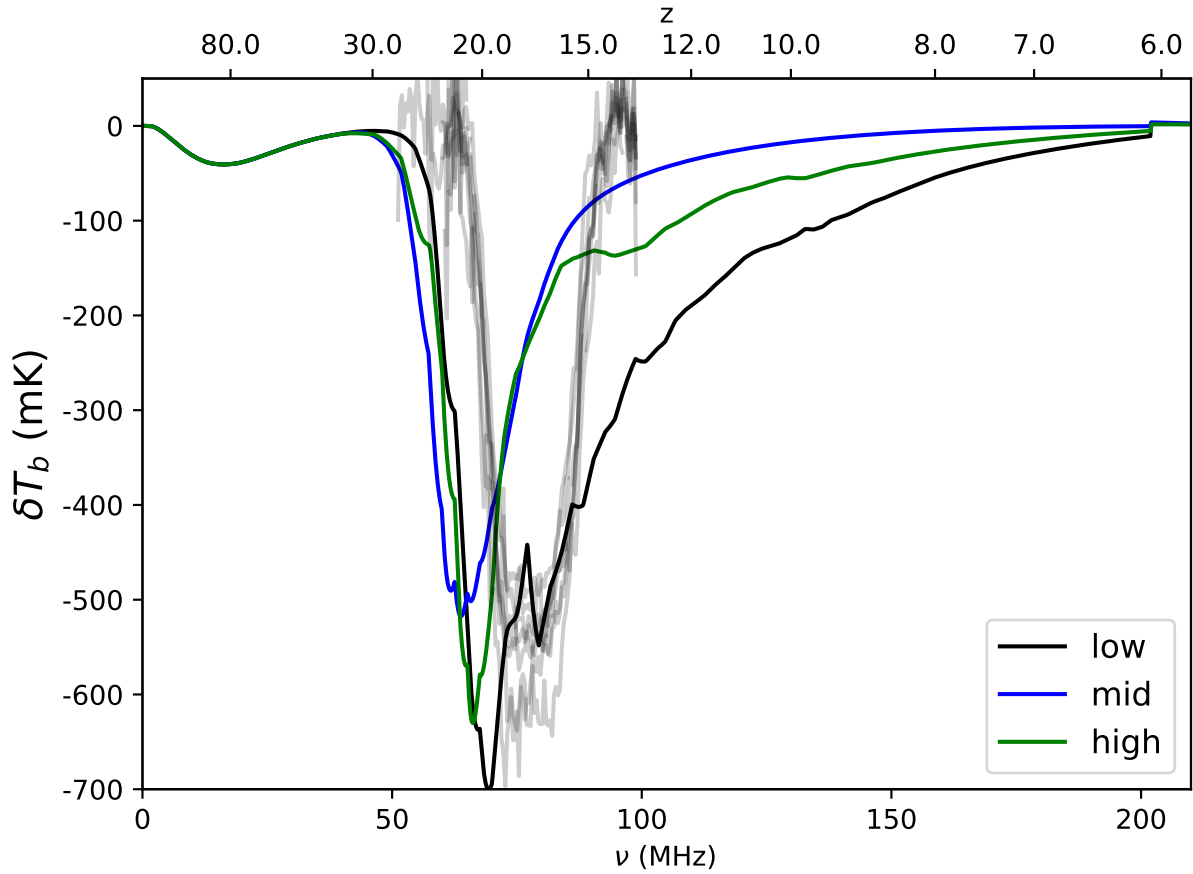
Figure 3.8: Global signals for varying Pop III IMFs. We have set $f_X = 1$ in all cases and have tuned f_R such that each model provides a rough fit to the depth of the EDGES signal. For the low mass case, as discussed in section 3.5.2, $f_R = 50$. In the mid and high mass cases we have set $f_R = 15$.

reproducing the depth of the EDGES signal requires Pop III black hole remnants to emit far more efficiently in the radio than in the X-ray, relative to local black holes.

3. Our choice of Pop III IMF can alter the shape of the signal without strongly affecting the timing or depth. In particular, our "mid" IMF model which forms stars from a sharply peaked IMF around $140 \, M_\odot$ is able to produce the sharpest signal.

We also compare our results to the recent detection from the EDGES experiment. In general, we find that a broad subset of our models for Pop III star formation are able to match the timing of the EDGES signal quite well, regardless of our choice of IMF and star formation prescription. Since the timing of the signal is mostly dependent on star formation at higher redshifts, the most important aspect our models in this regard is the timing of the formation of the very first Pop III stars. This generally happens before feedback specific to the IMF or Pop II star formation prescription has a large effect, so the most important factors are the physics of molecular hydrogen formation and cooling that sets the timing and halo mass range of the first Pop III stars. Altering other parameters such as the efficiency of accretion on Pop III black holes, the masses of Pop III stars, or the number of generations of Pop III star formation can vastly affect the shape and depth of the signal without altering the timing. Models including both a self-consistent radio and X-ray background can reproduce the depth of the EDGES signal only if f_R is much greater than f_X. One potential way to explain this is if Pop III halos have a high enough column density of neutral gas to block much of the X-ray emission from accreting black holes. This explanation is hard to motivate with our models, however, as we find that Pop III halos are constantly blowing out much of their gas, so that the local column density of neutral hydrogen is likely to be quite small.

While all of the Pop III models presented here produce a signal that agrees with the timing of the EDGES detection, it is also possible to produce a different timing by altering some of the parameters governing this mode of star formation. For example, we could produce a much later trough if we drastically reduce the efficiency of Pop III star formation. This

could be the case if only one generation of Pop III stars is allowed to form per halo or if the delay between generations of star formation is much larger due to our assumptions regarding accretion after a supernova clears the gas out of a halo. The likelihood of these scenarios is discussed in more detail in Mebane et al. (2018).

CHAPTER 4

The Effects of Population III Star Formation on the Cosmic 21-cm Power Spectrum

4.1 Introduction

The first stars in the Universe have never been observed, though their formation played an integral role in early galaxy formation and evolution. These stars likely formed in pristine minihalos cooled by molecular hydrogen, and, because of this, they were likely much more massive than stars forming today (Bromm et al., 1999; Abel et al., 2002; Bromm, 2013). Because of the small size and binding energy of their birth halos, these stars likely formed in very small numbers due to the disruptive nature of their feedback (Machacek et al., 2001; Wise & Abel, 2007; O'Shea & Norman, 2008; Shapiro et al., 2004; Visbal et al., 2018).

The actual first generations of metal-free stars are known as Population III (Pop III) stars, and there are many uncertainties in models studying Pop III star formation since we have yet to directly observe a Pop III halo. These unknowns include, for example, the initial mass function, the star formation efficency, and the transition to metal-enriched star formation. Many studies including analytic models (e.g., McKee & Tan 2008; Kulkarni et al. 2013), numerical simulations (e.g., Machacek et al. 2001; Wise & Abel 2007; O'Shea & Norman 2008; Xu et al. 2016; Stacy et al. 2012; Hirano et al. 2015; Maio et al. 2010; Sarmento et al. 2018), or semi-analytic models (e.g., Trenti et al. 2009; Crosby et al. 2013a; Jaacks et al.

2018; Visbal et al. 2018; Mebane et al. 2018) probe large ranges of parameter space due to these uncertainties. Regardless of the model, though, the extremely low star formation efficiency of Pop III stars in minihalos means it is unlikely we will directly observe them (Schauer et al. 2020 find that we would need a ~ 100 m telescope in space).

If we cannot directly observe these stars, perhaps we can probe them indirectly through measurements of the cosmological 21-cm background. This background is caused by the 21-cm "spin-flip" transition of neutral hydrogen, and we can learn much about star formation before reionization by studying its properties. The main features of this signal are set by the UV and X-ray backgrounds from star formation in the early Universe. The signal is observed as the difference between the spin temperature of neutral hydrogen in the intergalactic medium (IGM) and the temperature of the cosmic microwave background (CMB). At early times, a Lyman-α background will cause the signal to go into absorption. X-rays from the remnants of early star formation will then heat the gas in the IGM, potentially raising the spin temperature into emission. Finally, reionization from star formation will ionize the neutral hydrogen in the IGM, causing the signal to vanish (Furlanetto, 2006; Pritchard & Loeb, 2008). So far there has only been one claimed detection of the 21-cm global signal by the EDGES experiement (Bowman et al., 2018), although there are some claims that the absorption signal observed here is an artifact of instrumental effects (e.g., Hills et al., 2018; Bradley et al., 2019; Sims & Pober, 2020; Tauscher et al., 2020).

In Mebane et al. (2020) we studied the effects of Pop III star formation on the global 21-cm signal. We also included the effects of a radio background from accreting Pop III remnants which raised the radio background temperature above that of the CMB and helped us to better match the observations from Bowman et al. (2018). In general, we found that the specific details of radio and X-ray emission from early sources can have a large effect on the depth of the global signal. If accreting Pop III remnants are able to efficiently emit in the radio, they can cause a much deeper absorption feature by raising the background radio

temperature typically thought to be set by the CMB. We also found that Lyα emission from the first stars can hasten the onset of this feature to $z \sim 18$, consistent with the EDGES signal. By altering the IMF of Pop III star formation, we were able to change the shape of the signal without significantly affecting its depth or timing.

In this paper, we extend the analysis from our previous results to include another important aspect of the 21-cm signal, its spatial structure. We accomplish this by combining a semi-analytic model for Pop III star formation with the 21-cm simulation code 21CMFAST (Mesinger et al., 2011). We are interested in modeling the effect this mode of star formation has on the 21-cm background to see if there is any unique signature in the 21-cm power spectrum that would point to their existence and help us constrain the large parameter space in Pop III models. Since the power spectrum allows us to probe the spatial variations in this signal, there is potentially much more information than in the global signals studied in Mebane et al. (2020). We will examine how the distinct timing of Pop III star formation affects the 21-cm power spectrum, and we ask whether they imprint any unique signatures in the power spectrum.

We present the details of our semi-analytic model in section 4.2, and we describe our version of 21CMFAST in section 4.3. We present our results in section 4.4 and conclude in section 4.5.

In this paper, we assume a flat, ΛCDM cosmology with $\Omega_\mathrm{m} = 0.27$, $\Omega_\mathrm{b} = 0.046$, $\Omega_\Lambda = 0.73$, $\sigma_8 = 0.82$, $n_\mathrm{s} = 0.96$, and $h = 0.7$, consistent with the results from Planck Collaboration et al. (2015).

4.2   Semi-Analytic Model

We use the semi-analytic model studying the formation and evolution of Pop III star forming halos described in Mebane et al. (2018) for our star formation model. We start by evolving

a set of dark matter halos from $z = 50$ to $z = 6$ and track their growth through a process similar to abundance matching (Vale & Ostriker, 2004). In this model, we assume that halos stay at the same comoving number density throughout cosmic time, and we model their growth directly from the halo mass function as in Furlanetto et al. (2017). We use fits to the dark matter numerical simulations in Trac et al. (2015) for our halo mass functions, and halos are chosen such that their $z = 6$ masses span the range $10^6 - 10^{13} M_\odot$.

4.2.1 Pop III Star Formation

Once we have a set of dark matter halos and their growth histories, we begin to add in star formation. The minihalos which first formed Pop III stars contained only pristine gas with no metals, and they were very small and susceptible to feedback. The Pop III stars which formed in them were likely very massive, and they formed at very low star formation efficiencies, perhaps even in isolation. These first stars were very important to galaxy evolution, however, as they released the first metals in their supernovae which allowed their halos to transition to metal-enriched Pop II star formation.

The first step in modeling Pop III star formation is to determine the range in halos masses which can form these stars. Pop III star formation in minihalos is driven by molecular hydrogen cooling, so a halo must first form enough H_2 for the gas to begin cooling and forming stars. Tegmark et al. (1997) find the critical fraction of H_2 required for cooling as a function of the halo's virial temperature, T, to be

$$f_{\text{crit, H}_2} \approx 1.6 \times 10^{-4} \left(\frac{1+z}{20} \right)^{-3/2} \left(1 + \frac{10 T_3^{7/2}}{60 + T_3^4} \right)^{-1} \exp \left(\frac{512\text{K}}{T} \right), \tag{4.1}$$

where $T_3 = T/10^3$ K. A halo forms this H_2 through the reaction

$$H + e^- \rightarrow H^- + h\nu \tag{4.2}$$

$$H^- + H \rightarrow H_2 + e^-. \tag{4.3}$$

At these high redshifts, cosmic microwave background (CMB) photons can destroy the H^- ions in the intermediate step of this reaction. We find a halo's current H_2 fraction by balancing the creation and destruction rates of this ion such that

$$f_{H_2} \approx 3.5 \times 10^{-4} \, T_3^{1.52}. \tag{4.4}$$

Once a halo grows large enough such that $f_{H_2} > f_{\text{crit, } H_2}$, molecular hydrogen cooling becomes efficient and Pop III stars can form (Tegmark et al., 1997).

After the first stars begin to form and build up a UV background the minimum mass for Pop III star formation is set by the Lyman-Werner (LW) background. This band consists of photons between 11.5 and 13.6 eV, and they dissociate H_2 through the Solomon process (Stecher & Williams, 1967). A halo must be large enough to shield itself against this background for it to accumulate enough H_2 for efficient cooling. Visbal et al. (2014) find this minimum mass to be

$$M_{\min} = 2.5 \times 10^5 \, M_\odot \left(\frac{1+z}{26} \right)^{-1.5} \left(1 + 6.96 \left(4\pi J_{\text{LW}} \right)^{0.47} \right), \tag{4.5}$$

where J_{LW} is the LW background in units of 10^{-21} erg s^{-1} cm^{-2} Hz^{-1} sr^{-1}. In Mebane et al. (2018) we computed the global average of the LW background, but here we will compute its spatial fluctuations as well (see section 4.3.4).

Once we know which halos can form Pop III stars, the next step is to determine the properties of those stars. The actual initial mass function (IMF) of Pop III stars is not known, although they are likely much more massive since H_2 cooling is less efficient than metal line cooling. Because of this, molecular clouds may fragment into larger pieces as they cool (e.g., Bromm et al., 1999; Abel et al., 2002). In this work we use the "low" mass IMF from Mebane et al. (2018) which has a Salpeter-like slope, a minimum mass of $20 M_\odot$, and a maximum mass set by limiting accretion through radiation pressure once a star becomes very massive and luminous. McKee & Tan (2008) calculate this mass to be

$$M_{\max} \approx 145 M_\odot \left(\frac{25}{T_3} \right)^{0.24}. \tag{4.6}$$

In general, our choice of IMF has a relatively small impact on the star formation rate density. For a more detailed discussion of this, along with models including other IMFs, see Mebane et al. (2018).

A single core collapse supernova will release $\sim 10^{51}$ erg of kinetic energy, which can be orders of magnitude above the gravitational binding energy of these high redshift minihalos. Because of this, a single supernova will often completely unbind all of the gas in the halo, even if only a small percentage of this kinetic energy binds to the gas in the halo (here we assume 10%). This has interesting implications for the transition to Pop II star formation as any metals released in the supernova will also be carried out of the halo. We allow this ejected material to re-accrete after a free-fall time, and in the meantime halos may continue to form subsequent generations of Pop III stars as they continue to accrete pristine gas.

In general, a single supernova will produce more than enough metals for a halo to make the transition to Pop II star formation. As discussed above, the more important factor is actually retaining these metals. We find that halos are able to accumulate enough metals for this transition once they have acquired enough binding energy to be able to hold on to a few percent of their gas after a Pop III supernova. Most halos tend to have ~ 10 generations of Pop III star formation, and they generally reach this binding energy very close to when they would begin atomic cooling anyway at a virial temperature of 10^4 K.

4.2.2 Pop II Star Formation

Pop II star formation is another important part of our model, as these stars heavily contribute to the LW background which sets the minimum mass for Pop III star formation (Mebane et al., 2018). We use the feedback regulated models described in Furlanetto et al. (2017) which assume that either energy or momentum is conserved in supernova winds. The star formation efficiency in these models, defined as the fraction of accreted material which turns

into stars, is

$$f_* \approx \frac{1}{1 + \eta\left(M_h, z\right)}, \tag{4.7}$$

where η is the fraction of the star formation rate which is ejected from the halo, $\dot{M}_{\mathrm{ej}} = \eta \dot{M}_*$. In the energy regulated case, η is calculated by assuming the kinetic energy released in supernovae is equal to the rate at which a halo acquires binding energy through mass accretion,

$$\eta_{\mathrm{E}} = 10\epsilon_{\mathrm{k}}\omega_{49}\left(\frac{10^{11.5}M_\odot}{M_h}\right)^{2/3}\left(\frac{9}{1+z}\right). \tag{4.8}$$

Here, a fraction $\epsilon_{\mathrm{k}} = 0.1$ of a supernova's kinetic energy binds to the gas, and supernovae release $\omega_{49} = 1$ kinetic energy per mass in stars in units of 10^{49} erg $M_\odot^{-1}$.

In the momentum regulated case, we calculate η as

$$\eta_{\mathrm{p}} = \epsilon_{\mathrm{p}}\pi_{\mathrm{fid}}\left(\frac{10^{11.5}M_\odot}{M_h}\right)^{1/3}\left(\frac{9}{1+z}\right)^{1/2}. \tag{4.9}$$

The fraction of momentum from supernovae which drives winds is $\epsilon_{\mathrm{p}} = 0.2$, and the rate of momentum injection is related to π_{fid} which is of order unity for a Salpeter IMF. These values were chosen in Furlanetto et al. (2017) to match the observed luminosity functions at high redshifts, though they differ when moving to the even higher redshifts where Pop III halos are forming and beginning to transition to Pop II star formation. The momentum regulated case, for instance, has more efficient star formation in low mass halos, creating a higher LW background. This, in turn, causes the Pop III minimum mass to rise quicker than in the energy regulated case, causing relatively few Pop III stars to form (Mebane et al., 2018). We show this in Fig. 4.1 where Pop III star formation in the momentum regulated model ends much earlier and peaks at about an order of magnitude lower than the energy regulated model. In general, the energy and momentum regulated star formation models are two extremes, and they likely bracket the true star formation process in the early Universe.
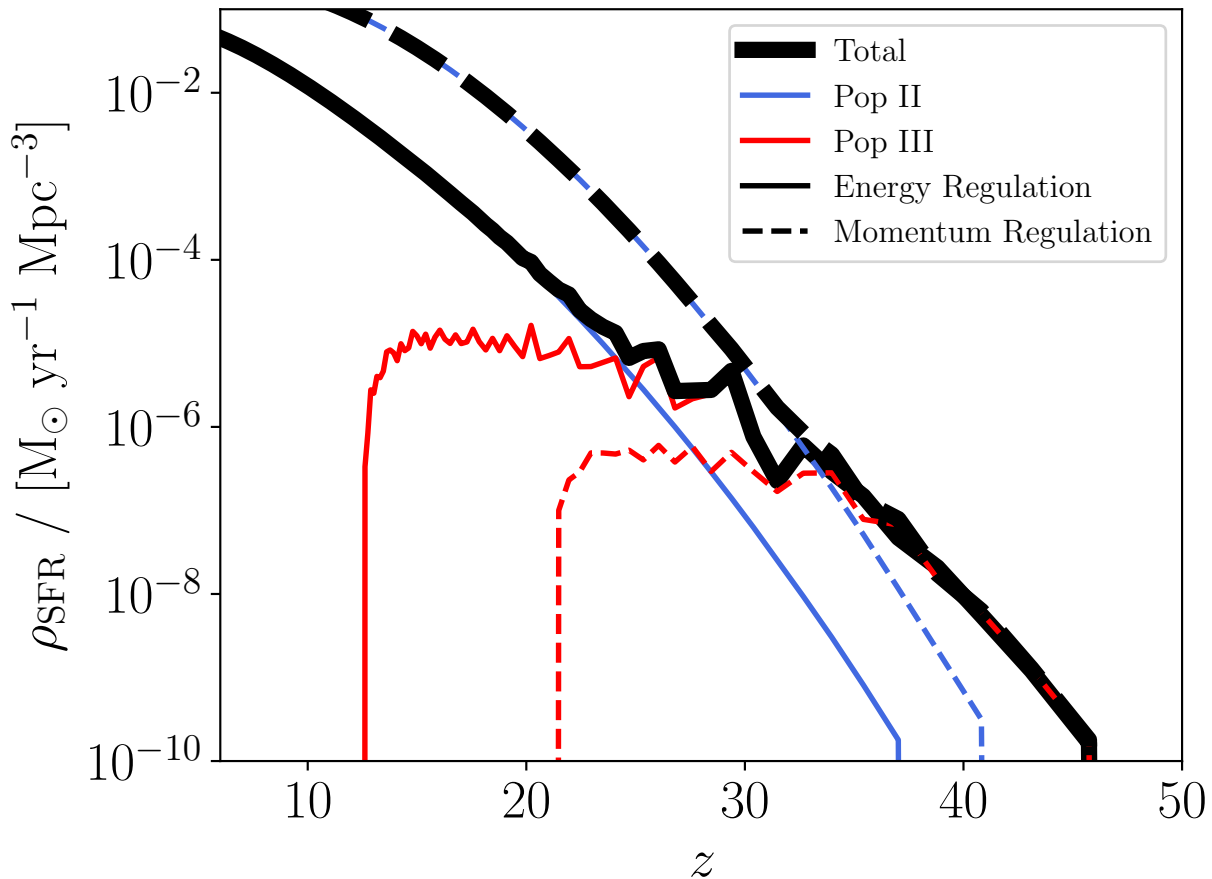
Figure 4.1: Star formation rate densities for the energy and momentum regulated cases of our semi-analytic model. Because momentum regulation for Pop II star formation allows low mass halos to form stars more efficiently, the LW background rises much more quickly in this case. This causes the Pop III minimum halo mass to quickly rise as well, cutting off Pop III star formation early.

4.3 Calculating the Cosmological 21-cm Background

The 21-cm differential brightness temperature is commonly written as the difference between the spin temperature of neutral hydrogen in the IGM, T_S, and the temperature of the cosmic microwave background (CMB), T_{CMB}. Furlanetto et al. (2006) find this relationship to be

$$\delta T_b \simeq 27 x_{HI} (1 + \delta) \left(\frac{\Omega_b h^2}{0.023} \right) \left(\frac{0.15}{\Omega_m h^2} \frac{1+z}{10} \right)^{1/2} \left(\frac{T_S - T_{CMB}}{T_S} \right) \text{ mK}, \tag{4.10}$$

where x_{HI} is the neutral hydrogen fraction and δ is the overdensity. The spin temperature of neutral hydrogen is calculated as

$$T_S^{-1} = \frac{T_{rad}^{-1} + x_\alpha T_\alpha^{-1} + x_c T_K^{-1}}{1 + x_c + x_\alpha}, \tag{4.11}$$

where T_K is the kinetic temperature of gas in the IGM, x_c is the collisional coupling coefficient, T_α is color temprature set by the strength of the Lyman-α background, and x_α is the radiative coupling coefficient from the Wouthuysen-Field effect (Wouthuysen, 1952; Field, 1958). This can be written as (Chen & Miralda-Escudé, 2004; Hirata, 2006)

$$x_\alpha = 1.81 \times 10^{11} (1+z)^{-1} J_\alpha, \tag{4.12}$$

where J_α is the Lyman-α flux computed from our model in units of s^{-1} cm^{-2} Hz^{-1} sr^{-1}.

Calculating the spatial fluctuations in this signal is necessary for computing the 21-cm power spectrum as it will allow us to probe the sources which affect the IGM on local scales. In Mebane et al. (2020) we only considered the global 21-cm signal and therefore used the global average of this background. In this work, however, we include the full spatially dependent calculation. This may be especially important when studying the contribution from Pop III star formation as Pop III minihalos are significantly more abundant than their Pop II counterparts and may affect the signal on different scales.

We use an altered version of the semi-numerical simulation code 21CMFAST (Mesinger et al., 2011) to calculate the cosmological 21-cm background. 21CMFAST generates and evolves

a cosmological density field and computes the Lyman-α, X-ray, and ionizing backgrounds necessary to compute the 21-cm signal. Here, we have improved upon the code to allow for a more general treatment of the sources which produce this signal in order to test the effects of the various star formation models from our semi-analytic model described in Section 4.2.

In the original version of 21CMFAST (Mesinger et al., 2011) the parameters governing star formation, such as the star formation efficiency and escape fraction of ionizing photons, were assumed to be constants with both halo mass and redshift. Park et al. (2019) improved upon this treatment by allowing such parameters to be power laws in halo mass, and Qin et al. (2020) extended this treatment to allow for a second population of minihalos with this same power law scaling. While these newer versions of the code do improve upon the source modeling in 21CMFAST, they do not allow for the flexibility we require to implement the results of our semi-analytic model as we find that many of these parameters are not well fit by a simple power law. In our updates to the code, we allow for any of the star formation parameters to be general functions of both halo mass and redshift. These parameters are:

1. $f_*(z, M)$: the star formation efficiency. This sets the total mass of stars to have formed in the halo's lifetime and is defined as the fraction of the halo's current baryonic mass. We input this directly from our semi-analytic model for both Pop II and Pop III star-forming halos.

2. $\mathrm{SFR}(z, M)$: the star formation rate. This is used in the calculation of both the Lyman-α and X-ray backgrounds, and we again input directly from the semi-analytic model. Because of the extreme feedback in Pop III halos, this tends to be very stochastic for Pop III while smooth for Pop II.

3. $f_{\mathrm{esc}}(z, M)$: the escape fraction. This is defined as the fraction of ionizing photons which escape the halo. Due to the extremely disruptive feedback in Pop III halos, we set $f_{\mathrm{esc}} = 1$ for Pop III halos (e.g., Xu et al., 2016) and $f_{\mathrm{esc}} = 0.1$ for Pop II (e.g.,

Robertson et al., 2015). In general, our choice of $f_{\rm esc}$ for Pop III halos does not matter, as even with a higher escape fraction they still do not produce nearly enough ionizing photons to significantly contribute to reionization.

4. The UV SED, $N_{\rm ion}$ and N_ν: $N_{\rm ion}(z, M)$ is the average number of ionizing photons produced per baryon in stars. We assume that Pop III stars produce ionizing photons more efficiently (e.g., Schaerer, 2002) and use values of $N_{\rm ion} = 4 \times 10^4$ photons per baryon for Pop III stars and $N_{\rm ion} = 5 \times 10^3$ (as in Park et al., 2019) photons per baryon for Pop II stars. If a halo contains a mixed population of both Pop III and Pop II stars, the mass-weighted average value is used, although this situation does not occur in our semi-analytic model. $N_\nu(n)$ is similar, but it defines the number of photons per baryon per unit frequency emitted between Lyman n and $n + 1$. These numbers are different for Pop III and Pop II stars, and we use the values from Barkana & Loeb (2005).

5. $M_{\rm Min}(z)$: the minimum halo mass for star formation. At the redshifts when Pop III star formation is still ongoing, this is set by the Lyman-Werner background via equation (4.5). We calculate this at each point in the box to find the spatially-dependent Lyman-Werner background and Pop III minimum mass. Since the horizon for the Lyman-Werner background is very large (~ 100 Mpc), we find that the minimum mass is largely constant across the box, and our results are consistent with Mebane et al. (2018) where we only calculate the global average.

The parameters $f_*(z, M)$ and $\mathrm{SFR}(z, M)$ are taken from our semi-analytic model which tracks the growth and star formation in individual halos. 21CMFAST, however, calculates the radiation fields necessary to compute the signal as integrals over halo mass for each cell in the box (described in the following sections). We set up interpolation tables in both halo mass and redshift to interface these two models and provide the star formation results from the semi-analytic model to 21CMFAST.

In the following subsections we describe in detail the calculation of the radiation backgrounds which produce the 21-cm signal from these parameters.

4.3.1 The Lyman-α Background

At any point in the box, we calculate the Lyα background as

$$J_\alpha(z, \mathbf{r}) = \frac{(1+z)^3}{4\pi} \int_z^\infty c \left| \frac{\mathrm{d}t}{\mathrm{d}z'} \right| \epsilon_\alpha \mathrm{d}z'. \tag{4.13}$$

Here, ϵ_α is the emissivity of the Lyα background found by integrating over the halos at a given redshift, z', and location, and is calcuated as

$$\epsilon_\alpha(z', \mathbf{r}) = \int_{M_{\mathrm{Min}}(z')}^\infty \phi_{\mathrm{c}}(z', \mathbf{r}) \mathrm{SFR}(z', M) \mathrm{d}M \sum_{n=2}^{n_{\mathrm{max}}} N_\nu(n) f_{\mathrm{rec}}(n), \tag{4.14}$$

where $N_\nu(n)$ is the number of photons emitted between Lyman n and $n+1$ per unit frequency per mass in stars from Barkana & Loeb (2005) for either Pop II or Pop III star formation, and $\phi_{\mathrm{c}}(z', \mathbf{r})$ is the conditional mass function. $f_{\mathrm{rec}}(n)$ is the fraction of Lyman-n photons absorbed by neutral hydrogen in the IGM which are recycled into Lyα photons (Hirata, 2006; Pritchard & Furlanetto, 2006). At $n > n_{\mathrm{max}}$ a photon emitted at z' will redshift into the $n-1$ resonance before redshift z and be absorbed by neutral hydrogen in the IGM. Eq. 4.13 is calculated as a spherical average over all lines of sight as computed in eq. 4.14. The Lyα background for the models presented in this work is shown in Fig. 4.2.

The inputs to this calculation from our semi-analytic model are the star formation rate of both Pop II and Pop III star forming halos along with the minimum halo mass for star formation. We then use J_α with eqs. 4.10, 4.11, and 4.12 to compute the 21-cm signal. In the energy regulated case, this occurs around when Pop II star formation has begun to surpass Pop III in the Universe, and their contributions to J_α are roughly comparable. For momentum regulation, Pop III star formation occurs at such a small rate that the Pop II contribution to J_α dominates.
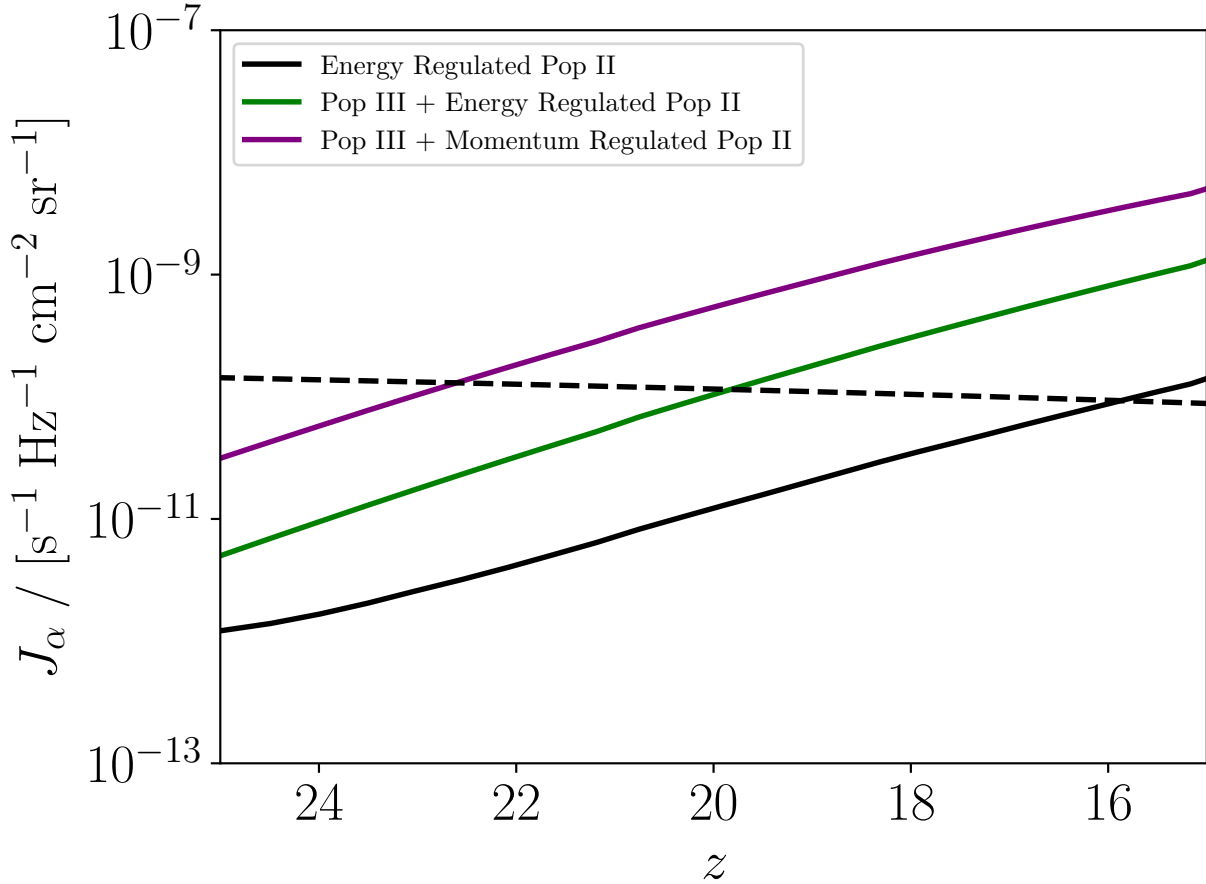
Figure 4.2: Lyα background for the various models presented in our paper. The dashed curve shows the critical Lyα background necessary for coupling to begin (Ciardi & Madau, 2003). The momentum regulated model begins coupling first as it has the most efficient Pop II star formation. The case with energy regulated Pop II star formation couples last, as it does not have any Pop III star formation occuring below the atomic cooling threshold, and energy regulated star formation has a lower efficiency.

4.3.2 The X-ray Background

We follow the calculation of the X-ray background in 21CMFAST laid out in Park et al. (2019) and Qin et al. (2020), where we assume an X-ray spectrum between 0.5-2.0 keV of the form $L_X(E) \propto E^{-\alpha}$. The upper limit here is set due to the mean free path of X-rays above 2 keV exceeding the Hubble length, so such photons are not efficiently absorbed by the IGM and do not contribute significantly to its heating. We follow Das et al. (2017) for the lower limit of 0.5 keV set by the host galaxy's ISM, and we set $\alpha = 1$ to best match their X-ray SED.

The X-ray background is then calculated similarly to the Lyα background with an emissivity of

$$\epsilon_X(z', \mathbf{r}) = \int_{M_{\mathrm{Min}}(z')}^{\infty} f_X(z', M)\phi_c(z', \mathbf{r})\mathrm{SFR}(z', M)\mathrm{d}M\frac{\mathrm{d}L_{X,\mathrm{SFR}}}{\mathrm{d}E}. \tag{4.15}$$

Here, $\frac{\mathrm{d}L_{X,\mathrm{SFR}}}{\mathrm{d}E}$ is the specific X-ray luminosity per unit star formation rate following the spectrum described above and normalized by $L_{X,\mathrm{SFR}} = 10^{40.5}$ erg s^{-1} $(M_\odot \text{ yr}^{-1})^{-1}$.

We also include a dimensionless scaling factor, f_X, to boost the X-ray emission in certain halos. In the models shown here, we set $f_X = 1$ for Pop II star forming halos and vary it for Pop III halos. We will show in section 4.4 that our choice of f_X for Pop III halos can have a large effect on the 21-cm signal.

We note that our calculation of the X-ray background here is slightly different than our calculation in Mebane et al. (2020) which assumes an SED from 0.2-30 keV and $\alpha = 1.5$. We also calculate the X-ray background directly from the star formation rate here, while in Mebane et al. (2020) we used the remnant black hole mass density from star formation. If there is a large delay between Pop III star formation and the formation of accreting black holes these details of the calculation may become important. It is difficult to judge this, however, as assumptions about the growth of black holes such as their duty cycle and accretion efficiency are by far the largest source of uncertainty. The parameter f_X, however,

has the same meaning in both models, as it is simply a dimensionless boost to X-ray emission from Pop III halos.

4.3.3 The Ionizing Background

21CMFAST computes the ionizing background slightly differently than the Lyα and X-ray backgrounds as it uses the total number of stars formed in a halo rather than the current star formation rate. A region in the box is considered fully ionized when the total number of ionizing photons which have been produced inside the box exceeds the total number of neutral hydrogen atoms plus any recombinations that have occured. The total number density of ionizing photons ber baryon produced is

$$n_{\mathrm{ion}}(z, \mathbf{r}) = \rho_b^{-1} \int_{M_{\mathrm{Min}}(z)}^{\infty} \phi_{\mathrm{c}}(z, \mathbf{r}) f_*(z, M) M \frac{\Omega_b}{\Omega_m} N_{\mathrm{ion}}(z, M) f_{\mathrm{esc}}(z, M) \mathrm{d}M, \qquad (4.16)$$

where ρ_b is the local baryon density in the region. 21CMFAST also computes the local recombination rate of ionized hydrogen throughout the box, although this calculation does not depend on any of our changes to the code. We refer the reader to Sobacchi & Mesinger (2014) for an explanation of this calculation.

We note that our inclusion of Pop III star formation does not significantly affect the course of reionization in any of our models. By the time the Universe has begun to reionize in earnest, Pop II star formation completely dominates the ionizing photon budget of the Universe, so our choice of Pop III model does not matter.

4.3.4 The Lyman-Werner Background

We also calculate the spatially-dependent Lyman-Werner background in a very similar manner to the Lyα background discussed in section 4.3.1. The Lyα background is generated by emission from neutral hydrogen in the IGM when a photon between Lyman-n and $n+1$ in the

rest frame redshifts into Lyman-n and is absorbed. The LW background, on the other hand, is produced from direct UV stellar emission and is attenuated by absorption in the neutral IGM as it redshifts, producing the "sawtooth" spectrum described in Haiman et al. (1997). We follow Ahn et al. (2008) and describe this spectrum using the picket fence modulation factor f_{mod} which is defined as the fraction of the total emission in the LW band oberserved at redshift z from a source at redshift z' and comoving separation r_c (in units of comoving Mpc). We use their provided fitting formula which matches the exact calculation to within 2%,

$$f_{\mathrm{mod}} = 1.7 \exp\left[-(r/116.29\alpha)^{0.68}\right] - 0.7, \tag{4.17}$$

where α is given by

$$\alpha = \left(\frac{h}{0.7}\right)^{-1}\left(\frac{\Omega_m}{0.27}\right)^{-1/2}\left(\frac{1+z'}{21}\right)^{-1/2}. \tag{4.18}$$

We then compute the emissivity as in equation 4.14, except that we now modulate the sum over the relevant portions of the spectra from Barkana & Loeb (2005) by f_{mod}.

The horizon for this background is very large (around 100 comoving Mpc), and we find that the background is very homogenous at all redshifts in this calculation, varying by no more than a few percent (see also, Ahn et al., 2008; Holzbauer & Furlanetto, 2012; Qin et al., 2020). Therefore, the minimum mass for Pop III star formation does not vary appreciably across the box, and we obtain the same results if we include the full spatially dependent calculation of the LW background as if we just use the average value from the semi-analytic model.

Regardless of the fluctuations in this background, we compute the minimum mass of Pop III star formation at each point in the box from eq. 4.5. If fluctuations are large, we use an interative approach where we first run our semi-analytic model with no fluctuations in the background, use the results from this run in 21CMFAST, and then re-run the semi-analytic model with the minimum mass computed at representative locations within the box. In principal we would continue this process until we converge upon the true fluctuations in

the minimum mass, although we find that this entire process is unnecessary because of the homogeneity of the background.

4.4 Results

In this section we describe the results of combining our star formation model from the semi-analytic model presented in section 4.2 with our modified version of 21CMFAST described in section 4.3. All models were run in a 300 cMpc box, and each individual cell was 1.5 cMpc across.

Fig. 4.3 shows the average differential brightness temperature, or global signal, throughout our entire box for a number of models. Here, we have varied f_X for Pop III star formation from 1 to 100 due to uncertainties in the emission process of X-rays from Pop III remnants. In general, we find that our choice of f_X changes the shape of the global signal and the amplitude of the power spectrum without affecting the timing. If f_X is high, early heating of the IGM from the X-ray background can cause the kinetic temperature of the gas to rise, causing a shallower absorption signal. Regardless of f_X, the strong Lyα background from Pop III star formation will cause the spin temperature of the neutral hydrogen in the IGM to drop toward the lower kinetic temperature, causing an early and deep absorption signal. If Pop II star formation is momentum regulated we may see an even earlier absorption signal due to the increased efficiency of star formation in low mass Pop II halos.

These results qualitatively agree with our results from Mebane et al. (2020), although we do not directly compare here as we do not include an excess radio background from accreting Pop III remnants. The global signals shown here are much smoother than in Mebane et al. (2020) as they are computed as an average of the differential brightness temperature across many points in the box.
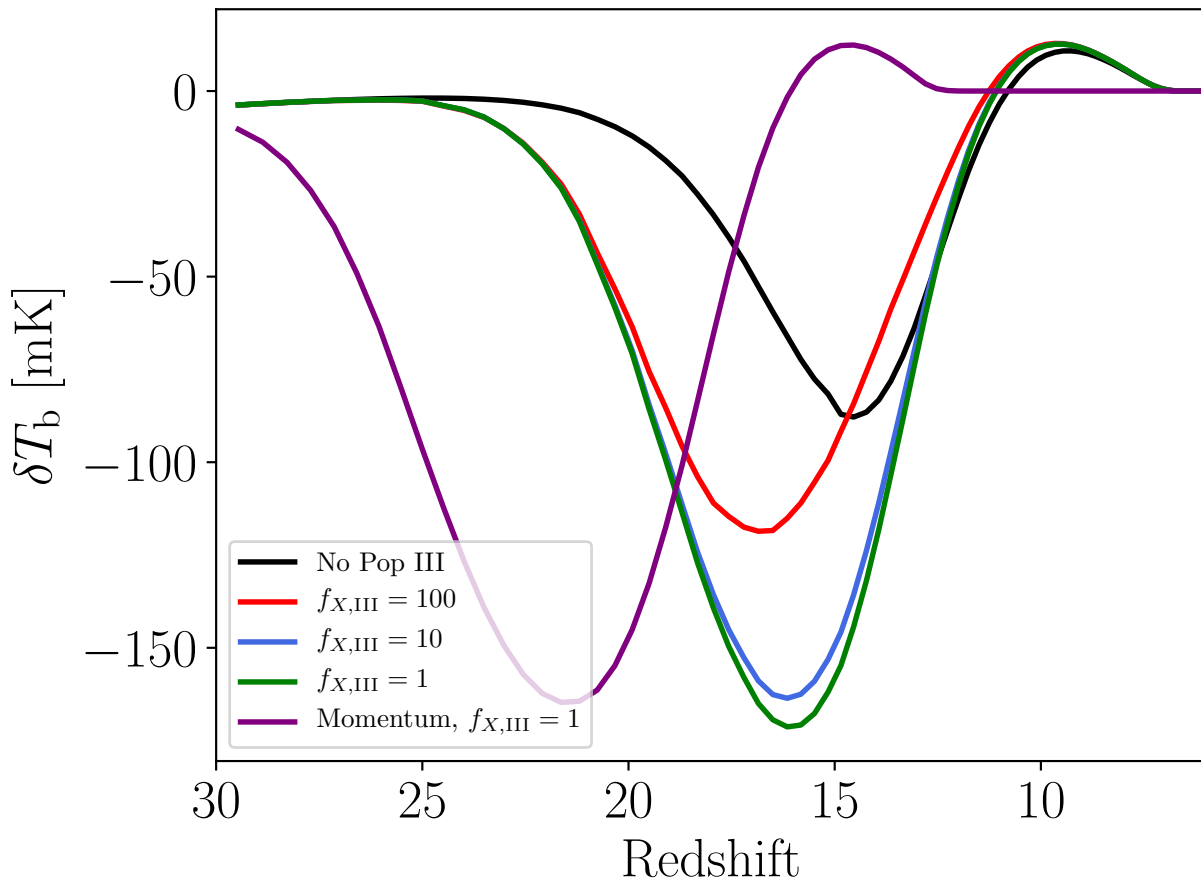
Figure 4.3: 21-cm global signal for a variety of models. Our choice of f_X for Pop III star formation can affect the signal, causing a smaller absorption feature at high f_X without altering the timing. All models assume energy regulation for Pop II star formation except the purple curve which assumes momentum regulation. We see a slightly earlier absorption signal in this case due to the increased star formation efficiency of low mass Pop II halos.
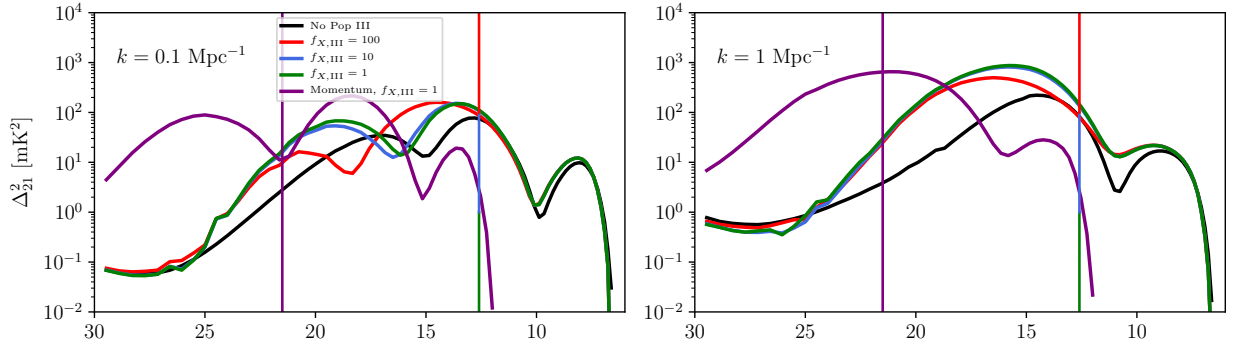
Figure 4.4: 21-cm power spectrum at $k = 0.1$ Mpc^{-1} (left) and $k = 1$ Mpc^{-1} (right). The vertical lines here show when Pop III star formation ends for the momentum and energy regulated cases. Even after this mode of star formation ceases, the cumulative effect of X-ray heating can still alter the signal. The three peaks in the $k = 0.1$ Mpc^{-1} panel correspond to the Lyα coupling, X-ray heating, and reionization phases of the signal.

4.4.1 Fluctuations in the 21-cm Signal

The evolution of the 21-cm signal due to star formation generally occurs in three phases (Furlanetto, 2006), and it is shown in Fig. 4.4. The first is when early star formation is able to produce a significantly strong Lyα background to cause the signal to appear in absorption. This is shown in Fig. 4.2, and it can be seen in the global signal in Fig. 4.3 and the power spectrum as the first bump in Fig. 4.4. The next phase occurs when a significant X-ray background is built up from the remnants of star formation and begins to heat the IGM. This raises both the kinetic and spin temperatures of the gas, resulting in a rise out of absorption, potentially causing the signal to show in emission. This is shown as the second bump in Fig. 4.4. As star formation continues to increase, the resulting UV background will ionize the neutral hydrogen in the IGM, causing the global signal (and fluctuations in the background) to vanish.

In our model, Pop III stars form in minihalos which are far more abundant than the typical
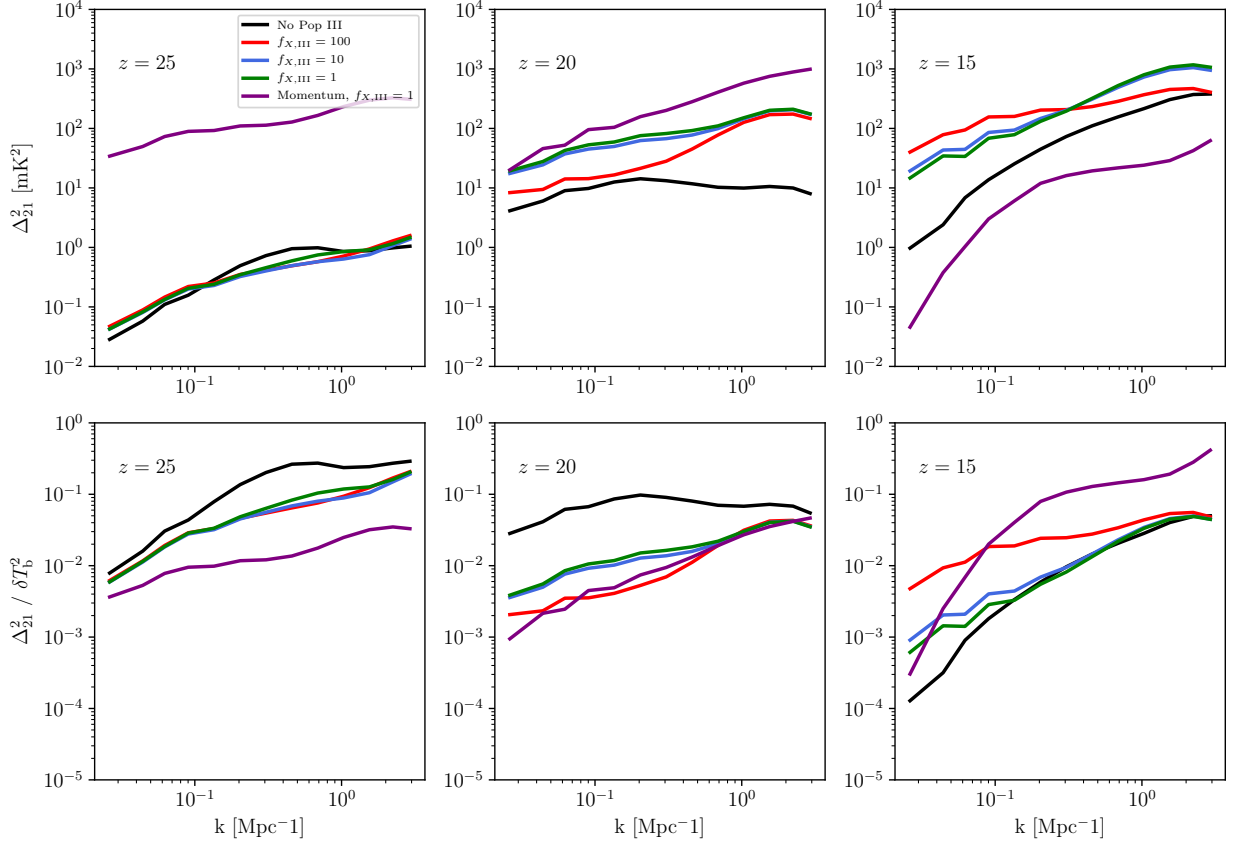
Figure 4.5: 21-cm power spectrum at $z = 25$ (left), $z = 20$ (middle), and $z = 15$ (right). The top panel shows the power spectrum in mK^2, and the bottom panel shows the power spectrum in units of the global signal squared at that redshift in order to better highlight differences in shape. In the Pop II case we see a flattening of the power spectrum on small scales and at higher redshifts that is not present in any of the models including Pop III star formation. When including the global signal data in the bottom panels we see larger differences between some models that are not evident in the top panels. For example, the momentum regulated Pop II case, which has very high Pop II star formation but low Pop III, is much easier to differentiate from the other models in our $z = 15$ panel. This highlights the importance of understanding both the global signal and the power spectrum.

atomic cooling halos used in most models containing only Pop II stars. Depending on the specifics of their formation and their contribution to the radiation backgrounds discussed in section 4.3, they may affect the cosmological 21-cm signal on different scales than expected for models containing only atomic cooled halos. While this effect does not appear to be very strong, we do see it manifest in Fig. 4.5. There is slight flattening of the power spectrum at $k \gtrsim 0.5 \ \mathrm{Mpc}^{-1}$ in the case without Pop III star formation which is not present in the models including Pop III stars.

There are also interesting differences in the overall power in these models. The increased Lyα background from the addition of Pop III stars causes higher fluctuations in the background, especially at early times. This is why there is more power in Fig. 4.5 in the Pop III models at the redshifts corresponding to the largest differences in the global signal. When comparing between Pop III models with different values of f_X, higher X-ray emission generally leads to reduced power. This is because increased X-ray heating means that it occurs very rapidly after Lyman-α coupling, preventing the coldest IGM features from becoming visible and reducing the contrast in the map.

4.4.2 Early X-Ray Heating

Even after Pop III star formation has ended there are still differences between the models in their power spectra. This is caused by the cumulative effects of X-ray heating from Pop III star formation. If Pop III stars are able to effectively heat the IGM at early times, this can carry over into even the lower redshifts of the signal and show up as a higher kinetic temperature than one might expect if you only include Pop II star formation. This is difficult to see in the global signal, though it may be more evident in the power spectrum, especially at smaller scales.

Mirocha et al. (2017) found that, in models without Pop III star formation, the X-ray heating and ionization phases of the 21-cm signal occur at similar times and are difficult to distinguish. When we include Pop III star formation, however, this early heating causes these two phases to be more distinct, and their effect on both the global signal and the power spectrum may help us distinguish between Pop II and Pop III star formation. Mirocha et al. (2018) updated their models to include Pop III star formation and found an assymetry in the absorption feature of the global signal, though we do not see that here.

4.4.3 Degeneracies

The energy and momentum regulated models discussed in section 4.2.2 are extremes, and "true" Pop II star formation likely lies somewhere in between. Because of this, it may be difficult to differentiate models with and without Pop III star formation with only a measurement of the global signal. Fortunately, due to the increased abundance of Pop III star forming halos, they may affect the signal on different scales which can be detected in the power spectrum. Indeed, we see these differences in Fig. 4.5 where Pop III models with energy regulated Pop II star formation have a larger power, especially at small scales. Understanding these modes of star formation in the early Universe will likely require measurements of both the 21-cm global signal and power spectrum.

There may certainly be other degeneracies with parameters we do not discuss here. For example, if Pop III star formation is much more efficient, it may produce a large enough Lyα background to produce very early coupling as in our momentum regulated Pop II model. If this Pop III star formation ends around the same time as our energy regulated models, though, we should see differences in the global signal and power spectrum at lower redshifts, as in the lower right panel of Fig. 4.5 at $z = 15$. There may also be subtle differences depending on the Pop III IMF. In Mebane et al. (2020) we found that the IMF can change the shape of the global signal without altering its depth or timing. These changes were

minor, though they may be useful to learn about the Pop III IMF by studying both the global signal and the power spectrum.

4.4.4   Comparison to Previous Works

Qin et al. (2020) also present a model for the 21-cm signal using 21CMFAST with Pop III minihalos, though they assume that the parameters governing both Pop III and Pop II star formation are independent of redshift and obey power laws in halo mass. This differs from our model, where Pop III star forming halos typically have very similar stellar masses regardless of halo mass since we assume these stars form in isolation. We also explicity track individual halos in our model, which allows us to include a criterion for the transition to Pop II star formation by modeling metal creation and retention by Pop III stars and their halos. Their models also have a significantly higher star formation efficiency in Pop III halos. This is offset in their calculation of the Lyα and X-ray backgrounds as they assume that all star formation in both Pop III and Pop II halos occurs over a timescale of half of a Hubble time. We find that this timescale is far too long, especially for Pop III halos, so we input the star formation rates for individual halos directly from our semi-analytic model.

In general, our energy regulated model is in good agreement with the global signal for their fiducial model, which assumes that X-ray emission from Pop III star formation occurs with $f_{X,\mathrm{III}} = 1$. They do not investigate changes in the shape of the power spectrum due to Pop III star formation, though we do find good agreement in the timing of the features in the power spectrum in our fiducial models.

4.5   Conclusions

We have presented a model studying the effects of Pop III star formation on the cosmological 21-cm power spectrum. We combined the semi-analytic model for Pop III star formation described in Mebane et al. (2018) with an altered version of the 21-cm simulation code 21CMFAST (Mesinger et al., 2011). In particular, we have made changes to the code that allow us to input any generic function for the various star formation parameters used to calculate the radiation backgrounds which set the 21-cm signal. In general, we find that Pop III star formation can have a significant effect on the timing of the 21-cm power spectrum but a modest effect on its shape and the details of X-ray emission from Pop III star formation can affect the amplitude of the signal without altering its timing.

Specifically, we find

1. The largest difference between models with and without Pop III star formation is in the timing of the 21-cm signal. In all models, we see a strong three-peaked structure to the power spectrum indicating the Lyα coupling, X-ray heating, and reionization phases of the signal. Recent models have shown that, when only Pop II sources are included, the X-ray heating and reionization eras may overlap, so Pop III sources play an important role in the evolving power spectrum (e.g., Mirocha et al., 2017; Mirocha & Furlanetto, 2019).

2. We find a modest variation in the shape of the 21-cm power spectrum when including Pop III star formation, which increases the relative importance of the small-scale power. While this effect is small, it can be used to differentiate between degenerate global signals where models with and without Pop III star formation may be indistinguishable.

3. Even after Pop III star formation ends it can still affect the 21-cm signal due to its contribution to early X-ray heating.

4. X-ray heating from Pop III star formation can have a large effect on the amplitude of the 21-cm signal. In models with high X-ray emission, the IGM can experience large heating early on which causes the magnitude of the aborption signal to lessen. Understanding the specific mechanisms for X-ray emission from Pop III remants will be important in learning how to discern the properties of Pop III star formation from a measured 21-cm signal.

5. The spatial variations in the Pop III minimum mass due to inhomogeneities in the Lyman-Werner background are very small due to the large horizon of the LW background. Because of this, it is sufficient to use the globally averaged LW background and assume that the minimum mass does not spatially vary.

Since Pop III star formation in minihalos occurs at such low rates, it is likely that our only method of detecting their presence will be through indirect methods such as the cosmological 21-cm signal. Most of our Pop III models do predict a high power in wavenumbers which will be probed by the Hydrogen Epoch of Reionization Array (HERA) and the Square Kilometre Array (SKA), so observations of the 21-cm signal by these instruments should help to constrain the parameter space described in our models.

CHAPTER 5

The Effects of Warm Dark Matter on the Formation of the First Stars and the Cosmic 21-cm Background

5.1 Introduction

There is still very little known of the exact nature of dark matter. While most cosmological models focus on cold dark matter with small thermal velocities, there have also been many studies involving thermalized dark matter particles such as the sterile neutrino (see Kusenko 2009 for a review). Understanding the nature of dark matter in the Universe is a fundamental question in physics and cosmology, and it may provide a compelling explanation for the lack of observed satellite galaxies compared to CDM models (e.g., Moore et al., 1999; Springel et al., 2008) and the difference in slope of the inner density profile of halos in simulations and observations (the so-called "core-cusp" problem, e.g., Gentile et al., 2009; de Blok, 2010).

Many constraints on warm dark matter come from gravitational lensing (e.g., Miranda & Macciò, 2007; Inoue et al., 2015; Birrer et al., 2017; Gilman et al., 2019; Brehmer et al., 2019; Gilman et al., 2020) and the Lyman-α forest (e.g., Boyarsky et al., 2009; Wang et al., 2013; Markovič & Viel, 2014; Baur et al., 2017; Garzilli et al., 2019a). These methods work by probing the cosmological density field to understand the effect of warm dark matter on structure formation. In general, warm dark matter increases the velocity dispersion of dark matter and smooths out small-scale structure, suppressing the formation of halos with virial

velocities below this scale. Current limits from gravitational lensing (Gilman et al., 2020) suggest the halo mass scale at which this effect is strongest is $m_{\rm hm} \lesssim 10^8 M_\odot$, corresponding to a thermal dark matter particle mass of $m_{\rm DM} \gtrsim 5.0$ keV. Depending on the models used, this effect can be strongest in minihalos with very low masses (i.e., $\lesssim 10^9 M_\odot$) and at very high redshifts when the first stars formed. If warm dark matter exists and affects the formation of these minihalos, we may be able to learn much of its properties from the formation of the first stars.

The actual first generation of stars, known as Population III (Pop III), form from pristine, metal-free gas in minihalos below the atomic cooling threshold. These stars form through molecular hydrogen cooling, and they are thought to have a relatively higher mass and luminosity than more traditional stars which form through metal-line cooling (Bromm et al., 1999; Abel et al., 2002; Bromm, 2013). The minihalos in which they form were very small, and were therefore highly susceptible to feedback. Because of this, these Pop III stars likely formed at extremely low efficiencies, or even in isolation (Machacek et al., 2001; Wise & Abel, 2007; O'Shea & Norman, 2008; Shapiro et al., 2004; Visbal et al., 2018; Mebane et al., 2018).

There has yet to be a direct observation of a Pop III star, so the parameters governing their formation are highly uncertain. Much of our knowledge of Pop III star formation, therefore, has come from analytical models (e.g., McKee & Tan 2008; Kulkarni et al. 2013), numerical simulations (e.g., Machacek et al. 2001; Wise & Abel 2007; O'Shea & Norman 2008; Xu et al. 2016; Stacy et al. 2012; Hirano et al. 2015; Maio et al. 2010; Sarmento et al. 2018), or semi-analytic models (e.g., Trenti et al. 2009; Crosby et al. 2013a; Jaacks et al. 2018; Visbal et al. 2018; Mebane et al. 2018). Because of their low formation efficiency, it is highly unlikely that we will observe a Pop III star with even the next generation of telescopes such as JWST (Schauer et al. 2020 find we may need a 100 m space telescope to directly observe these stars).

One potential avenue to indirectly detect Pop III star formation is the cosmological 21-cm background. There has only been one claimed detection of this signal by the EDGES experiment (Bowman et al., 2018), although this detection may be an artifact of instrument effects (e.g., Hills et al., 2018; Sims & Pober, 2020; Tauscher et al., 2020) and needs to be confirmed by another experiment. This signal is highly dependent on the UV and X-ray backgrounds caused by star formation in the early Universe, so understanding this mode of star formation is very important to properly modeling it (e.g., Mirocha et al., 2018; Mebane et al., 2020). If warm dark matter affects the abundance of star-forming halos substantially, it will become another important factor in understanding the 21-cm background.

There have been many studies on the effects of warm dark matter on star formation and the cosmic 21-cm background (e.g., Yoshida et al., 2003; Safarzadeh et al., 2018; Boyarsky et al., 2019; Lopez-Honorez et al., 2019; Chatterjee et al., 2019), though few have also studied the combined effect of Pop III stars with a detailed model of their formation. But the Pop III era is of critical importance for understanding the implications of warm dark matter, because they form in the smallest halos ($M \lesssim 10^8 \ M_\odot$) that are most susceptible to the smoothing induced by the finite velocity dispersion of warm dark matter. At the same time, the physics of Pop III stars is sufficiently different from "normal" galaxies that their properties cannot simply be extrapolated from normal galaxy formation models (e.g., Visbal et al., 2018; Jaacks et al., 2018; Mebane et al., 2018). In this paper we study the effects of warm dark matter on star formation and the cosmic 21-cm background in the early Universe. We improve upon past calculations by combining a detailed semi-analytic model for the formation and evolution of Pop III halos described in Mebane et al. (2018) with an altered halo mass function from warm dark matter. In particular, we are interested in studying the magnitude of the delay in both Pop II and Pop III star formation as well as its implications for two observables, the primary absorption feature of the 21-cm signal due to warm dark matter and the UV luminosity function. Due to the small size of these minihalos, we can potentially probe structure formation at much smaller scales than gravitational lensing or the Lyα forest.

In Section 5.2 we describe our semi-analytic model for Pop III star formation including warm dark matter, and we discuss our results related to star formation and the cosmic 21-cm background in Section 5.3. We conclude in Section 5.4.

In this work, we assume a flat cosmology with $\Omega_\mathrm{m} = 0.28$, $\Omega_\mathrm{b} = 0.046$, $\Omega_\Lambda = 0.72$, $\sigma_8 = 0.82$, $n_\mathrm{s} = 0.95$, and $h = 0.7$, consistent with the results from Planck Collaboration et al. (2015).

5.2   Semi-Analytic Model with Warm Dark Matter

Here we describe our semi-analytic model for the formation and evolution of Pop III star forming halos, described in more detail in Mebane et al. (2018). We update the model here to include the effects of warm dark matter, which alters the formation of structure and the halo mass function.

5.2.1   The Halo Mass Function

The first ingredient in our model is the formation and growth of dark matter halos. Halos are initialized at $z = 50$ and evolved until $z = 6$, and their masses are chosen such that their final masses span the range of $10^6 - 10^{13} M_\odot$. The growth of halos is modeled using abundance matching (e.g., Vale & Ostriker, 2004). We assume halos stay at a constant number density throughout cosmic time, allowing us to track their growth directly from the halo mass function (Furlanetto et al., 2017).

We use fits to the high redshift dark matter simulations from Trac et al. (2015) for our fiducial mass functions with no warm dark matter. When including warm dark matter we assume the mass function takes the form (Schneider et al., 2012)

$$\frac{\mathrm{d}N_\mathrm{wdm}}{\mathrm{d}m} = \frac{\mathrm{d}N_\mathrm{cdm}}{\mathrm{d}m} \left(1 + \frac{m_\mathrm{hm}}{m}\right)^{-\beta}, \tag{5.1}$$

where $\frac{\mathrm{d}N_{\mathrm{cdm}}}{\mathrm{d}m}$ is the cold dark matter mass function from Trac et al. (2015) and m_{hm} is the halo mass where the warm dark matter power spectrum is reduced by half compared to the cold dark matter power spectrum (e.g., Schneider et al., 2012; Lovell et al., 2014). The parameters m_{hm} and β depend on the particular warm dark matter model. Here, we assume $\beta = 1.16$ as in Schneider et al. (2012) and vary m_{hm} to investigate the mass scales at which the suppression of formation affects star formation in the early Universe. We also include a model with $\beta = 1.3$ as in Lovell et al. (2014) and $m_{\mathrm{hm}} = 10^{10} M_{\odot}$ to test variations in β, although the relatively small range in these model fits to β means this does not have much of an effect compared to variations in m_{hm} and the star formation model. Fig. 5.1 shows the mass functions used in our model. The abundance of halos is drastically reduced as m_{hm} increases, especially in low mass halos which will form Pop III stars.

In general, the accretion rates of halos with warm dark matter are higher below m_{hm}, and above they are consistent with cold dark matter models. In the more extreme cases the halo mass function can turn over at lower redshifts, causing our abundance matching approach to break down. This happens well after the time of Pop III star formation, though, so it does not affect our model. Behroozi & Silk (2015) find that the majority of halo growth at these redshifts comes from smooth accretion of material from the intergalactic medium (IGM), so our model only accounts for the average growth of halos and does not include the effects of mergers. This growth must occur very rapidly, as small halos in these warm dark matter models are very rare yet are still the seeds for larger dark matter halos.

5.2.2 Population III Star Formation

The next step in our model is to add stars to the dark matter halos discussed in section 5.2.1. The first star-forming minihalos were very different than the galaxies we observe today due to their extremely low mass and binding energy, along with their lack of metals. Because of this, Pop III stars were likely more massive than stars formed through metal-line cooling,
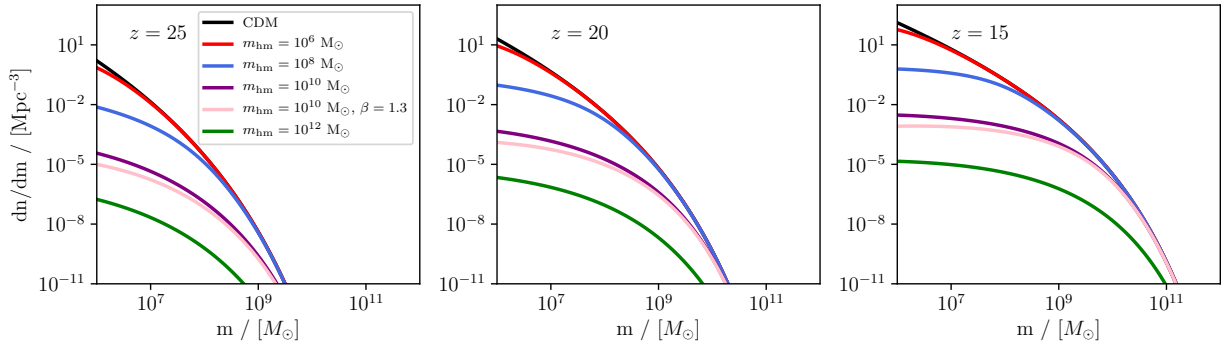
Figure 5.1: Halo mass functions at the redshifts relevant to Pop III star formation for a variety of models with and without warm dark matter. Our fiducial CDM mass functions from Trac et al. (2015) are shown in black, and the colored lines show a number of warm dark matter models with m_{hm} ranging from 10^6 to $10^{12} M_\odot$. At higher values of m_{hm} the mass function can be suppressed by many order of magnitude. This effect is greatest at the low masses and high redshifts at which Pop III stars form in minihalos. The pink curve shows a model with $\beta = 1.3$.

and they probably formed in isolation as feedback from their radiation and explosions could completely disrupt the gas in a halo. After these first stars formed, however, their supernovae released metals which could allow a halo to transition to more traditional star formation.

The first ingredient in this model is to understand the halo mass range in which Pop III star formation occurs. This is set mostly by the physics of H_2 cooling, as a halo must first accumulate enough H_2 to begin to efficiently cool and form stars. The fraction of H_2 required for this cooling is given by

$$f_{\text{crit, H}_2} \approx 1.6 \times 10^{-4} \left(\frac{1+z}{20} \right)^{-3/2} \left(1 + \frac{10T_3^{7/2}}{60 + T_3^4} \right)^{-1} \times \exp \left(\frac{512\text{K}}{T} \right), \qquad (5.2)$$

where $T_3 = T/10^3$ K and T is the halo's virial temperature (Tegmark et al., 1997). The actual formation channel of this H_2 is

$$\text{H} + \text{e}^- \rightarrow \text{H}^- + h\nu \qquad (5.3)$$

$$\text{H}^- + \text{H} \rightarrow \text{H}_2 + \text{e}^-. \qquad (5.4)$$

The intermediate step of creating H^- ions is crucial to this process, as cosmic microwave background (CMB) photons can easily destroy these ions at high redshift. Tegmark et al. (1997) found the fractional abundance of H_2 in halos as a function of their virial temperature by balancing the creation and destruction rates of these ions as

$$f_{\text{H}_2} \approx 3.5 \times 10^{-4} \ T_3^{1.52}. \qquad (5.5)$$

Therefore, a halo is able to begin forming Pop III stars when $f_{\text{H}_2} > f_{\text{crit, H}_2}$.

This method for determining the minimum halo mass of Pop III star formation only works for the very first star-forming halos, as once an appreciable UV background is built up by star formation, the Lyman-Werner (LW) background becomes the dominant process. LW photons have energies between 11.5 and 13.6 eV and can dissociate H_2 through the Solomon process (Stecher & Williams, 1967). If a halo is present in a large enough LW background, it

will need to exceed a certain minimum mass to be able to shield itself from this background and continue producing H_2. This minimum mass can be written as

$$M_{\text{min}} = 2.5 \times 10^5 \ M_{\odot} \left(\frac{1+z}{26} \right)^{-1.5} \left(1 + 6.96 \left(4\pi J_{\text{LW}} \right)^{0.47} \right), \tag{5.6}$$

where J_{LW} is the LW background (Visbal et al., 2014). We compute this background self-consistently from the star formation in our model in a very similar fashion to the Lyman-α background (see section 5.3.2). Once the LW background becomes the dominant process for determining the minimum mass, we require all new star-forming halos to exceed this mass. Some studies find that the relative stream velocity between baryons and dark matter instead sets the minimum mass for Pop III star formation (e.g., Schauer et al., 2019). In general, we find that our LW minimum mass is the dominant except in the most extreme regions.

The initial mass function (IMF) of Pop III stars is unknown, although it is thought that they were very massive due to the reduced efficiency of H_2 cooling compared to metal-line cooling (e.g., Bromm et al., 1999; Abel et al., 2002). While we test a number of different IMFs in Mebane et al. (2018) and Mebane et al. (2020), we only include our "low" mass fiducial model here as the IMF has a relatively small effect on the star formation rate density and the differences in the halo mass function which we investigate here are much larger. This IMF has a Salpeter-like slope, a minimum mass of $20 M_{\odot}$, and a maximum mass of $\sim 145 M_{\odot}$ set by limiting accretion onto a newly-formed star once it is luminous enough to stop growth due to radiation pressure. McKee & Tan (2008) find this maximum mass to be

$$M_{\text{max}} \approx 145 M_{\odot} \left(\frac{25}{T_3} \right)^{0.24}. \tag{5.7}$$

We assume that stars form in isolation in our model as supernova feedback can often eject all of the gas in a halo. A single supernova will release $\sim 10^{51}$ erg of kinetic energy, and this can exceed the binding energy of these early minihalos by multiple orders of magnitude, even if only a few percent of this kinetic energy binds to the gas in the halo. This is very important for the transition to metal-enriched Pop II star formation, as a halo must be able

to retain the metals released in a supernova for it to transition. In our model we allow halos to go through multiple phases of Pop III star formation until they can accumulate enough metals for this transition. We use metal yields from the simulations presented in Heger & Woosley (2010) for Pop III core-collapse supernovae although, in practice, the specific amount of metals produced does not matter in our model. A single supernova will produce more than enough metals for a halo to transition, so it is only a matter of retaining even a small fraction of these metals for the transition to occur.

After a supernova occurs in a halo, we assume that 10% of its kinetic energy binds to the gas in the halo and then calculate the fraction that is ejected assuming the gas follows a Maxwell-Boltzmann distribution. We track this ejected material's mass and metallicity, and we allow it to re-accrete onto the halo after a free-fall time. In general, halos are able to accumulate enough metals to transition once they acquire a binding energy that lets them retain a few percent of their gas after a supernova. This tends to happen very close to the atomic cooling threshold at a virial temperature of 10^4 K when atomic hydrogen cooling would become efficient anyway. Most halos in our model tend to form ~ 10 generations of Pop III stars with a lifetime of 5 Myr before transitioning.

In general, all halos end up forming at least one generation of Pop III stars before transitioning to Pop II. The only way to skip this phase in our model is if the LW background rises quickly enough to raise the minimum mass for Pop III star formation above the atomic cooling threshold. This happens in our fiducial momentum regulated models, and after this point all new star formation will occur through atomic cooling.[1] Warm dark matter tends to lessen the abundance of star forming halos, and therefore the LW background and Pop III minimum mass, so it becomes even more difficult to skip the minihalo Pop III phase. In other words, even though warm dark matter suppresses the abundance of small haloes, those

---

[1]These are still technically Pop III stars as they form from pristine gas, though their formation will now occur through atomic rather than molecular hydrogen cooling. This will likely cause them to have a more traditional IMF, making their halos similar to a Pop II halo.

haloes still grow through all of the normal phases. Because the sources are more rare, they do not "self-regulate" with the Lyman-Werner background as efficiently as in the CDM picture, allowing a broader range of haloes to form Pop III stars at any given time.

We note that the models mentioned here cover only a small range of the reasonable parameter space of Pop III star formation. We briefly discuss the relevant parameters in section 5.3.3, and we refer the reader to Mebane et al. (2018) for a more detailed discussion.

5.2.3   Population II Star Formation

The modified mass function from warm dark matter will also affect Pop II star formation, especially if the characteristic mass extends into their typical mass range (i.e., $m_{\mathrm{hm}} \gtrsim 10^8 M_\odot$). We use the feedback-regulated models from Furlanetto et al. (2017) for Pop II star formation in our model. The choice of model is also important for Pop III star formation as Pop II stars will ultimately contribute the most to the LW background which regulates and ends the Pop III phase in the Universe (Mebane et al., 2018). In particular, we use two models here, in which either the energy or momentum carried by supernova winds are assumed to set the star formation efficiency in early galaxies. We define the star formation efficiency of these models as the fraction of accreted material which is turned into stars, and we compute it as

$$f_* \approx \frac{1}{1 + \eta\,(m, z)}. \tag{5.8}$$

Here, m is the halo mass and η relates the rate of star formation to the rate of ejection of material due to feedback, $\dot{M}_{\mathrm{ej}} = \eta \dot{M}_*$. We assume that this process is in equilibrium, and we compute η in the energy-regulated case by equating the kinetic energy released by supernovae to the rate at which a halo acquires binding energy through mass accretion,

$$\eta_{\mathrm{E}} = 10 \epsilon_{\mathrm{k}} \omega_{49} \left(\frac{10^{11.5} M_\odot}{M_h} \right)^{2/3} \left(\frac{9}{1 + z} \right). \tag{5.9}$$

122

In this equation, $\epsilon_{\rm k} = 0.1$ is the fraction of a supernova's kinetic energy which binds to the gas and drives winds, and $\omega_{49} = 1$ is the kinetic energy released in supernova per unit mass in stars in units of 10^{49} erg $M_\odot^{-1}$.

We calculate η in the momentum-regulated case as

$$\eta_{\rm p} = \epsilon_{\rm p} \pi_{\rm fid} \left(\frac{10^{11.5} M_\odot}{M_h} \right)^{1/3} \left(\frac{9}{1+z} \right)^{1/2}, \tag{5.10}$$

where $\epsilon_{\rm p} = 0.2$ is the fraction of momentum released by supernovae which is used to drive winds. The rate of momentum injection is characterized by $\pi_{\rm fid}$ which is of order unity for a Salpeter IMF. The particular values for these parameters were chosen in Furlanetto et al. (2017) to match the observed luminosity function at $z \gtrsim 6$, though they can differ substantially when we move to even higher redshifts and lower halo masses where the first stars form. In particular the momentum-regulated models allow for much more efficient star formation in low mass halos which causes the overall Pop II star formation rate density to rise along with the resulting LW background. This creates a much higher Pop III minimum mass very early on, and the Pop III phase of star formation in the Universe ends much earlier (Mebane et al., 2018).

These energy and momentum regulated models represent two extremes, and we regard them as rough brackets on the "true" star formation rate.

5.3 Results

Here we present our results combining our semi-analytic model for Pop III star formation with warm dark matter. In these models we vary $m_{\rm hm}$ from 10^6–$10^{12} M_\odot$. The lower limit here is set simply because, below $10^6 M_\odot$, warm dark matter does not appreciably affect the halo mass function. The upper limit is chosen as the most extreme model from Schneider et al. (2012), which is slightly above the limits set by the Lyα forest (e.g., Boyarsky et al.,

2009; Garzilli et al., 2019b).

5.3.1 Early Universe Star Formation

We show the star formation rate density of both Pop II and Pop III star-forming halos in Fig. 5.2. In general, the reduced abundance of the minihalos which form Pop III stars leads to a large reduction in the Pop III star formation rate density, especially at high values of $m_{\rm hm}$.

Given the extraordinary faintness of our Pop III sources, the best direct constraints on warm dark matter by galaxy observations will likely come from halos above the atomic cooling threshold, which we assume form Pop II stars. At lower redshifts, when Pop II star formation is occurring in relatively higher mass halos, the difference is not extreme. At higher redshifts, however, even the abundance of Pop II halos is reduced enough for a significant reduction in the star formation rate density.

Most of the curves in Fig. 5.2 assume energy regulation for Pop II star formation. The cyan curve, however, shows our $m_{\rm hm} = 10^{10} M_\odot$ warm dark matter model with momentum regulation. This illustrates a degeneracy between the specific star formation model used and the abundance of star-forming halos. If warm dark matter exists and alters the halo mass function as described in section 5.2.1, it may be difficult to disentangle uncertainties in the star formation model and in the halo mass function (and hence warm dark matter) purely through measurements of the abundance of observable distant galaxies, as the cyan and blue Pop II curves are quite similar. However, the Pop III contributions in these two models are quite different, because that component is more sensitive to the changes in the mass function at very small scales. We also include a model varying β for the $m_{\rm hm} = 10^{10} M_\odot$ case, although this does not significantly alter our results.

Fig. 5.3 shows the UV luminosity function for all our models at $z = 10$. We estimate this by

assuming

$$\dot{m}_* = \mathcal{K}_{\mathrm{UV}} \times L_{\mathrm{UV}}, \tag{5.11}$$

where $\dot{m}_*$ is the star formation rate of a Pop II halo, $\mathcal{K}_{\mathrm{UV}} = 1.15 \times 10^{-28}$ $M_\odot$ yr^{-1} (erg s^{-1} Hz^{-1})$^{-1}$ (Sun & Furlanetto, 2016), and L_{UV} is the intrinsic rest-frame luminosity at 1500–2800 Å. At $z = 10$, Pop III star formation has ceased in all models, so this is only the Pop II luminosity function. We can already rule out some models here, as the most extreme cases are well below current observations (e.g., McLure et al., 2013; Oesch et al., 2013; Schenker et al., 2013; Bowler et al., 2015; Finkelstein et al., 2015; Bouwens et al., 2015). In particular, we rule out the $m_{\mathrm{hm}} = 10^{12} M_\odot$ in agreement with current Lyα (Garzilli et al., 2019a) and gravitational lensing (Gilman et al., 2020) constraints. We note that two of these cases ($m_{\mathrm{hm}} = 10^8$ $M_\odot$ and momentum-regulated $m_{\mathrm{hm}} = 10^{10}$ $M_\odot$) were nearly degenerate in terms of the overall SFRD in Figure 5.2. Here their luminosity functions are also very similar at the bright end, but they do differ at the faint end, as discussed by Furlanetto et al. (2017).

5.3.2   The 21-cm Background

Even without warm dark matter, it is still very unlikely that we will be able to directly detect Pop III star formation in minihalos (Schauer et al., 2020). This is mainly due to the extremely low efficiencies of star formation rather than their low abundance. In Mebane et al. (2018) we found that Pop III minihalos have a magnitude of $M_{\mathrm{AB}} = -5$ to -10 if stars form in isolation or in binaries. We may, however, be able to measure the abundance of these halos indirectly through the cosmic 21-cm background.

After the first stars form, they will build up a Lyα background which couples to the spin temperature of neutral hydrogen in the IGM. This will cause the 21-cm signal to go into absorption relative to the cosmic microwave background.

We calculate the specific intensity of the average Lyα background, $J_\alpha(z)$, directly from the
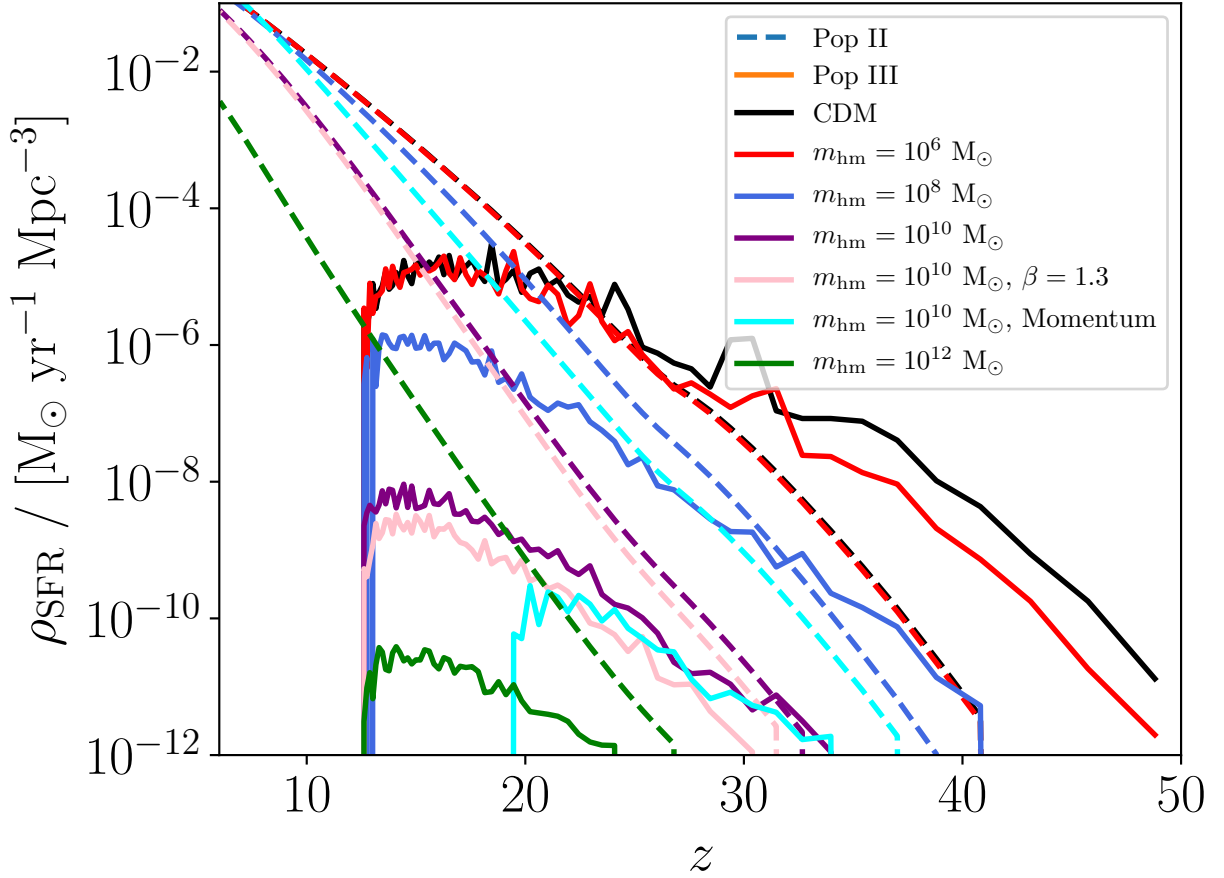
Figure 5.2: Star formation rate density of Pop III and Pop II stars for a variety of warm and cold dark matter models. Our fiducial CDM model is shown in black, and the colored curves show various WDM models. As $m_{\rm hm}$ increases, both Pop III and Pop II star formation are increasingly delayed and reduced. All models shown here assume energy regulation for Pop II star formation except the cyan curve which assumes momentum regulation. In this case, the higher efficiency of star formation in low mass halos causes a subsequent increase in the star formation rate density. Without knowing the details of star formation in the early Universe, there is therefore a degeneracy between the star formation model used and the abundance of dark matter halos due to warm dark matter.
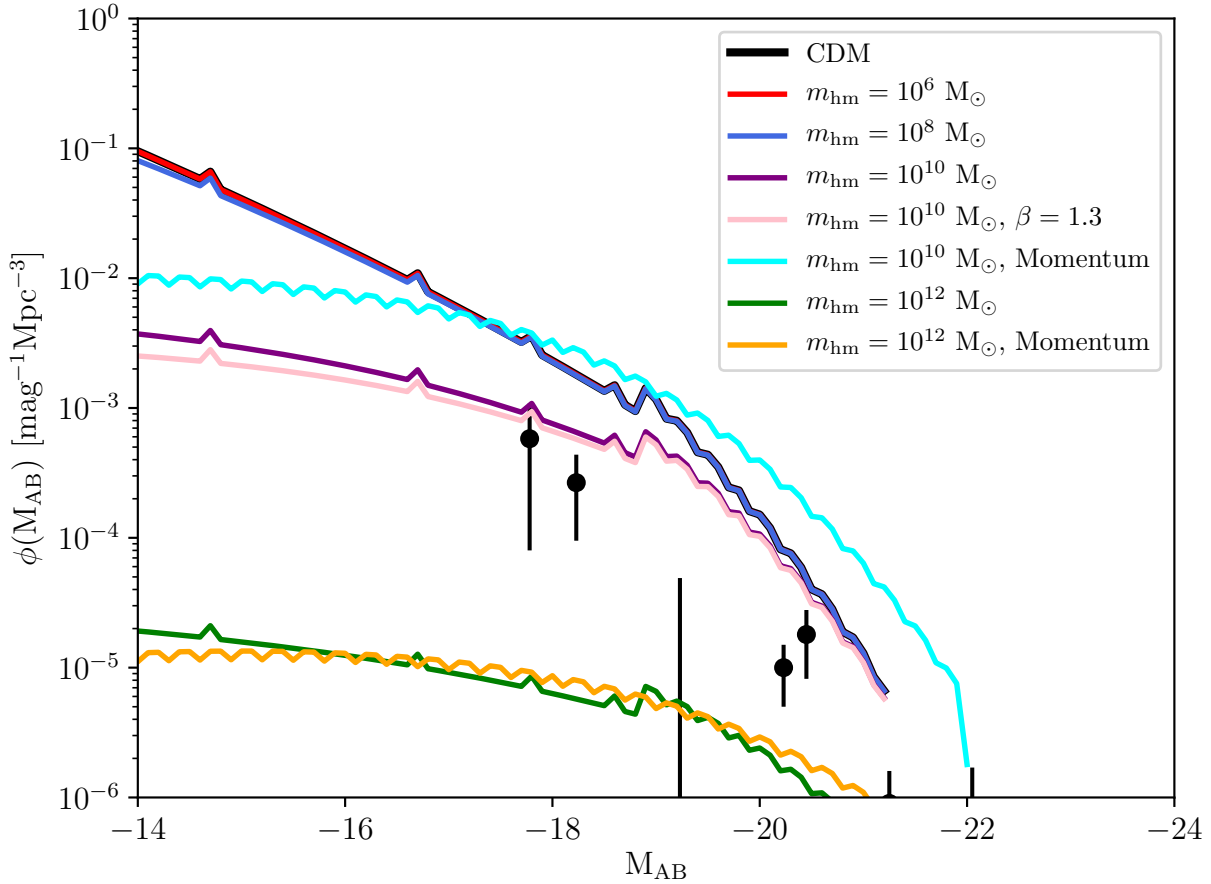
Figure 5.3: Luminosity functions at $z = 10$ for the models presented in this paper. By this time, the only contribution to the luminosity function is from Pop II stars. In general, the reduced halo mass functions from warm dark matter can significantly reduce the luminosity function. The most extreme models here, such as the $m_{hm} = 10^{12} M_\odot$ model with energy or momentum regulation, are already below luminosity function data from Bouwens et al. (2015). The reason the momentum and energy regulated models are so similar in this case is because, at $z = 10$, the $m_{hm} = 10^{12} M_\odot$ mass function turns over at small masses where momentum regulated models have their most efficient star formation compared to energy regulation.

star formation rate density as

$$J_\alpha(z) = \frac{c}{4\pi} \int_z^{z_{\text{max}}} \left| \frac{\mathrm{d}t}{\mathrm{d}z'} \right| (1+z)^3 \, \epsilon_\alpha(z') \mathrm{d}z'. \tag{5.12}$$

Here, z_{max} is the maximum redshift of a source which contributes to the Lyα background felt at redshift z. For simplicity, we assume that continuum photons produced between Lyα and the Lyman continuum contribute to this background, and anything at higher energy is immediately absorbed by the neutral IGM. This sets a maximum redshift of $1+z_{\text{max}} = \frac{4}{3}(1+z)$ (Ciardi & Madau, 2003). We calculate the specific luminosity density of Lyα, ϵ_α, as

$$\epsilon_\alpha(z') = \int_{M_{\text{min}}}^\infty \frac{\Omega_{\text{b}}}{\Omega_{\text{m}}} \frac{\dot{\rho}_*}{m_{\text{p}}} \left(\frac{N_\alpha E_\alpha}{\nu_\alpha} \right) \mathrm{d}M. \tag{5.13}$$

N_α is the number of photons per baryon produced between Lyα and the Lyman continuum by Pop II and Pop III stars. We assume $N_\alpha = 9690$ for Pop II stars (Barkana & Loeb, 2005) and $N_\alpha = 10^5$ for Pop III (Schaerer, 2002). $E_\alpha = 10.2$ eV is the energy of Lyα photons, and $\nu_\alpha = 2.466 \times 10^{15}$ Hz is the corresponding frequency.

Efficient Lyα coupling happens at $J_\alpha \approx 9 \times 10^{-23}(1+z)$ erg s^{-1} cm^{-2} Hz^{-1} sr^{-1} (Ciardi & Madau, 2003). We plot this threshold and the calculated $J_\alpha(z)$ for each of our models in Fig. 5.4. In models with $m_{\text{hm}} > 10^6 M_\odot$ Pop III star formation is suppressed by so much that it does not significantly contribute to J_α. Any differences in this background, therefore, are set by the Pop II star formation rate density. Indeed, if m_{hm} is high enough to substantially suppress Pop II star formation, Lyα coupling may not occur until much later. In the most extreme cases, this coupling may not even occur until the signal vanishes due to reionization. We note that the two almost-degenerate cases ($m_{\text{hm}} = 10^8 M_\odot$ and momentum-regulated $m_{\text{hm}} = 10^{10} M_\odot$) are more different in their Lyα background than in the Pop II SFRD, but the differences mostly manifest at very high redshifts where Pop III stars have a significant contribution in the former case. However, by the time coupling is significant, the differences are small.

We also plot the 21-cm global signal from each of our models in Figure 5.5. We follow Mebane
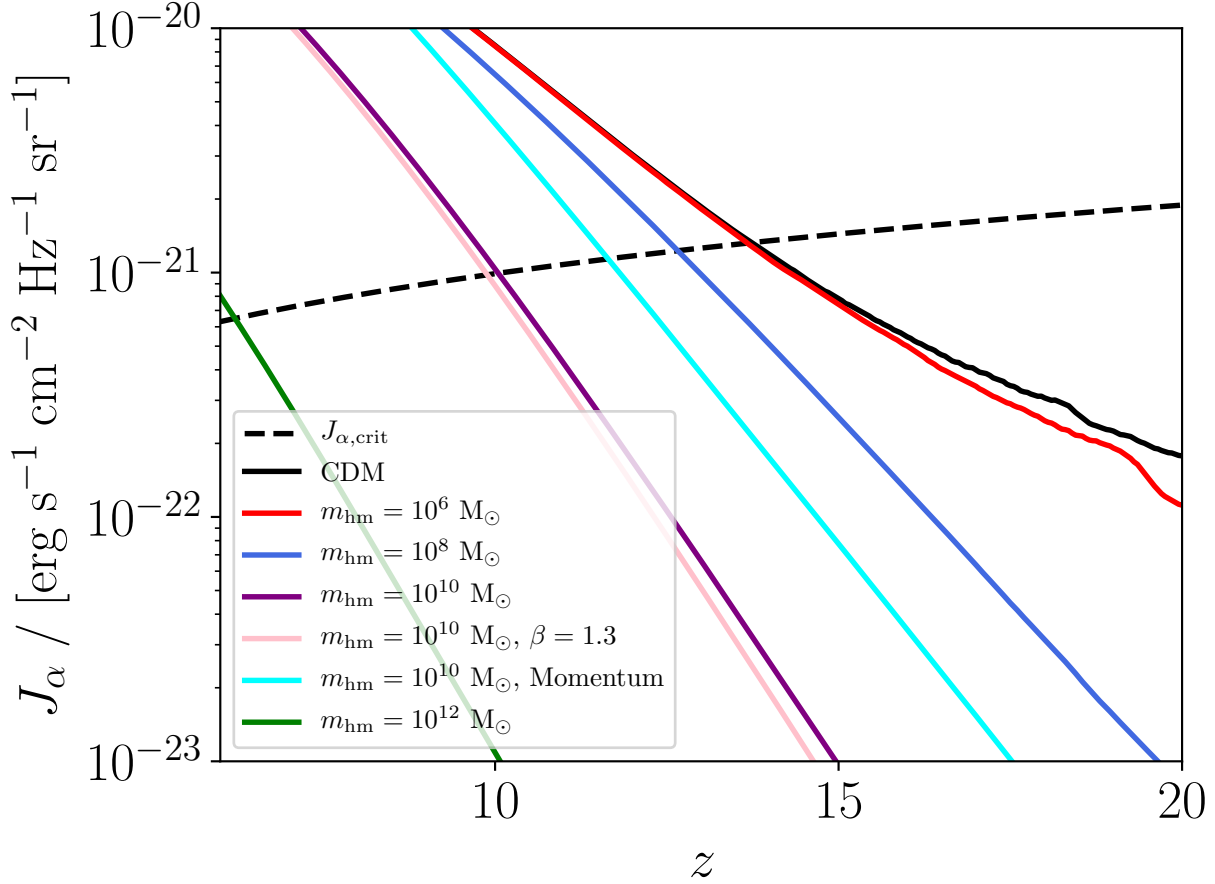
Figure 5.4: Lyα background for the models presented in this work. The dashed line shows the critical background required for efficient Lyα coupling. The background must approximately exceed this threshold for the 21-cm signal to go into absorption. Depending on the assumed value of m_{hm}, the redshift when this occurs can be drastically delayed. In the most extreme cases, this can even delay the absorption signal until the epoch of reionization when the signal will vanish.

et al. (2020) and compute the signal using the 21-cm simulation code ARES (Mirocha, 2014). As expected, the addition of warm dark matter delays the absorption feature in the signal. If the delay is too long, however, X-ray heating from stellar remnants will raise the kinetic temperature of the IGM, causing a shallower signal. In this case, the only way to detect the 21-cm global signal may be if there is a sufficient radio background produced from these remnants which can lower the depth of the absorption feature (see Mebane et al. 2020 for a more detailed discussion of this effect).

5.3.3 Degeneracies with Other Parameters

Warm dark matter can substantially alter the abundance of star-forming halos, which is distinct from other astrophysical effects. However, because the net effect is to decrease the amount of star formation, the observable effects can be degenerate with a number of other astrophysical uncertainties about this era. Some of these include:

1. The Pop III star formation model. The models shown here assume repeated bursts of Pop III star formation until a halo is able to become stable to supernovae and retain metals. In Mebane et al. (2018), we also test models where only one generation of star formation is allowed. Depending on the mass of stars formed per burst and the number of generations allowed to form, this can potentially have a large effect on the Pop III star formation rate density. Altering the abundance of these halos with warm dark matter may make it more difficult to differentiate between these models.

2. The Pop III IMF. In a similar manner, the Pop III IMF can alter the star formation rate density based on the typical mass of a Pop III star. Another complication is that, depending on the mass range in which Pop III stars form, they may end their lives very differently in a core-collapse supernova, a pair-instability supernova, or even directly collapsing into a black hole. These scenarios can alter the way feedback and metal

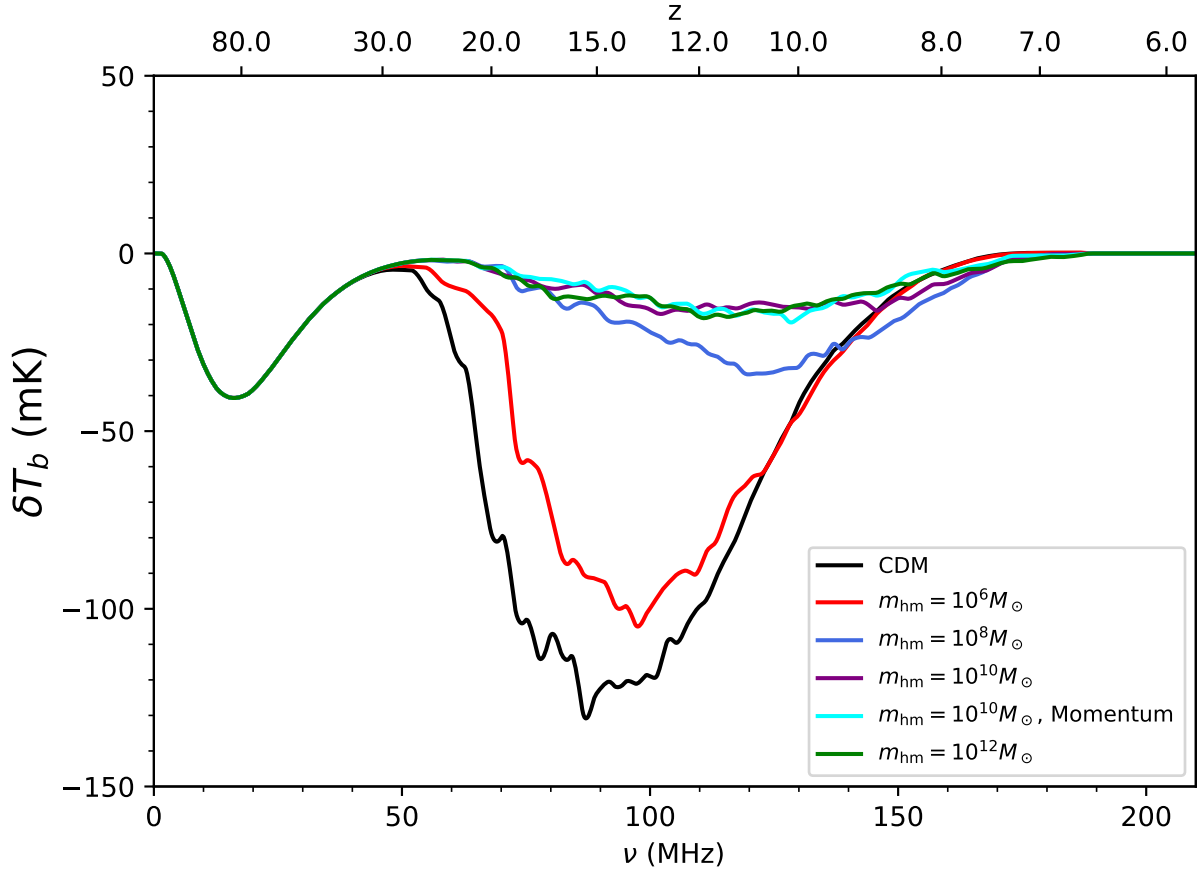Figure 5.5: 21-cm global signal for all of our models. Most models have a significantly reduced depth and are delayed relative to the CDM model. This is due to the delayed Lyα background which couples to the spin temperature of neutral hydrogen and pushes the signal into absorption. If the signal is delayed for too long, X-ray heating will raise the kinetic temperature of the gas, causing a very shallow absorption feature.

production effects the evolution of Pop III halos, further altering the star formation rate density. For example, if Pop III stars form in a mass range where they often collapse to a black hole, they may release few metals into their halos, causing an extended Pop III phase. Alternatively, if feedback is limited and halos can easily retain metals, the transition to Pop II star formation may occur rapidly.

3. The Pop II star formation model. As discussed in section 5.3.1, we can confuse our momentum and energy regulated models of Pop II star formation by adding warm dark matter. If the halo mass function is significantly suppressed at these redshifts, we may have to look to even more efficient models of star formation to match observations of the high redshift luminosity function or reionization. This degeneracy may be broken by the luminosity function (Fig. 5.3), as the momentum and energy regulated models have different slopes, especially on the faint end.

4. The X-ray background. In Mebane et al. (2020) we found that if Pop III remnants have a large contribution to the X-ray background, they can greatly heat the IGM at early times and cause the 21-cm signal to completely vanish. This adds another degeneracy, as it may be difficult to distinguish between a large X-ray background and warm dark matter models with a high m_{hm} since both of these models will cause the signal to vanish. However, such models will manifest differently in other observables (such as the high-z supernova rate; REFS) so may still be distinguishable.

Despite these uncertainties, these kinds of degeneracies will not entirely compromise constraints. The most important aspect of the warm dark matter effect is to delay the formation of large galaxies, which has a clear impact on the 21-cm signal. We have previously found that the timing of the absorption trough in the 21-cm background is fairly robust to astrophysical uncertainties (Mebane et al., 2020), because it depends primarily on when halos are able to host Pop III stars. Thus we expect this aspect of warm dark matter models to be relatively robust to uncertainties. Additionally, leveraging multiple observables should help

to isolate the effects of warm dark matter. For example, we have already seen that even when the SFRDs are similar, the amplitude of the 21-cm background can distinguish some models.

5.4 Conclusions

We present a model for the formation and evolution of Pop III star-forming halos including the effects of warm dark matter. We combine the semi-analytic model described in Mebane et al. (2018) with an altered halo mass function to study warm dark matter's effects on both the star formation rate density and 21-cm background in the early Universe. This allows us to probe these effects on lower halo masses than other studies that use the Lyα forest or gravitational lensing. In general, we find that the reduced abundance of minihalos due to warm dark matter can drastically delay and reduce the rate of early star formation, although there is a degeneracy between the warm dark matter and star formation models used. This degeneracy may be broken if there are differing slopes in the UV luminosity function for potential star formation models. In models with $m_{\rm hm} > 10^6 M_\odot$, Pop II star formation is delayed enough to significantly lower the redshift of Lyα coupling to the spin temperature of neutral hydrogen in the IGM. We can already rule out the most extreme warm dark matter models by comparing our results to the observed luminosity function at high redshift. This is in agreement with Lyα forest and gravitational lensing studies which find similar constraints.

While we may not be able to directly observe the abundance of Pop III star-forming halos, the 21-cm background does provide an exciting opportunity to probe not only minihalo Pop III star formation but also the nature of dark matter. Though there are many uncertainties in the parameters governing the formation of the first stars which cause the 21-cm background, upcoming experiments such as the Hydrogen Epoch of Reionization Array (HERA) or the Square Kilometre Array (SKA) should be able to at least rule out the most extreme warm

dark matter models. If the detection from the EDGES experiment is confirmed and the 21-cm signal has a very deep and early absorption feature, this may rule out many warm dark matter models if large amounts of early star formation are required to produce such a signal.

CHAPTER 6

Conclusions

I have presented a study of the first generations of star formation in the Universe and their effects on the cosmological 21-cm background. I accomplished this by developing a semi-analytic model for the formation and evolution of Pop III star forming halos and interfacing this model with updated versions of the 21-cm global signal code ARES and the 21-cm simulation code 21CMFAST. I also studied the effects of warm dark matter on this mode of star formation.

With the semi-analytic model, I showed that minihalo Pop III star formation can form at rates up to $10^{-4} - 10^{-5}$ M$_\odot$ yr^{-1} Mpc^{-3} and typically ends before $z \sim 12$. This is highly dependent on the Pop II star formation model which dominates the Lyman-Werner background and sets the minimum halo mass for Pop III star formation. If a halo is unable to retain the metals produced in supernovae due to feedback, a single halo may experience multiple generations of Pop III star formation. These Pop III halos have magnitudes of $M_{\rm AB} = -5$ to -10, so we will likely have to indirectly detect them through their supernovae or the 21-cm background.

I also studied the 21-cm global signal and showed that Pop III stars can explain the depth of the absorption feature in the claimed EDGES detection if their remants are efficient at emitting in the radio but inefficient in X-rays. Even if this excess radio background is not what causes the abnormally large depth, my models can still explain the timing of the signal. Pop III stars can easily produce a strong enough Lyman-α background to couple to the spin

temperature of the IGM, causing an earlier absorption feature than expected from Pop II only models.

Pop III star formation can also have a large effect on the 21-cm power spectrum. I found that there is only a slight variation in the shape of the power spectrum when including Pop III stars, although there can be large changes in the amplitude. The largest effect here is the X-ray background which, if sufficiently strong, can uniformly heat the IGM and smooth out the signal. Because this X-ray heating is cumulative, it can even affect the signal well after Pop III star formation ends. The specific Pop II model used is also important because it sets the minimum mass of Pop III star formation due to its contributions to the Lyman Werner background. I included a spatially dependent calculation of this background and found that it only varies by a few percent across our simulation volume, and star formation is well approximated by using the average value.

Finally, I studied the effects of warm dark matter on star formation in the early Universe and the 21-cm background. If WDM has a large velocity dispersion, it will limit the formation of low mass halos. This effect is strongest at the low masses and high redshifts when the first stars form, so, depending on the WDM model assumed, it will have a large affect on both Pop III and Pop II star formation and the resulting 21-cm background. Because it affects the abundance of these halos, WDM introduces a degeneracy with the specific star formation model used.

This is an exciting time in the field of high redshift star formation and the cosmic 21-cm background. Upcoming telescopes such as the James Webb Space Telescope (JWST) will probe star formation in the dimmest and most distant galaxies ever observed. There is already one claimed detection of the 21-cm background from the EDGES experiment, and even more sensitive instruments such as the Hydrogen Epoch of Reionization Array (HERA) and the Square Kilometre Array (SKA) will soon probe the spatial fluctuations of the signal. As we begin to see the first data from these experiments, we will be able to chip away at the

large parameter space of these theoretial models to better understand the cosmic dawn.

Bibliography

Abel T., Bryan G. L., Norman M. L., 2002, Science, 295, 93

Agarwal B., Smith B., Glover S., Natarajan P., Khochfar S., 2016, MNRAS, 459, 4209

Ahn K., Shapiro P. R., Iliev I. T., Mellema G., Pen U.-L., 2008, in O'Shea B. W., Heger A., eds, American Institute of Physics Conference Series Vol. 990, First Stars III. pp 374–376 (arXiv:0807.0920), doi:10.1063/1.2905584

Aller M. C., Richstone D., 2002, AJ, 124, 3035

Atek H., et al., 2015, ApJ, 814, 69

Barkana R., 2018, Nature, 555, 71

Barkana R., Loeb A., 2005, ApJ, 626, 1

Baur J., Palanque-Delabrouille N., Yèche C., Boyarsky A., Ruchayskiy O., Armengaud É., Lesgourgues J., 2017, J. Cosmology Astropart. Phys., 2017, 013

Behroozi P. S., Silk J., 2015, ApJ, 799, 32

Behroozi P. S., Wechsler R. H., Conroy C., 2013, ApJ, 770, 57

Berlin A., Hooper D., Krnjaic G., McDermott S. D., 2018, Phys. Rev. Lett., 121, 011102

Birrer S., Amara A., Refregier A., 2017, J. Cosmology Astropart. Phys., 2017, 037

Bouwens R. J., et al., 2015, ApJ, 803, 34

Bowler R. A. A., et al., 2015, MNRAS, 452, 1817

Bowler R. A. A., McLure R. J., Dunlop J. S., McLeod D. J., Stanway E. R., Eldridge J. J., Jarvis M. J., 2017, MNRAS, 469, 448

Bowman J. D., Rogers A. E. E., Monsalve R. A., Mozdzen T. J., Mahesh N., 2018, Nature, 555, 67

Boyarsky A., Lesgourgues J., Ruchayskiy O., Viel M., 2009, J. Cosmology Astropart. Phys., 2009, 012

Boyarsky A., Iakubovskyi D., Ruchayskiy O., Rudakovskyi A., Valkenburg W., 2019, Phys. Rev. D, 100, 123005

Bradley R. F., Tauscher K., Rapetti D., Burns J. O., 2019, ApJ, 874, 153

Brehmer J., Mishra-Sharma S., Hermans J., Louppe G., Cranmer K., 2019, ApJ, 886, 49

Bromm V., 2013, Reports on Progress in Physics, 76, 112901

Bromm V., Larson R. B., 2004, ARA&A, 42, 79

Bromm V., Loeb A., 2003, Nature, 425, 812

Bromm V., Coppi P. S., Larson R. B., 1999, ApJ, 527, L5

Bromm V., Yoshida N., Hernquist L., 2003, ApJ, 596, L135

Chatterjee A., Dayal P., Choudhury T. R., Hutter A., 2019, MNRAS, 487, 3560

Chen X., Miralda-Escudé J., 2004, ApJ, 602, 1

Cheung K., Kuo J.-L., Ng K.-W., Tsai Y.-L. S., 2019, Physics Letters B, 789, 137

Chianese M., Di Bari P., Farrag K., Samanta R., 2019, Physics Letters B, 790, 64

Ciardi B., Madau P., 2003, ApJ, 596, 1

Clark P. C., Glover S. C. O., Smith R. J., Greif T. H., Klessen R. S., Bromm V., 2011, Science, 331, 1040

Coe D., et al., 2013, ApJ, 762, 32

Costa A. A., Landim R. C. G., Wang B., Abdalla E., 2018, European Physical Journal C, 78, 746

Crosby B. D., O'Shea B. W., Smith B. D., Turk M. J., Hahn O., 2013a, ApJ, 773, 108

Crosby B. D., O'Shea B. W., Smith B. D., Turk M. J., Hahn O., 2013b, ApJ, 773, 108

Das A., Mesinger A., Pallottini A., Ferrara A., Wise J. H., 2017, MNRAS, 469, 1166

Dekel A., Krumholz M. R., 2013, MNRAS, 432, 455

Draine B. T., Miralda-Escudé J., 2018, ApJ, 858, L10

Ewall-Wice A., Chang T.-C., Lazio J., Doré O., Seiffert M., Monsalve R. A., 2018, ApJ, 868, 63

Falkowski A., Petraki K., 2018, arXiv e-prints, p. arXiv:1803.10096

Faucher-Giguère C.-A., Kereš D., Ma C.-P., 2011, MNRAS, 417, 2982

Feng C., Holder G., 2018, ApJ, 858, L17

Fialkov A., Barkana R., 2019, MNRAS, 486, 1763

Field G. B., 1958, Proceedings of the IRE, 46, 240

Finkelstein S. L., et al., 2015, ApJ, 810, 71

Fixsen D. J., et al., 2011, ApJ, 734, 5

Furlanetto S. R., 2006, MNRAS, 371, 867

Furlanetto S. R., Oh S. P., Briggs F. H., 2006, Phys. Rep., 433, 181

Furlanetto S. R., Mirocha J., Mebane R. H., Sun G., 2017, MNRAS, 472, 1576

Garzilli A., Ruchayskiy O., Magalich A., Boyarsky A., 2019a, arXiv e-prints, p. arXiv:1912.09397

Garzilli A., Magalich A., Theuns T., Frenk C. S., Weniger C., Ruchayskiy O., Boyarsky A., 2019b, MNRAS, 489, 3456

Gentile G., Famaey B., Zhao H., Salucci P., 2009, Nature, 461, 627

Gilman D., Birrer S., Treu T., Nierenberg A., Benson A., 2019, MNRAS, 487, 5721

Gilman D., Birrer S., Nierenberg A., Treu T., Du X., Benson A., 2020, MNRAS, 491, 6077

Glover S. C. O., Brand P. W. J. L., 2001, MNRAS, 321, 385

Gnedin N. Y., Hui L., 1998, MNRAS, 296, 44

Goerdt T., Ceverino D., Dekel A., Teyssier R., 2015, MNRAS, 454, 637

Greif T. H., Glover S. C. O., Bromm V., Klessen R. S., 2010, ApJ, 716, 510

Haiman Z., Rees M. J., Loeb A., 1997, ApJ, 476, 458

Heger A., Woosley S. E., 2002, ApJ, 567, 532

Heger A., Woosley S. E., 2010, ApJ, 724, 341

Hills R., Kulkarni G., Meerburg P. D., Puchwein E., 2018, Nature, 564, E32

Hirano S., Bromm V., 2017, MNRAS, 470, 898

Hirano S., Bromm V., 2018, MNRAS, 480, L85

Hirano S., Hosokawa T., Yoshida N., Omukai K., Yorke H. W., 2015, MNRAS, 448, 568

Hirata C. M., 2006, MNRAS, 367, 259

Holzbauer L. N., Furlanetto S. R., 2012, MNRAS, 419, 718

Inoue K. T., Takahashi R., Takahashi T., Ishiyama T., 2015, MNRAS, 448, 2704

Jaacks J., Thompson R., Finkelstein S. L., Bromm V., 2018, MNRAS, 475, 4396

Jia L.-B., 2019, European Physical Journal C, 79, 80

Johnson J. L., Bromm V., 2006, MNRAS, 366, 247

Kovetz E. D., Poulin V., Gluscevic V., Boddy K. K., Barkana R., Kamionkowski M., 2018,
    Phys. Rev. D, 98, 103529

Kuhlen M., Madau P., 2005, Monthly Notices of the Royal Astronomical Society, 363, 1069

Kulkarni G., Rollinde E., Hennawi J. F., Vangioni E., 2013, ApJ, 772, 93

Kusenko A., 2009, Phys. Rep., 481, 1

Lawson K., Zhitnitsky A. R., 2019, Physics of the Dark Universe, 24, 100295

Loeb A., Furlanetto S. R., 2013, The First Galaxies in the Universe

Lopez-Honorez L., Mena O., Villanueva-Domingo P., 2019, Phys. Rev. D, 99, 023522

Lovell M. R., Frenk C. S., Eke V. R., Jenkins A., Gao L., Theuns T., 2014, MNRAS, 439,
    300

Machacek M. E., Bryan G. L., Abel T., 2001, ApJ, 548, 509

Machacek M. E., Bryan G. L., Abel T., 2003, MNRAS, 338, 273

Maio U., Ciardi B., Dolag K., Tornatore L., Khochfar S., 2010, MNRAS, 407, 1003

Markovič K., Viel M., 2014, PASA, 31, e006

Mason C. A., Trenti M., Treu T., 2015, ApJ, 813, 21

Matthee J., et al., 2017, preprint, (arXiv:1709.06569)

McBride J., Fakhouri O., Ma C.-P., 2009, MNRAS, 398, 1858

McGreer I. D., Bryan G. L., 2008, ApJ, 685, 8

McKee C. F., Tan J. C., 2008, ApJ, 681, 771

McLeod D. J., McLure R. J., Dunlop J. S., Robertson B. E., Ellis R. S., Targett T. A., 2015,
    MNRAS, 450, 3032

McLure R. J., et al., 2013, MNRAS, 432, 2696

Mebane R. H., Mirocha J., Furlanetto S. R., 2018, MNRAS, 479, 4544

Mebane R. H., Mirocha J., Furlanetto S. R., 2020, MNRAS, 493, 1217

Merloni A., Heinz S., di Matteo T., 2003, MNRAS, 345, 1057

Mesinger A., Furlanetto S., Cen R., 2011, MNRAS, 411, 955

Miranda M., Macciò A. V., 2007, MNRAS, 382, 1225

Mirocha J., 2014, MNRAS, 443, 1211

Mirocha J., Furlanetto S. R., 2019, MNRAS, 483, 1980

Mirocha J., Furlanetto S. R., Sun G., 2017, MNRAS, 464, 1365

Mirocha J., Mebane R. H., Furlanetto S. R., Singal K., Trinh D., 2018, MNRAS, 478, 5591

Mitsuda K., et al., 1984, PASJ, 36, 741

Moore B., Quinn T., Governato F., Stadel J., Lake G., 1999, MNRAS, 310, 1147

Moroi T., Nakayama K., Tang Y., 2018, Physics Letters B, 783, 301

Muñoz J. A., Furlanetto S. R., 2013, MNRAS, 435, 2676

Muñoz J. B., Dvorkin C., Loeb A., 2018, Phys. Rev. Lett., 121, 121301

Naoz S., Barkana R., 2007, MNRAS, 377, 667

Neistein E., Dekel A., 2008, MNRAS, 388, 1792

O'Shea B. W., Norman M. L., 2008, ApJ, 673, 14

Oesch P. A., et al., 2013, ApJ, 773, 75

Oesch P. A., et al., 2014, ApJ, 786, 108

Oh S. P., Haiman Z., 2002, ApJ, 569, 558

Oh S. P., Haiman Z., 2003, MNRAS, 346, 456

Omukai K., Hosokawa T., Yoshida N., 2010, ApJ, 722, 1793

Park J., Mesinger A., Greig B., Gillet N., 2019, MNRAS, 484, 933

Planck Collaboration et al., 2015, preprint, (arXiv:1502.01589)

Press W. H., Schechter P., 1974, ApJ, 187, 425

Pritchard J. R., Furlanetto S. R., 2006, MNRAS, 367, 1057

Pritchard J. R., Loeb A., 2008, Phys. Rev. D, 78, 103511

Qin Y., Mesinger A., Park J., Greig B., Muñoz J. B., 2020, MNRAS, 495, 123

Ricotti M., 2016, MNRAS, 462, 601

Robertson B. E., Ellis R. S., Furlanetto S. R., Dunlop J. S., 2015, ApJ, 802, L19

Safarzadeh M., Scannapieco E., Babul A., 2018, ApJ, 859, L18

Sarmento R., Scannapieco E., Cohen S., 2018, ApJ, 854, 75

Schaerer D., 2002, A&A, 382, 28

Schauer A. T. P., Glover S. C. O., Klessen R. S., Ceverino D., 2019, MNRAS, 484, 3510

Schauer A. T. P., Drory N., Bromm V., 2020, arXiv e-prints, p. arXiv:2007.02946

Schenker M. A., et al., 2013, ApJ, 768, 196

Schneider R., Omukai K., Inoue A. K., Ferrara A., 2006, MNRAS, 369, 1437

Schneider A., Smith R. E., Macciò A. V., Moore B., 2012, MNRAS, 424, 684

Shapiro P. R., Iliev I. T., Raga A. C., 2004, MNRAS, 348, 753

Sheth R. K., Tormen G., 1999, MNRAS, 308, 119

Sims P. H., Pober J. C., 2019, arXiv e-prints, p. arXiv:1910.03165

Sims P. H., Pober J. C., 2020, MNRAS, 492, 22

Slatyer T. R., Wu C.-L., 2018, Phys. Rev. D, 98, 023013

Smith B. D., Wise J. H., O'Shea B. W., Norman M. L., Khochfar S., 2015, MNRAS, 452, 2822

145

Sobacchi E., Mesinger A., 2014, MNRAS, 440, 1662

Sobral D., Matthee J., Darvish B., Schaerer D., Mobasher B., Röttgering H. J. A., Santos S., Hemmati S., 2015, ApJ, 808, 139

Spinelli M., Bernardi G., Santos M. G., 2019, MNRAS, 489, 4007

Springel V., et al., 2008, MNRAS, 391, 1685

Stacy A., Greif T. H., Bromm V., 2012, MNRAS, 422, 290

Stecher T. P., Williams D. A., 1967, ApJ, 149, L29

Sun G., Furlanetto S. R., 2016, MNRAS, 460, 417

Tauscher K., Rapetti D., Burns J. O., 2020, ApJ, 897, 132

Tegmark M., Silk J., Rees M. J., Blanchard A., Abel T., Palla F., 1997, ApJ, 474, 1

Trac H., Cen R., Mansfield P., 2015, ApJ, 813, 54

Trenti M., Stiavelli M., 2009, ApJ, 694, 879

Trenti M., Stiavelli M., Michael Shull J., 2009, ApJ, 700, 1672

Turk M. J., Abel T., O'Shea B., 2009, Science, 325, 601

Vale A., Ostriker J. P., 2004, MNRAS, 353, 189

Visbal E., Haiman Z., Terrazas B., Bryan G. L., Barkana R., 2014, MNRAS, 445, 107

Visbal E., Haiman Z., Bryan G. L., 2018, MNRAS, 475, 5246

Wang M.-Y., Croft R. A. C., Peter A. H. G., Zentner A. R., Purcell C. W., 2013, Phys. Rev. D, 88, 123515

Whalen D., O'Shea B. W., Smidt J., Norman M. L., 2008a, ApJ, 679, 925

Whalen D., van Veelen B., O'Shea B. W., Norman M. L., 2008b, ApJ, 682, 49

Whalen D. J., Fryer C. L., Holz D. E., Heger A., Woosley S. E., Stiavelli M., Even W., Frey L. H., 2013, ApJ, 762, L6

Wise J. H., Abel T., 2007, ApJ, 671, 1559

Wise J. H., Abel T., 2008, ApJ, 685, 40

Wolcott-Green J., Haiman Z., Bryan G. L., 2017, MNRAS, 469, 3329

Wouthuysen S. A., 1952, AJ, 57, 31

Xu H., Wise J. H., Norman M. L., Ahn K., O'Shea B. W., 2016, ApJ, 833, 84

Yoshida N., Sokasian A., Hernquist L., Springel V., 2003, ApJ, 591, L1

Yoshida N., Oh S. P., Kitayama T., Hernquist L., 2007a, ApJ, 663, 687

Yoshida N., Omukai K., Hernquist L., 2007b, ApJ, 667, L117

Zheng W., et al., 2012, Nature, 489, 406

de Blok W. J. G., 2010, Advances in Astronomy, 2010, 789293